NUMERICAL EXPERIMENTS ON CHARACTERISTICS OF NONLINEAR ENERGY TRANSFER OF OCEAN WAVES

フィトリ, スチアティ

NUMERICAL EXPERIMENTS ON CHARACTERISTICS OF NONLINEAR ENERGY TRANSFER OF OCEAN WAVES

Fitri Suciaty

July, 2016

NUMERICAL EXPERIMENTS ON CHARACTERISTICS OF NONLINEAR ENERGY TRANSFER OF OCEAN WAVES

A Dissertation

submitted for the degree of

Doctor of Engineering

by

Fitri Suciaty

Kyushu University

July, 2016

ABSTRACT

A numerical study of the nonlinear energy transfer spectrum for a gravity wave spectrum is carried out with the aim of presenting an alternative to the resonant configuration number so as to approximate the nonlinear transfer of a given wave spectrum with sufficient accuracy and efficiency.

The long-term evolution of a gravity wave spectrum caused by nonlinear energy transfer is investigated using three different types of the third-generation wave model, i.e., the wave action model (WAM), where each type is implemented with the discrete-interaction approximation (DIA) method (Hasselmann et. al., 1985), Research Institute for Applied Mathematics (RIAM) method (Komatsu et. al., 1993), and simplified RIAM (SRIAM) method (Komatsu et. al., 1996) under duration-limited conditions. The numerical results of these methods for various directional spectra, including multimodal spectra, are compared. The comparisons show that the SRIAM method is superior to the other methods for practical applications of the wave model.

The WAM model implemented with the finite-depth RIAM (FD-RIAM) method (Hashimoto et.al, 1998) is applied under duration-limited conditions for nonlinear energy transfer computation in finite water depths. The evolution of directional spectra in finite water depths caused by nonlinear energy transfer is confirmed to be much faster than that in deep water.

Two new methods for nonlinear energy transfer computation with free parameters similar to those in the RIAM method are presented. The first method, i.e., the reduced SRIAM (R-SRIAM) method using only a number of configurations of nine, is able to show almost the same degree of accuracy as the original SRIAM method. This result was applied to the second method, i.e., the alternative multiple DIA method, where the resonance configurations are selected only from the quasi-singular quadruplets. These approximations have the advantage of better accuracy than that of the existing model using the DIA method.

ACKNOWLEDGEMENTS

Contents

LIST OF FIGURES

LIST OF TABLES

CHAPTER 1

INTRODUCTION

1.1 Background

Currently, there is a rapidly growing need for wave forecasts and wave climatology in maritime countries. To meet this demand for wave information, wave conditions must be estimated over large tracts of ocean in regular intervals, often many times a day. The amount of data and calculations makes computers indispensable. Numerical wave models have been developed for the required estimates of wave conditions. For several decades, ocean wave modeling has been an interesting subject. Wave modeling is not only used for practical purposes such as wave forecasting, but also involves many fundamental sciences.

Following Hasselman (1960), ocean wave modeling is generally based on the action or energy balance equation of the following form:

$$\frac{DF}{Dt} = S_{tot} = S_{in} + S_{nl} + S_{ds}, \tag{1.1}$$

where F is the variance of an energy spectrum and S_{tot} represents the source terms of the spectral energy, including the wind input (S_{in}), nonlinear energy transfer (S_{nl}), and dissipation (S_{ds}) source terms. To predict the evolution of wave spectra with high accuracy, each of the source functions must be estimated accurately.

Among the three source terms, the nonlinear energy transfer term is known to play an important role in wind wave evolution. Cavaleri et al. (2007) suggested that nonlinear energy transfer is probably the most solid piece of information in wave modeling. Inspires by fundamental physics, and brought to light more than 40 years ago, the nonlinear energy transfer term is well defined. However, a proper evaluation of required computational time in practical applications is not yet available.

The physical meaning of nonlinear energy transfer is a redistribution of energy caused by four-wave resonance in spectral space, in which wave energy is transferred from the spectral peak to low and high frequencies. Nonlinear energy transfer is also suggested to provide the lowest order

mechanism to transfer wave energy to waves of longer wave lengths, and a stabilization mechanism for the shape of the spectrum (Tolman, 2003).

Nonlinear energy transfer can be computed using the Boltzmann integral, originally proposed by Hasselmann (1962). The computation of the Boltzmann integral consists of a six-dimensional integral, a complicated coupling coefficient, and two delta functions corresponding to the resonance conditions. Therefore, this computation is very complicated, making the numerical integration difficult, unstable, and very time consuming (Hashimoto and Kawaguchi, 2001).

Various approximations have been developed to compute nonlinear energy transfer. Masuda (1980), Tracy and Resio (1982), Resio and Perrie (1991), Komatsu and Masuda (1996), and Van Vledder (2000) have improved the exact computation using various approaches. Even with this improvement, the exact nonlinear energy transfer is computationally expensive because of multiple integrations and complexity of the interaction coefficient G, thus making it computationally formidable in practical models (Tolman, 2003).

Hasselmann et al. (1985) developed the discrete-interaction approximation (DIA) to overcome the shortcomings of the exact methods. The DIA takes into account the interaction of each wave component only from two quadruplets in the spectrum. For each of these two quadruplets, the self-interaction of the wave components and their interaction with the other two wave components (making it formally four components in total) are computed (Holthuijsen, 2007). Hasselmann et al. showed that the DIA preserves a few but important characteristics of the full solution, such as slow downshifting of the peak frequency and shape stabilization during wave growth (Cavaleri et al., 2007).

Most types of the third-generation wave model such as the wave action model (WAM) (WAMDI Group, 1988), WAVEWATCH (Tolman, 1991, 2002c), TOMAWAC (Benoit et al., 1997), the simulating waves nearshore (SWAN) model (Booij et al., 1999), and the recently developed coupled routing and excess storage (CREST) model (Ardhuin et al., 2001) have adopted the DIA method for the computation of nonlinear energy transfer. However, the DIA has a drawback in that it has a poor accuracy for approximating nonlinear energy transfer in the case of sharp-shaped spectra such as the Joint North Sea Wave Project (JONSWAP) spectrum, although it exhibits good performance for wide-shaped spectra such as the Pierson–Moskowitz spectrum (Hashimoto and Kawaguchi, 2001).

Numerous researches have been performed to derive better accuracy and computationally feasible nonlinear energy transfer algorithms. Komatsu and Masuda (1996) attempted to speed up the calculation and claimed to retain most of the interaction accuracy in computing nonlinear energy transfer at about 20 times the cost of the DIA used in the Simplified Research Institute for Applied Mathematics (SRIAM) method. Ueno and Ishizaka (1997) and Hashimoto and Kawaguchi (2001) developed an approximation for the calculation of nonlinear energy transfer that has more accuracy, more complex quadruplets, or more quadruplet combinations. Tolman (2003) modified the DIA to the variable DIA (VDIA), where the free parameters in the DIA are allowed to be functions of the parameters defining spectral space. However, this approach is less accurate, but more computationally economical than the DIA. Tolman (2013) derived the generalized multiple DIA (GMD) by adding more complexity to the DIA. The GMD method extends the DIA method by allowing for multiple representative quadruplets and by formulating the expressions for arbitrary water depths. The GMD method is capable of removing most of the DIA's errors, but may not be computationally feasible in operational models because of its complexity. The latest version of WAVEWATCH III adopted the GMD method for the computation of nonlinear energy transfer.

Although numerous efforts have been made in the improvement of nonlinear energy transfer computation, despite its deficiency in accuracy the DIA method is still commonly used for evaluating nonlinear energy transfer in practical wave models because of the low computational cost. Up until now, there is no proper definition as to how to justify which method is the best. An intercomparison of those methods is needed for the improvement of nonlinear energy transfer computation.

Theoretically, a precise evaluation of nonlinear energy transfer requires a large number of resonance configurations. Such calculations need huge computational costs that are not suitable for operations in wave models. Therefore, it is very important to identify how many resonance configurations are needed to approximate nonlinear energy transfer with sufficient accuracy and efficiency and to be practically implemented in operational wave models.

The efficient number of resonance configurations for nonlinear energy transfer computation is presented in this study so as to reduce computational costs. The first method is the reduced SRIAM (R-SRIAM) method, which modified the SRIAM method by reducing the number of resonant configurations. Furthermore, the alternative multiple DIA (AM-DIA) method is proposed by selecting the resonance configurations only from the quasi-singular quadruplets. The

reduced number of resonant configurations is expected to make the computational method of nonlinear energy transfer more accurate and computationally feasible, and hence the resulting method can be incorporated in wave models.

1.2 Statement of the Problem

Computations of nonlinear energy transfer need an infinite number of four-wave configurations to satisfy resonance conditions. The DIA method adopted by most of the third-generation wave models uses a single configuration of four-wave resonances selected from an infinite number of configurations. Although the DIA has low computational cost, it is yet a rough way to compute nonlinear energy transfer. The DIA method also limited to complex wave fields. Tamura (2008) suggested the SRIAM method (Komatsu and Masuda, 1996) to be incorporated into operational wave models. The SRIAM method was developed to accurately reproduce S_{nl} using 20 resonance configurations. It has low computational cost than more rigorous algorithms. However, its computational cost is still larger than that of existing operational wave models using the DIA (by 20 times). Hence, it is necessary to know how many resonance configurations are required to estimate nonlinear transfer reasonably accurately.

1.3 Purpose of the Study

The purposes of this study are as follows.

- To clarify fundamental processes of wave generation and development by investigating the characteristics of directional spectra evolution in long-time integrations caused by nonlinear energy transfer in deep and infinite water depths.
- To evaluate performance of the DIA, RIAM, and SRIAM method for computing nonlinear energy transfer in order to direct a suggestion to the improvements of nonlinear energy transfer computation.
- To present the efficient number of configurations for nonlinear energy transfer computation with better accuracy and less computational time than existing methods that can be incorporated in operational wave models.

1.4 Importance of the Study

The R-SRIAM and AM-DIA methods are expected to provide economical solutions for computing nonlinear energy transfer without losing accuracy. Furthermore, this study is

conducted to improve the performance of wave modeling for high-accuracy wave generation prediction, not only for practical purposes, such as wave forecasting and hazard mitigation, but also for an understanding of the beauty of nature.

1.5 Outline

This dissertation consists of six chapters. Chapter 1 is an introduction to the background of this study. It also presents the purposes and importance of this study. This chapter is closed with an outline of the dissertation.

Chapter 2 describes some previous methods that provide high-accuracy nonlinear energy transfer computation. For evaluating the Boltzmann integral in nonlinear energy transfer computation, descriptions of the DIA (Hasselmann et al., 1985), RIAM (Komatsu et al., 1993), SRIAM (Komatsu et al., 1996), extended DIA (EDIA), and Multiple DIA (MDIA) (Hashimoto et al, 2001) methods in deep water and the finite-depth RIAM (FD-RIAM) method (Hashimoto et al, 1998) in finite water depths are presented.

To understand the fundamental process of wave generation and wave development in deep water depth, as a preliminary of this study, the long-term evolution of a gravity wave spectrum caused by nonlinear energy transfer is investigated in Chapter 3 using the third-generation wave model, i.e., the WAM, implemented with the DIA, RIAM, and SRIAM methods. The numerical simulations were performed under duration-limited conditions for various initial conditions of the directional spectra. Intercomparisons of those methods were conducted, leading to a suggestion of the best method. The numerical results show that the SRIAM method seems to be superior to the other methods. In addition, the characteristics of frequency downshift are investigated in the WAM model implemented in the SRIAM method. The relation between frequency downshift, wave steepness, peak frequency, and energy concentration parameters are presented. As a result, interesting characteristics of frequency downshift for the gravity wave spectrum caused by nonlinear energy transfer are clarified in both frequency and directional domains, with a special focus on the relation between frequency downshift and energy concentration parameters of the directional spectra. This chapter also discusses the characteristics of bimodal directional spectra in the frequency and directional domains.

Chapter 4 focuses on nonlinear energy transfer computation in finite water depths using a modified WAM implemented with the FD-RIAM method under duration-limited conditions. The evolution of directional spectra in finite water depths caused by nonlinear energy transfer was confirmed to be much faster than that in deep water. The enhancement factor used in the third-generation wave models and the downshift factor for various directional spectra in various water depths are also evaluated.

The proposed efficient number of configurations for nonlinear energy transfer computation is presented in Chapter 5. First, we modify the SRIAM method, developed by Komatsu and Masuda (1996), by reducing the number of configurations. This method is called the R-SRIAM method. The second method is the AM-DIA method, which has efficient configurations selected only from the quasi-singular quadruplets. The numerical computation results of the R-SRIAM and AM-DIA method are compared with those of the RIAM and original SRIAM methods, which have been proven to have the same degree of accuracy with the exact method developed by Masuda (1980) and by Komatsu and Masuda (1996). As a result, the R-SRIAM method is less time consuming than the original SRIAM method, but still more time consuming than the DIA method. Meanwhile, the AM-DIA method with two configurations is more accurate than the DIA method, and more economical to be incorporated into operational wave models than the RIAM, SRIAM, and R-SRIAM methods.

The last chapter summarizes the results and suggests a next step of this study. The major conclusion is that both the R-SRIAM and AM-DIA methods can be considered promising alternative methods for nonlinear energy transfer computation of a gravity wave spectrum in deep water.

CHAPTER 2

COMPUTATION OF NONLINEAR ENERGY TRANSFER

2.1 Introduction

The important role played by the nonlinear energy transfer term in the evolution of the energy spectrum of gravity waves has been well understood because of the JONSWAP project (Hasselmann et al., 1973). It is also described and discussed in, e.g., Phillips (1981a), Resio and Perrie (1991), Young and van Vledder (1993), Banner and Young (1994), and Resio et al. (2001). Moreover, nonlinear energy transfer is an important mechanism that always exists during the propagation of ocean surface waves. However, it is difficult to observe the phenomena of nonlinear energy transfer because they are usually compounded with other physical processes such as the evolution and attenuation of waves (Hashimoto et al., 1998). It is also difficult to discuss this mechanism based on experiments and/or observation data. Therefore, the theoretical approach is necessary to examine the characteristics of nonlinear energy transfer in waves.

The theory for nonlinear energy transfer was developed by Hasselman (1962, 1963a, 1963b). Hasselman found that resonances between a set of four waves, called the quadruplet, can transfer energy. The resonance of four spectral components follows the following conditions:

$$\boldsymbol{k}_1 + \boldsymbol{k}_2 = \boldsymbol{k}_3 + \boldsymbol{k}_4 , \tag{2.1}$$

$$\omega_1 + \omega_2 = \omega_3 + \omega_4 , \tag{2.2}$$

where ω_j and $\boldsymbol{k}_j$ are respectively the angular frequency and wave vector ($j = 1, \ldots, 4$). The frequency and wave number are related by the dispersion relationship $\omega_i^2 = g\mathbf{k}_i \tanh \mathbf{k}_i h$, which reduces to $\omega_i^2 = g\mathbf{k}_i$ in deep water conditions, where g is the gravitational acceleration and h is the water depth.

The nonlinear energy transfer can be computed using the following Boltzmann integral, as originally proposed by Hasselmann (1962),

$$\frac{\partial n_1}{\partial t} = \iiint G\left(\boldsymbol{k}_1, \boldsymbol{k}_2, \boldsymbol{k}_3, \boldsymbol{k}_4\right) \times \delta\left(\boldsymbol{k}_1 + \boldsymbol{k}_2 - \boldsymbol{k}_3 - \boldsymbol{k}_4\right) \times \delta\left(\omega_1 + \omega_2 - \omega_3 - \omega_4\right)$$
$$\times \left[n_1 n_2\left(n_3 + n_4\right) - \left(n_1 + n_2\right)n_3 n_4\right]dk_2 dk_3 dk_4 \tag{2.3}$$

where $n_i = n(\boldsymbol{k}_i)$ is the action density for component i, $G = G(\boldsymbol{k}_1, \boldsymbol{k}_2, \boldsymbol{k}_3, \boldsymbol{k}_4)$ is a complex coupling coefficient (Webb, 1978; Herterich and Hasselmann, 1980), and δ_k and δ_ω are delta functions corresponding to the resonance conditions in Eqs. (2.1) and (2.2).
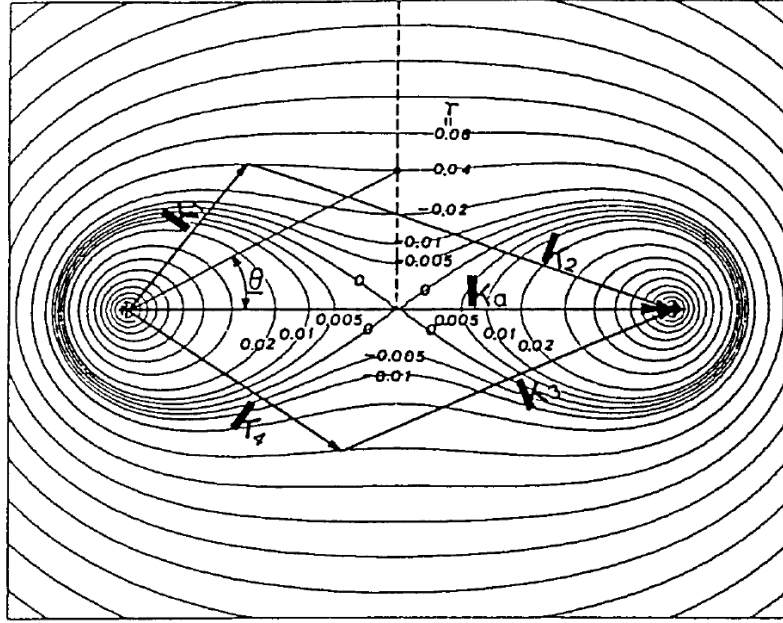
Figure 2.1. Longuet–Higgins interaction chart. The contours of γ are defined in Masuda (1980) for deep-water waves. Adapted from "Nonlinear energy transfer between wind waves", by Masuda, 1980, Journal of Physical Oceanography, Vol.10, 2082-2092. Copyright (1980), American Meteorogical Society.

The Boltzmann integral in Eq. (2.3) consists of a six-fold integral in wave vector space, a complicated coupling coefficient, and two delta functions corresponding to the resonance conditions. The coupling coefficient $G(\boldsymbol{k}_1, \boldsymbol{k}_2, \boldsymbol{k}_3, \boldsymbol{k}_4)$ is defined by

$$G = \frac{9\pi g^2 D^2}{4\rho^2 \omega_1 \omega_2 \omega_3 \omega_4},$$

where ρ is the density of water and D is the interaction coefficient in deep water, defined by (Hasselmann, 1962, 1963a)

$$D = \frac{2\omega_2\left(\omega_1 - \omega_4\right)\left(k_1 k_4 + \mathbf{k}_1 \cdot \mathbf{k}_4\right)\left\{\omega_3^2 \omega_{1-4}^2 + \mathbf{k}_3 \cdot \left(\mathbf{k}_1 - \mathbf{k}_4\right)\right\}}{3\left\{\omega_{1-4}^2 - \left(\omega_1 - \omega_4\right)^2\right\}}$$

$$+ \frac{2\omega_2\left(\omega_1 - \omega_3\right)\left(k_1 k_3 + \mathbf{k}_1 \cdot \mathbf{k}_3\right)\left\{\omega_4^2 \omega_{1-3}^2 + \mathbf{k}_4 \cdot \left(\mathbf{k}_1 - \mathbf{k}_3\right)\right\}}{3\left\{\omega_{1-3}^2 - \left(\omega_1 - \omega_3\right)^2\right\}}$$

$$- \frac{2\omega_2\left(\omega_3 + \omega_4\right)\left(k_3 k_4 + \mathbf{k}_3 \cdot \mathbf{k}_4\right)\left\{\omega_1^2 \omega_{3+4}^2 + \mathbf{k}_1 \cdot \left(\mathbf{k}_3 + \mathbf{k}_4\right)\right\}}{3\left\{\omega_{3+4}^2 - \left(\omega_3 + \omega_4\right)^2\right\}}$$

$$- \omega_3\left(\omega_1 - \omega_4\right)\left(k_1 k_4 + \mathbf{k}_1 \cdot \mathbf{k}_4\right)\left(\omega_3^2 + \omega_{1-4}^2\right)/3$$

$$- \omega_4\left(\omega_1 - \omega_3\right)\left(k_1 k_3 + \mathbf{k}_1 \cdot \mathbf{k}_3\right)\left(\omega_4^2 + \omega_{1-3}^2\right)/3$$

$$- \omega_1\left(\omega_3 + \omega_4\right)\left(k_3 k_4 - \mathbf{k}_3 \cdot \mathbf{k}_4\right)\left(\omega_1^2 + \omega_{3+4}^2\right)/3$$

$$+ \left\{\mathbf{k}_1 \cdot \mathbf{k}_4 - \omega_1 \omega_4\left(k_1 + k_4 - \omega_1 \omega_4\right)\right\}\left\{\omega_3^3\left(\omega_1 - \omega_4\right) - \mathbf{k}_3 \cdot \left(\mathbf{k}_1 - \mathbf{k}_4\right)\right\}/6$$

$$+ \left\{\mathbf{k}_1 \cdot \mathbf{k}_3 - \omega_1 \omega_3\left(k_1 + k_3 - \omega_1 \omega_3\right)\right\}\left\{\omega_4^3\left(\omega_1 - \omega_3\right) - \mathbf{k}_4 \cdot \left(\mathbf{k}_1 - \mathbf{k}_3\right)\right\}/6$$

$$- \left\{\mathbf{k}_3 \cdot \mathbf{k}_4 - \omega_3 \omega_4\left(k_3 + k_4 + \omega_3 \omega_4\right)\right\}\left\{\omega_1^3\left(\omega_3 + \omega_4\right) - \mathbf{k}_1 \cdot \left(\mathbf{k}_3 + \mathbf{k}_3\right)\right\}/6$$

$$- \omega_3\left(\mathbf{k}_1 \cdot \mathbf{k}_4\right)\left\{\omega_2\left(k_1 + k_4\right) + \omega_1 \omega_4\left(\omega_1 - \omega_4\right)\right\}/6$$

$$- \omega_4\left(\mathbf{k}_1 \cdot \mathbf{k}_3\right)\left\{\omega_2\left(k_1 + k_3\right) + \omega_1 \omega_3\left(\omega_1 - \omega_3\right)\right\}/6$$

$$- \omega_1\left(\mathbf{k}_3 \cdot \mathbf{k}_4\right)\left\{\omega_2\left(k_3 + k_4\right) + \omega_3 \omega_4\left(\omega_4 + \omega_4\right)\right\}/6$$

$$+ \omega_1 \omega_3 \omega_4\left\{\omega_3^5 + \omega_4^5 - \omega_1^5 - \omega_2^2\left(\omega_3^3 + \omega_4^3 - \omega_1^3\right)\right\}/6 \qquad .$$

The configurations of interacting quadruplets are illustrated in Fig. 2.1 for deep water. A projection of the resonant loops in three dimensions onto the wavenumber plane as shown in Fig. 2.1 is utilized. This figure determines the sets of wave numbers for surface waves capable of undergoing resonant interactions. If k_3 and k_4 are fixed, the resonant conditions determine k_1 and k_2, leaving one degree of freedom in the resonant conditions. It is clearly understood from Fig. 2.1 that for given k_3 and k_4, k_1 (or k_2) must lie on the curve where $\gamma =$ constant. Masuda (1980) derived the approximate solution around the singular point ($\gamma = 0$) of the Boltzmann integral to develop an accurate computational scheme for nonlinear energy transfer of deep water gravity waves.

The most significant advance in the wave spectral model for nonlinear energy transfer was the development of the discrete-interaction approximation (DIA) by Hasselmann et al. (1985). Hasselmann et al., (1985) introduced several simplifications to the computation of nonlinear energy transfer that improve computational time. They showed that the DIA preserves a few but important characteristics of the full solution, such as slow downshifting of the peak frequency

and shape stabilization during wave growth (Cavaleri et al., 2007). Currently, the DIA has been adopted by almost all of the third-generation wave prediction models.

Although the development of the DIA partly accomplishes the deficiency of the exact method, the DIA has some drawbacks. The DIA does not have sufficient accuracy for sharp-pointed shape spectra, such as the Joint North Sea Wave Project (JONSWAP)-type spectrum, although it gives good performance for broad shape spectra, such as the Pierson–Moskowitz (PM) spectrum (Hashimoto and Kawaguchi, 2001).

Various efforts have been made to develop nonlinear energy transfer computation. Extensions of the DIA method have been proposed by adding the number of wave configurations. Proposals for the multiple DIA were made by Van Vledder et al. (2000), Hashimoto and Kawaguchi (2001), and more recently by Tolman (2004). Hashimoto and Kawaguchi (2001) developed the extended DIA (EDIA) and multiple DIA (MDIA). Recently, Tolman (2004) has developed a generalized multiple DIA (GMD) to be adopted in WAVEWATCH III.

Another alternative to nonlinear energy transfer computation have been developed by Komatsu (1993) and Komatsu and Masuda (1996), who developed the RIAM and SRIAM method based on Masuda's method. Komatsu et al. (1993) developed the RIAM method and showed that it preserves the same degree of accuracy and smoothness as the exact method by modifying Masuda's method with the use of symmetry characteristics of four-wave resonances. The computation using the RIAM method is 300 times faster than that using Masuda's method, although it is restricted to deep water wave applications. Komatsu and Masuda (1996) simplified the RIAM method to the SRIAM method, which makes the computation 100 times faster than the RIAM method. The SRIAM method, however, requires a computation time 20 times longer than the DIA method. Although the SRIAM method is one of the important progresses in optimizing the interactions, it is more computationally expensive than the DIA method and hence economically unacceptable for practical models at the moment (Tolman, 2003).

In the past, several attempts also were made to nonlinear energy transfer computations in finite-depth conditions. The nonlinear energy transfer for finite-water depths in the wave action model (WAM) and simulating waves nearshore (SWAN) model is approximated by multiplying the deep-water transfer rate (computed in the DIA) by a depth dependent scaling factor R. Although this approximation is convenient, the first-order representation of the change in nonlinear energy

transfer does not capture the frequency shift and spectral shape changes that decrease as the water depth increases. Hashimoto et al. (1998) proposed a computational method for calculating nonlinear energy transfer in finite-water depth wave spectra by extending the exact method of Masuda (1980) and Komatsu and Masuda (1996) for deep water waves. The method is called the finite-depth RIAM (FD-RIAM). It is also applicable to deep water as the latter is a special case of finite-depth water.

This chapter explains previous approximations of nonlinear energy transfer computation methods, such as the DIA, MDIA, EDIA, RIAM, SRIAM, and FD-RIAM methods, which are considered the most promising methods to be used in practical wave models.

2.2 Discrete-Interaction Approximation Method

Since the Boltzmann integral in Eq. (2.3) consists of multidimensional integration, a complicated coupling coefficient, and two delta functions corresponding to resonance conditions, its solution is computationally expensive for applications in wave models. Hasselmann et al. (1985) developed the DIA method and successful in increasing the speed of computation for practical applications.

The full solution to the Boltzmann integral in Eq. (2.3) uses a very large set of wave quadruplets with many different configurations, whereas the DIA uses a small number of quadruplets with the same configuration. The resonant conditions are expressed as

$$
\left.\begin{array}{l}
\omega_1 = \omega_2 = \omega \\
\omega_3 = \omega(1+\lambda) = \omega_+ \\
\omega_4 = \omega(1-\lambda) = \omega_- \\
\theta_1 = \theta_2 = \theta
\end{array}\right\}
\qquad
\left.\begin{array}{l}
\theta_3 - \theta = \pm\cos^{-1}\left\{\dfrac{1+2\lambda+2\lambda^3}{(1+\lambda)^2}\right\} \\[4mm]
\theta_4 - \theta = \mp\cos^{-1}\left\{\dfrac{1-2\lambda-2\lambda^3}{(1+\lambda)^2}\right\}
\end{array}\right\}
\qquad (2.4)
$$

where λ is a constant determining the combination of the component waves. Hasselmann et al (1985) set $\lambda = 0.25$ based on numerical experiments. The rates of change in the energy densities $(\delta_{nl}, \delta_{nl}^+, \delta_{nl}^-)$ with a focus only on the configuration and the simplified Boltzmann integral are given by

$$\begin{Bmatrix} \delta S_{nl} \\ \delta S_{nl}^{+} \\ \delta S_{nl}^{-} \end{Bmatrix} = \begin{Bmatrix} -2(\Delta\omega\Delta\theta)/(\Delta\omega\Delta\theta) \\ (1+\lambda)(\Delta\omega\Delta\theta)/(\Delta\omega_{+}\Delta\theta) \\ (1-\lambda)(\Delta\omega\Delta\theta)/(\Delta\omega_{-}\Delta\theta) \end{Bmatrix} \times C\omega^{11}g^{-4}\left[F^2\left\{ \frac{F_{+}}{(1+\lambda)^4} + \frac{F_{-}}{(1-\lambda)^4} \right\} - 2\frac{FF_{+}F_{-}}{(1-\lambda^2)^4} \right], \qquad (2.5)$$

where $F \equiv F(\omega,\theta)$, $F_{+} \equiv F(\omega_{+},\theta)$, and $F_{-} \equiv F(\omega_{-},\theta)$ are the energy densities for the values of the interacting wave numbers, g is the gravitational acceleration, and C is a constant equal to 3×10^7. The six dimensional integral in Eq. (2.3) is replaced by a single loop over the discrete spectral space, and the complicated coefficient G is replaced by a constant C. These replacements lead to acceleration of the computation.

However, the DIA has a drawback of deficiency for applications in operational wave models. Furthermore, it has been known that an improvement of the DIA necessitates the development of the third-generation wave model.
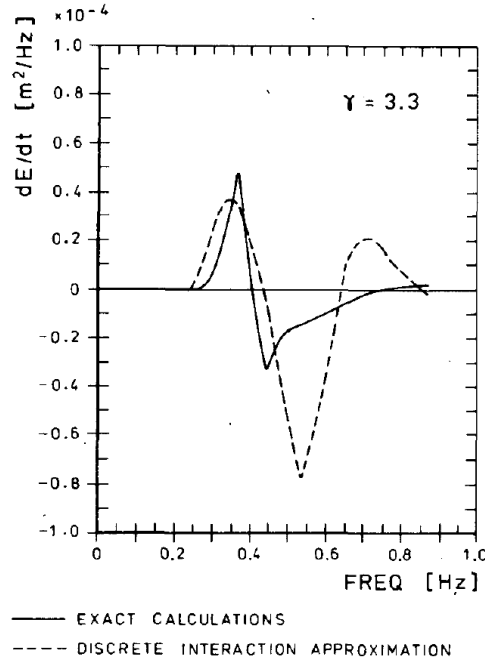
Figure 2.2. Comparison of the exact one-dimensional distribution S_{nl} with that in the DIA for a JOSWAP-type spectrum. Adapted from "Computations and Parameterizations of the Nonlinear Energy Transfer in a Gravity-Wave Spectrum. Part I: A New Method for Efficient Computations of the Exact Nonlinear Transfer Integral" by Hasselmann, S. and K. Hasselmann, 1985, Journal of Physical Oceanography, Vol. 15, 1378-1391. Copyright (1985), American Meteorogical Society.

A comparison of the DIA method and the exact method for the JONSWAP spectrum is shown in Fig. 2.2. It can be seen that the DIA result in a numerical wave model gives a significant overestimation of the wave energy spectral at high frequencies. However, Hasselman et al.

12

(1985) asserted this value is less important for a satisfactory reproduction of wave growth than the correctly simulated form of the positive lobe. The latter controls the rate at which the spectral peak shift towards low frequencies. The strength of the DIA is not in its accuracy, but in its preservation of conservation of energy, action, and momentum, together with the resonance conditions (Tolman, 2003).

2.3 Research Institute for Applied Mechanics Method

The RIAM method was developed based on the seminal work of Masuda (1980). Hereafter, Masuda does not explicitly write the conditions $|\mathbf{k}_1| \leq |\mathbf{k}_2|$, $|\omega_1| \leq |\omega_2|$ for simplicity. The integration over $k2$ can be written as

$$\frac{\partial n_4}{\partial t} = 2 \iint d\mathbf{k}_3 \iint d\mathbf{k}_1 G \delta(\omega_1 + \omega_2 - \omega_3 - \omega_4) \times \{ n_1 n_2 (n_3 + n_4) - n_3 n_4 (n_1 + n_2) \}, \tag{2.6}$$

where $\mathbf{k}_2 = \mathbf{k}_3 + \mathbf{k}_4 - \mathbf{k}_1$ and $\omega_2 = |\mathbf{k}_3 + \mathbf{k}_4 - \mathbf{k}_1|^{1/2}$. Using the relation $d\mathbf{k} = 2\omega^3 d\omega d\theta$, the above equation can be written in terms of the frequency ω and propagation direction θ as

$$\frac{\partial n_4}{\partial t} = 2 \iint d\omega_3 d\theta_3 \iint d\omega_1 d\theta_1 (4\omega_1^3 \omega_3^3) \times G \delta(\omega_1 + \omega_2 - \omega_3 - \omega_4)$$
$$\times \{ n_1 n_2 (n_3 + n_4) - n_3 n_4 (n_1 + n_2) \} \tag{2.7}$$

where the energy density $T(\omega, \theta) = 2\omega^4 n(\mathbf{k})$ is introduced. Then, substituting the energy density into Eq. (2.7) yields

$$T(\omega_4, \theta_4) = 2\omega_4^4 \iint d\omega_3 d\theta_3 \iint d\omega_1 d\theta_1 (8\omega_1^3 \omega_3^3 G) \times \delta(\omega_1 + \omega_2 - \omega_3 - \omega_4)$$
$$\times \{ n_1 n_2 (n_3 + n_4) - n_3 n_4 (n_1 + n_2) \} \tag{2.8}$$

As is well known, the delta function in Eq. (2.3) indicates that nonlinear energy transfer occurs when resonant conditions are satisfied. Figure (2.1) shows that for given k_3 and k_4, k_1 (or k_2) must lie on the curve γ = constant. Masuda adopted $\theta_1 - \theta_a$ as the parameter representing the remaining degree of freedom, where θ_a is the direction of $\mathbf{k}_a$. Then, the frequency ω_1 is obtained by solving the following algebraic equation of third order:

$$4\omega_a \omega_1^3 - \left[2\mathbf{k}_a \cos(\theta_1 - \theta_a) + 6\omega_a^2 \right] \times \omega_1^2 + 4\omega_a^3 \omega_1 + \left(\mathbf{k}_a^2 - \omega_a^2 \right) = 0. \tag{2.9}$$

Form the condition $|\mathbf{k}_1| \le |\mathbf{k}_2|$ or $|\omega_1| \le |\omega_2|$, we note that for $\gamma < 0$, $\theta_1 - \theta_a$ is restricted to the range $\theta \le |\theta_1 - \theta_a| \le \pi$. The integration in Eq. (2.8) over ω_1 yields

$$T(\omega_4, \theta_4) = (2\omega_4^{23}) \int_{-\pi}^{\pi} d\tilde{\theta}_3 \int_0^{\infty} d\tilde{\omega}_3 \int_{-\pi}^{\pi} d\tilde{\theta}_1 \times (8\tilde{\omega}_1^3 \tilde{\omega}_3^4 \tilde{G} S^{-1})$$
$$\times \{n_1 n_2 (n_3 + n_4) - n_3 n_4 (n_1 + n_2)\}$$
(2.10)

where the transformation variables are given by $\tilde{\theta}_1 = \theta_1 - \theta_a$, $\tilde{\theta}_3 = \theta_3 - \theta_4$, $\tilde{\omega}_2 = \omega_2 / \omega_4$, $\mathbf{k}_a = \mathbf{k}_a / \omega_4^2$, and $G = G / \omega_4^{12}$.

It can be seen that G, $\tilde{S}$, ω_1, etc., depend on the configuration of wave resonances. If $\tilde{\Omega} = \ln \tilde{\omega}_3$ is introduced, the energy density $T(\omega, \theta)$ becomes

$$T(\omega_4, \theta_4) = (2\omega_4^{23}) \int_0^{\pi} d\tilde{\theta}_3 \int_0^{\infty} d\tilde{\Omega} \int_0^{\pi} d\tilde{\theta}_1 \times \sum_{\pm} \sum_{\pm} \sum_{\pm} (8\tilde{\omega}_1^3 \tilde{\omega}_3^4 \tilde{G} S^{-1})$$
$$\times \{n_1 n_2 (n_3 + n_4) - n_3 n_4 (n_1 + n_2)\}$$
(2.11)

where

$$\int_{-\pi}^{\pi} d\tilde{\theta}_3 \int_0^{\infty} d\tilde{\Omega} \int_{-\pi}^{\pi} d\tilde{\theta}_1$$

has been replaced by

$$\int_0^{\pi} d\tilde{\theta}_3 \int_0^{\infty} d\tilde{\Omega} \int_0^{\pi} d\tilde{\theta}_1 \times \sum_{\pm} \sum_{\pm} \sum_{\pm}$$

Equation (2.11) is the final formula used by Masuda (1980) to calculate nonlinear energy transfer, where the denominator S arises from $\delta(\omega_1 + \omega_2 - \omega_3 - \omega_4)$ and is given by

$$S = \left| 1 + (\omega_1 / \omega_2) \{ (\omega_1 / \omega_2)^2 - (|\mathbf{k}_a| / \omega_2^2) \cos(\theta_1 - \theta_a) \} \right|.$$
(2.12)

This final formula makes it sufficient to calculate complicated functions such as G, S, etc., only once, thus reducing the computation time. Figure 2.3. shows schematically the domain of integration in the $(\tilde{\theta}_1, \tilde{\Omega}, \tilde{\theta}_3)$ space. It is an infinitely long rectangular prism, excluding the lower region because of the condition $\omega_1 \le \omega_2$. This excluded volume is bounded by three planes $\tilde{\theta}_3 = \pi$, $\tilde{\Omega} = 0$, and $\tilde{\theta}_1 = 0$, and the curved surface $\tilde{\theta}_1 = \theta(\tilde{\theta}_3, \tilde{\Omega})$. The singular points caused by the denominator S^{-1} are located along the curve $\gamma = |\mathbf{k}_a|^{-1/2} \omega_a^{-1} - 2^{-1/2} = 0$ in the plane $\tilde{\theta}_1 = 0$.

As Masuda noted, numerical instability in the integral in Eq. (2.11) is caused mainly by an inappropriate treatment of the singular points. Masuda, hence, solved this instability problem by analytically deriving an approximate solution of Eq. (2.11) around the singular points.

14
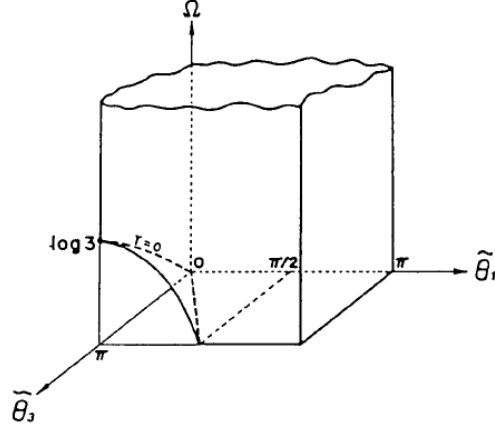
Figure 2.3. A schematic graph of the region over which the integral in Eq. (2.11) is performed. Adapted from "Nonlinear energy transfer between wind waves", by Masuda, 1980, Journal of Physical Oceanography, Vol.10, 2082-2092. Copyright (1980), American Meteorogical Society.

Although Masuda's method improves the computational time of nonlinear energy transfer computation, it is still time consuming and impractical to be incorporated into wave models. Therefore, Komatsu and Masuda (1996) developed a new scheme called the RIAM method. The RIAM method deals with about 2000 configurations out of an infinite number using the symmetry of the resonant interaction pointed out by Hasselmann and Hasselmann (1981) and truncates the less substantial resonance configurations in Masuda's method.

In the RIAM method, two kinds of symmetries are discriminated from each other (Komatsu and Masuda, 1996). The first kind is that $\delta n(\mathbf{k}_i)d\mathbf{k}_i/\delta t$ (i = 1, 2, 3, 4) have the following relationship (Hasselmann and Hasselmann, 1981):

$$\frac{\delta n(\mathbf{k}_1)}{\delta t}d\mathbf{k}_1 = \frac{\delta n(\mathbf{k}_2)}{\delta t}d\mathbf{k}_2 = -\frac{\delta n(\mathbf{k}_3)}{\delta t}d\mathbf{k}_3 = -\frac{\delta n(\mathbf{k}_4)}{\delta t}d\mathbf{k}_4 , \qquad (2.13)$$

where $\delta n(\mathbf{k})/\delta t$ indicates the action transfer caused by this particular resonance combination. As shown in Eq. (2.13), $\delta n(\mathbf{k}_i)d\mathbf{k}_i/\delta t$ (i = 1, 2, 3, 4) are of equal magnitude but differ in sign. Accordingly, if we calculate $\delta n(\mathbf{k})/\delta t$ for one component of the resonant four waves, then we immediately know $\delta n(\mathbf{k})/\delta t$ for the other three components. The above action transfers for the four waves are converted to the corresponding nonlinear energy transfers because of the specific combination of resonances δT^{LO}, δT^{LI}, δT^{HI}, and δT^{HO}, where the suffixes LO, LI, HI, and HO denote the components for the lower frequency of the outer pair (LO component), the lower

15

frequency of the inner pair (LI component), the higher frequency of the inner pair (HI component), and the higher frequency of the outer pair (HO component), respectively.

The second kind of symmetry is associated with geometrical similarity of the resonance configurations, which include:

(1) The mirror image of the resonance combination gives another combination with the same interaction coefficient.

(2) A rotation of the resonance combination gives another combination with the same interaction.

(3) A scale transformation of the wave number preserves the resonance condition. Nevertheless, this is valid only for deep water waves.

To make use of the symmetries mentioned above, the (ω, θ) space is divided into bins of nonuniform finite areas:

$$\omega_{k+1} = R_\omega \cdot \omega_k,$$ (2.14)

where $R_\omega \equiv 1 + \Delta(\log\omega)$. The central direction θ_m of the bin is distributed as

$$\theta_{m+1} = \theta_m + \Delta\theta,$$ (2.15)

with the directional increment $\Delta\theta$ kept constant. Based on this bin distribution, if a combination of four bins satisfies the resonance condition, so do any combination obtained by the mirror transformation, rotational transformation, and scale transformation. All the resonance combinations with the same geometry as in the above transformations are said to have the same configuration of resonance.

Finally, the procedure of the RIAM method is written schematically as

$$T = \sum_{cnf}\sum_{scl}\sum_{rot}\left(\delta T^{LO} + \delta T^{LI} + \delta T^{HI} + \delta T^{HO}\right),$$ (2.16)

where the parameters c_{nf}, s_{cl}, and r_{ot} symbolically denote the configuration, scale, and rotation (plus mirror image), respectively. The summation over the LO, LI, HI, and HO components represents the symmetry of the first kind, while the summation over c_{nf}, s_{cl}, and r_{ot} corresponds to the second kind of symmetry. In order to limit the number of resonance combinations, Komatsu

16

and Masuda discarded the resonance configurations for which the ratio of the higher and lower frequencies of the outer pair, ω^{HO}/ω^{LO}.

In the RIAM method, energy transfer is calculated for each bin. When we fix c_{nf}, s_{cl}, r_{ot}, and a bin corresponding to the HO component (HO bin), the locations of the other three resonant bins relative to the HO bin in the frequency-direction space are determined by the c_{nf} parameter. The rate of energy the HO bin receives from the resonance in the four bins of assigned areas is calculated as

$$dT^{HO} = G_1(cnf).G_2(scl)(n^{LI}n^{HI}(n^{LO}+n^{HO})-n^{LO}n^{HO}(n^{LI}+n^{HI})), \tag{2.17}$$

where n^{LI} is the action density for the LI bin, etc. G_1 and G_2 describe the strength of the resonant interaction between the four bins. The kernel G_1 is determined using the Masuda method, whereas G_2 is a simple power of the frequency of the HO bin (Masuda, 1980). Note that the resonance configurations and the two factors G_1 and G_2 are independent of the spectrum.

Once δT^{HO} is obtained, the energy of the other resonant bins can be easily calculated using the symmetry of the first kind. Then, the total nonlinear energy transfer as expressed in Eq. (2.16) can be obtained. To eliminate overlap computations, we assume the following sequence of frequencies:

$$\omega_3 \leq \omega_1 \leq \omega_2 \leq \omega_4. \tag{2.18}$$

Figure 2.4 shows a comparison of the one-dimensional nonlinear energy transfer functions T_1 obtained using the RIAM method, WAM method in the DIA, and the previous rigorous algorithms of Masuda (1980), Hasselmann and Hasselmann (1981), and Resio and Perrie (1991), where the wave spectrum examined is the standard JONSWAP spectrum with a $\cos^2\theta$ directional spreading (Komatsu and Masuda, 1996). The RIAM method well reproduces the T obtained in Masuda method, whereas the result of the WAM method completely differs from those of the other. These results show that the RIAM method preserves the same degree of accuracy and smoothness as the Masuda method.

Although the RIAM method is 300 times faster than the Masuda method, it is still requires 2000 times longer computational time than the DIA. This is because the RIAM method uses thousands of configurations whereas the DIA method deals only with one mirror-image pair of the interaction configurations. Compared with the RIAM method, the DIA method gives quite

unrealistic nonlinear energy transfer functions both in magnitude and in pattern, when the spectrum is either directionally concentrated, frequency-concentrated, or double peaked. The DIA method is unreliable even for the standard JONSWAP spectrum.
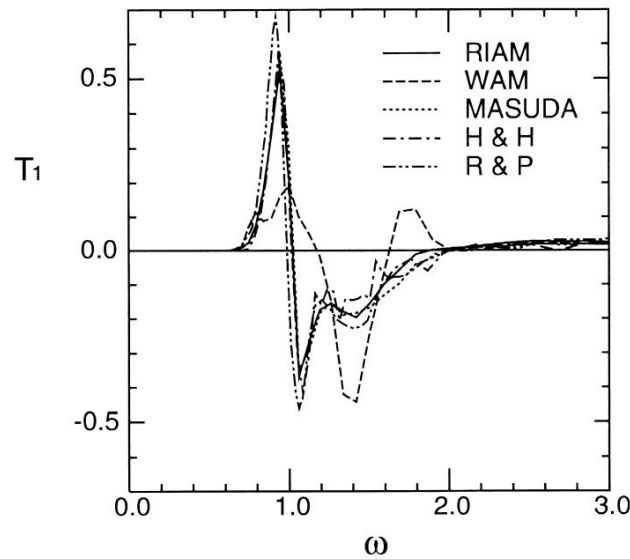
Figure 2.4. Comparison of the one-dimensional nonlinear energy transfer functions T_1 obtained using the RIAM, WAM, and by Masuda (1980), Hasselmann and Hasselmann (1981), and Resio and Perrie (1991). Adapted from "A new scheme of nonlinear energy transfer among wind waves: RIAM method − algorithm and performance" by Komatsu and Masuda, 1996, Journal of Oceanography, 52, 509-537. Copyright (1996), Springer Japan.

Komatsu and Masuda, therefore, concluded that the RIAM method is not fast enough for an operational model. The advantage of the RIAM method is to give almost the same degree of accuracy as the other exact algorithms, such as the Masuda method, even for rather atypical wave spectra. However, in any case, the RIAM method cannot be used as an algorithm for operational wave prediction. Other efficient methods with a slightly lower level accuracy need to be developed for operational wave prediction.

2.4 Simplified Research Institute for Applied Mechanics Method

As mentioned above, the most widely used method for evaluating nonlinear energy transfer is the DIA method (Hasselmann et al., 1985), because of its low computational cost. However, Komatsu and Masuda (1996) showed that the RIAM method provides better numerical stability and smoothness than the DIA method. However, the RIAM method is not economically acceptable to be implemented in operational wave models. Therefore, Komatsu (1996) decreased the number of resonance configurations to achieve less computational time without the loss of

accuracy. The resulting method is called the simplified RIAM method (SRIAM), which deals with only 20 resonance configurations.

The SRIAM method can be expressed by the following equation:

$$T(\omega_4, \theta_4) = \frac{\partial \phi_4}{\partial t} = (2\omega_4^{23}) \sum_{i=1}^{20} C_i \tilde{K}_i(\tilde{\theta}_1, \tilde{\Omega}, \tilde{\theta}_3) \{n_1 n_2 (n_3 + n_4) - n_3 n_4 (n_1 + n_2)\}_i, \qquad (2.19)$$

where $\tilde{K}_i(\tilde{\theta}_1, \tilde{\Omega}, \tilde{\theta}_3) = 8\tilde{\omega}_1^3 \omega_3^4 \tilde{G} S^{-1} \Delta\tilde{\theta}_3 \Delta\tilde{\Omega}\Delta\tilde{\theta}_1$ and C_i $(i = 1, \cdots 20)$ are coefficients. Komatsu (1996) listed the optimum 20 combinations of the resonant configurations, where seven configurations are chosen from singular points and the other 13 configurations are chosen from regular points in the $(\tilde{\theta}_1, \tilde{\Omega}, \tilde{\theta}_3)$ space. Table 2.2 shows the detailed parameters that determine each resonant configuration and the associated interaction coefficients, where i_{rep} is the number of resonant configurations, $\tilde{\theta}_3$ and $\tilde{\theta}_1$ are angles of the wave vector k_3 and k_1, $\tilde{\omega}_3$ is the normalized angular frequency $\tilde{\omega}_3$ divided by $\tilde{\omega}_4$, $\tilde{K}$ is the kernel function for a specific quadruplet, and C_{irep} is a parameter that modifies the interaction coefficient so that that optimized kernel function is evaluated as $C_{irep} \times \tilde{K}$.

The optimum resonant configurations and the coefficients C_{irep} depend on the number of selected configurations and the number of directional and frequency bins constituting the directional spectrum in the model. For practical purposes, we need to select the values which are in general applicable to various types of directional spectra. Therefore, the optimum resonant configurations and the coefficients C_{irep} have to be redetermined for each computation condition. For these reasons, the SRIAM method determines the optimum configurations and the coefficients C_{irep} using eight different energy concentrations (Table 2.1) and optimizes the interaction coefficients by minimizing the following equation:

$$E(i) = \sum_{SPj} \frac{1}{\max_k \left\{ |T_{SPj}(k)|^2 \right\}} \sum_k \left| T_{SPj}(k) - \sum_i C_{irep} T_{SPj}^i(k) \right|^2, \qquad (2.20)$$

where $T_{SPj}(k)$ is the exact value of the nonlinear energy transfer, and $C_i T_{SPj}^i(k)$ is the contribution of the ith configuration to the wave components. The optimum C_{irep} is then determined by the least-square method. The resonance configurations used in the SRIAM method are shown in Fig. 2.5. The wave vectors k_1, k_2, k_3, and k_4 for one quadruplet are indicated by arrows. Other quadruplets are specified by the symbols O and +, which represent the endpoints of the wave

vectors k_1 and k_3, respectively. Mirror images of these configurations are also considered, but are not shown in the figure. All sets of quadruplets that satisfy the resonance conditions lie on the specific curve $\gamma_{conf} =$ constant (Masuda, 1980).

Table 2.1. Eight test spectra used for the optimization of the SRIAM method, where γ is the peakedness factor and s is the directional spreading

j	γ	s
1	1.0	2
2	1.0	10
3	3.3	2
4	3.3	10
5	5.0	2
6	5.0	10
7	9.0	2
8	9.0	10

Table 2.2. Parameters determining resonant configurations and the associated interaction coefficients for the SRIAM method: singular quadruplets (i_{rep}: 1–7) and regular quadruplets (i_{rep}: 8–20)

i_{rep}	$\tilde{\theta}_1$	$\tilde{\sigma}_3$	$\tilde{\theta}_3$	γ_{conf}	$Log_{10}\tilde{K}$	C_{irep}
1	0	0.88	10	0.000	2.15	1.00
2	0	0.78	20	0.000	1.85	1.00
3	0	0.70	30	0.000	1.11	1.00
4	0	0.63	40	0.000	0.40	1.00
5	0	0.57	50	0.000	-0.29	1.00
6	0	0.52	60	0.000	-0.92	1.00
7	0	0.49	70	0.000	-1.51	1.00
8	0	0.62	30	0.009	-0.64	2.01
9	10	0.75	30	-0.004	0.98	1.96
10	10	0.68	30	0.002	0.01	1.94
11	10	0.62	40	0.001	-0.56	1.96
12	10	0.56	40	0.011	-1.46	4.60
13	10	0.51	50	0.013	-2.04	8.44
14	10	0.47	50	0.024	-2.80	2.63
15	20	0.83	40	-0.018	0.93	2.01
16	20	0.75	40	-0.013	0.38	1.62
17	20	0.68	40	-0.006	-0.28	1.79
18	20	0.62	50	-0.008	-1.00	2.67
19	20	0.56	50	0.002	-1.56	1.57
20	20	0.51	50	0.013	-2.25	1.53

Figure 2.5. Interaction diagram in the wave number plane for the resonance configurations used in the SRIAM method and the contours of γ_{conf} defined by Masuda (1980). Wave vectors k_1, k_2, k_3, and k_4 for one quadruplet are indicated by arrows. Other quadruplets are specified with the symbols O and +, which represent the end points of the wave vectors k_1 and k_3, respectively. Adapted from "Current-Induced Modulation of the Ocean Wave Spectrum and the Role of Nonlinear Energy Transfer" by Tamura, 2008, Journal of Physical Oceanography, Vol. 38, 2662-2984. Copyright (2008), American Meteorogical Society.
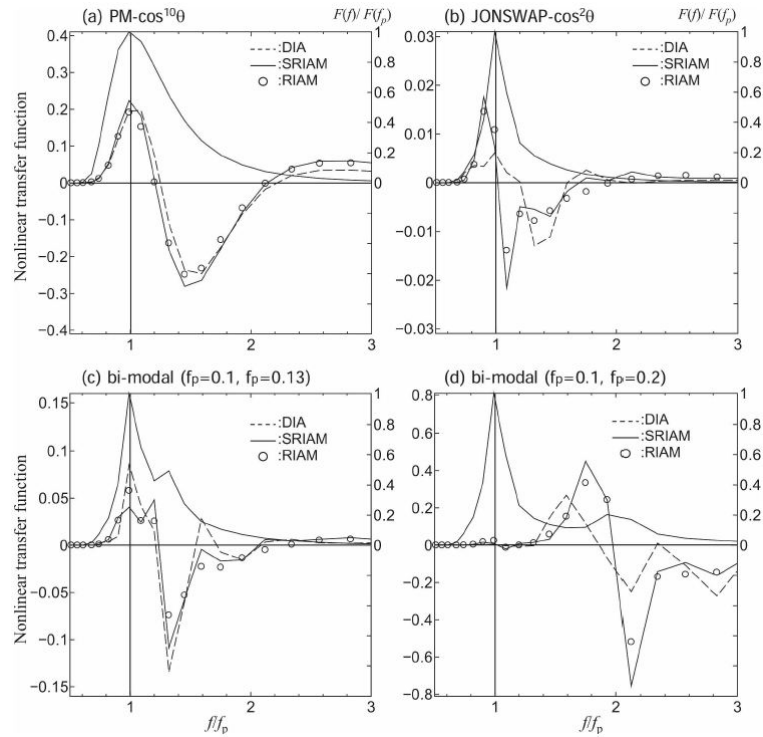
Figure 2.6. Comparison of one-dimensional nonlinear energy transfer calculations in the SRIAM, RIAM, and DIA methods. The wave spectra examined are the (a) Pierson–Moskowitz spectrum, (b) standard JONSWAP spectrum, and double-peaked spectra in the frequency domain for (c) $f_{p1} = 0.1$ and $f_{p2} = 0.13$, and (d) $f_{p1} = 0.1$ and $f_{p2} = 0.2$ Adapted from "Current-Induced Modulation of the Ocean Wave Spectrum and the Role of Nonlinear Energy Transfer" by Tamura, 2008, Journal of Physical Oceanography, Vol. 38, 2662-2984. Copyright (2008), American Meteorogical Society.

It is clearly shown in Fig. 2.6 that the SRIAM method has practical applicability in complex situations, especially for the JONSWAP spectrum and the double-peaked spectra, while the DIA method does not. The SRIAM method has a slightly lower level of accuracy than the RIAM method; however, its computation time is 100 times faster than that of the RIAM method. Thus, as for accuracy and flexibility, the SRIAM method is almost perfect to be used in practical wave models. However, the SRIAM method has computational time 20 times longer than the DIA method.

2.5 Modified and Extended Discrete-Interaction Approximation Methods

Hashimoto and Kawaguchi (2001) examined the validity and effectiveness of the original DIA method and demonstrated that the accuracy of the method can be improved as the number of the configurations increases. Following Ueno (1997), Hashimoto and Kawaguchi (2001) found an improvement of the nonlinear energy transfer computation using only a few configurations. The EDIA method improves the DIA method by increasing the number of configurations. The EDIA can be expressed as

$$
\begin{Bmatrix} \delta S_{nl} \\ \delta S_{nl}^+ \\ \delta S_{nl}^- \end{Bmatrix} = \sum_i \begin{Bmatrix} -2(\Delta\omega\Delta\theta)/(\Delta\omega\Delta\theta) \\ (1+\lambda_i)(\Delta\omega\Delta\theta)/(\Delta\omega_+\Delta\theta) \\ (1-\lambda_i)(\Delta\omega\Delta\theta)/(\Delta\omega_-\Delta\theta) \end{Bmatrix} \times C_i \omega^{11} g^{-4} \left[F^2 \left\{ \frac{F_+}{(1+\lambda_i)^4} + \frac{F_-}{(1-\lambda_i)^4} \right\} - 2 \frac{FF_+F_-}{(1-\lambda_i^2)^4} \right]. \quad (2.20)
$$

Hashimoto and Kawaguchi (2001) used the same independent parameter as those in the DIA method, i.e., the independent parameters for EDIA are λ_i and C_i. Each of the wave configurations added into the original DIA equation has different parameters λ_i and C_i. The MDIA was obtained by adding the parameters $C_{i,1}$ and $C_{i,2}$ to the EDIA. It is expressed as

$$
\begin{Bmatrix} \delta S_{nl} \\ \delta S_{nl}^+ \\ \delta S_{nl}^- \end{Bmatrix} = \sum_i \begin{Bmatrix} -2(\Delta\omega\Delta\theta)/(\Delta\omega\Delta\theta) \\ (1+\lambda_i)(\Delta\omega\Delta\theta)/(\Delta\omega_+\Delta\theta) \\ (1-\lambda_i)(\Delta\omega\Delta\theta)/(\Delta\omega_-\Delta\theta) \end{Bmatrix} \omega^{11} g^{-4} \left[C_{1,i} F^2 \left\{ \frac{F_+}{(1+\lambda_i)^4} + \frac{F_-}{(1-\lambda_i)^4} \right\} - 2C_{2,i} \frac{FF_+F_-}{(1-\lambda_i^2)^4} \right]. \quad (2.21)
$$

Hashimoto and Kawaguchi (2001) have demonstrated that the parameter λ used in the original DIA is most accurate for the PM spectrum and Mitsuyatsu-type directional function with $S_{max} = 10$, and that the error between the DIA and exact values increases as the energy concentration increases. Thus, the optimum values of the parameters λ and C used in the DIA method depend on the directional spectrum. The optimum values of λ and C for various configuration numbers in the EDIA and MDIA methods are shown in Tables 2.3 and 2.4, respectively.

Table 2.3. Optimum values of λ and C in the EDIA method.

No. of Conf	λ	C
1	0.19	2.97
2	0.16	2.43
	0.27	0.92
3	0.01	-10.64
	0.16	2.51
	0.27	0.91
4	0.14	34.80
	0.15	-67.02
	0.16	35.61
	0.3	0.56
5	0.1	-5.01
	0.11	9.87
	0.15	-17.76
	0.16	15.92
	0.29	0.64
6	0.08	8.77
	0.09	-13.82
	0.11	10.02
	0.15	-15.92
	0.16	14.41
	0.29	0.65

Table 2.4. Optimum values of λ and C in the MDIA method.

No. of conf	λ	C_1	C_2
1	0.19	3.09	3.35
2	0.13	1.21	-1.13
	0.27	0.68	-0.49
3	0.09	5.74	20.05
	0.12	2.49	-7.69
	0.27	0.25	-2.45
4	0.1	4.3	25.85
	0.11	1.81	-14.78
	0.17	0.45	-1.79
	0.28	0.57	-0.12
5	0.1	1.29	13.66
	0.11	4.11	-6.51
	0.15	-7.96	-0.12
	0.16	8.04	0.51
	0.29	0.53	0.04
6	0.06	1.41	-1.28
	0.09	-9.22	-5.27
	0.11	12.86	7.34
	0.12	-4.93	2.7
	0.16	2.38	-0.59
	0.28	0.48	-0.51

Note : Table 2.3 and Table 2.4 are adapted from "Extension and Modification of Discrete Interaction Approximation (DIA) for Computing Nonlinear Energy Transfer of Gravity Wave Spectra" by Hashimoto, N and K. Kawaguchi, 2001, Proc. 4th Int. Symp. Waves 2001, 530-539. Copyright (2002), American Society of Civil Engineers.
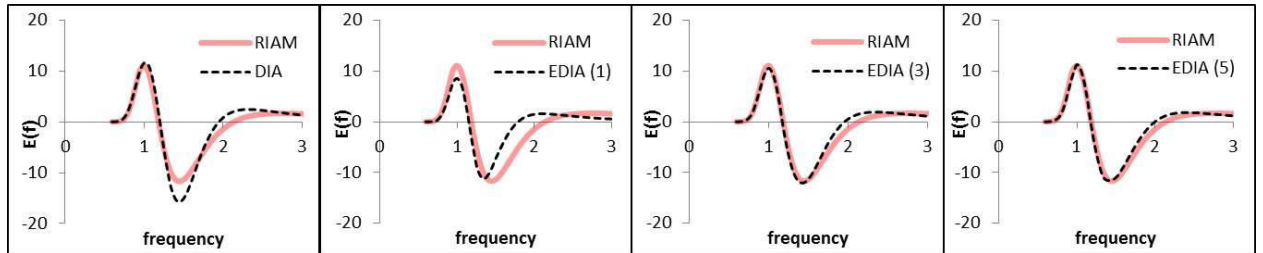
Figure 2.7. Examples of the nonlinear energy transfer computations for the PM Spectrum ($S_{max} = 10$)
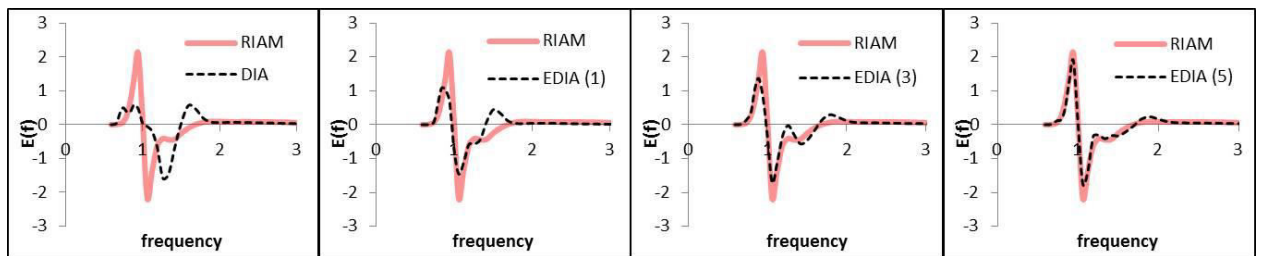
Figure 2.8. Examples of the nonlinear energy transfer computations for the JONSWAP spectrum ($S_{max} = 10$)

Hashimoto and Kawaguchi (2001) confirmed that in the WAM, the EDIA has a higher adaptability to the JONSWAP spectrum than the traditional DIA, but its adaptability to the PM spectrum decreased slightly. The accuracy of the EDIA is better than that of the original DIA (Figs. 2.7 and 2.8). Whereas the MDIA is generally more accurate than the EDIA, the MDIA equation is needed to be resolved whether the characteristics of the Boltzmann integral, such as the conservation of total energy, total momentum, and total wave action, are satisfied or not. The MDIA can be generally accurate, but it requires dynamical adjustment of the parameter settings (Tolman, 2003).

2.6 Finite-Depth Research Institute for Applied Mechanics Method

Although the RIAM, SRIAM, and M DIA methods have much better accuracy than the DIA method, they can only be applied to deep water. Hashimoto et al. (1998) developed a computational method for finite-depth gravity waves by extending the methods of Masuda (1980) and Komatsu et al. (1993). This refined method has the advantage that it can be applied to deep and finite water depth waves.

Hashimoto et al. (1998) reduced the Boltzmann integral by extending the Masuda formulation for deep water waves to a finite water depth based on Masuda's derivation (1980). Using the relations

$$d\mathbf{k} = \frac{\mathbf{k}}{C_g(\mathbf{k})} d\omega d\theta \tag{2.21}$$

and

$$\frac{\Phi(\omega,\theta)}{\omega} d\omega d\theta = n(\mathbf{k}) d\mathbf{k} , \tag{2.22}$$

we have

$$\frac{\partial \Phi(\omega_4,\theta_4)}{\partial t} = \frac{2\omega_4 \mathbf{k}_4}{C_g(\mathbf{k}_4)} \iint d\omega_3 d\theta_3 \iint d\omega_1 d\theta_1 \left\{ \frac{\mathbf{k}_1 \mathbf{k}_3}{C_g(\mathbf{k}_1) C_g(\mathbf{k}_3)} G \right\}.$$
$$\times \delta(\omega_1 + \omega_2 - \omega_3 - \omega_4) \left\{ n_1 n_2 (n_3 + n_4) - n_3 n_4 (n_1 + n_2) \right\} \tag{2.23}$$

Using the parameter γ, Masuda derived an approximate solution of the Boltzmann integral around the singular point ($\gamma = 0$) and used the solution to develop an accurate computational scheme for

determining nonlinear energy transfer in deep-water waves. Taking into consideration the effect of finite-water depth, Hashimoto et al. (1998) redefined the parameter γ as

$$\gamma = \sqrt{g\mathbf{k}_a \tanh \frac{\mathbf{k}_a}{2} h} \Big/ \omega_a - 1/\sqrt{2} \,. \tag{2.24}$$

Note that the parameter γ is zero at the singular points and that when h approaches infinity, γ is identical to that in Masuda's definition.

Integrating Eq. (2.23) over ω_1 yields

$$\frac{\partial \Phi(\omega_4, \theta_4)}{\partial t} = \frac{2\omega_4 \mathbf{k}_4}{C_g(\mathbf{k}_4)} \iint d\omega_3 d\theta_3 \int d\theta_1 \times \left\{ \frac{\mathbf{k}_1 \mathbf{k}_3}{C_g(\mathbf{k}_1) C_g(\mathbf{k}_3)} \frac{G}{S} \right\} \left\{ n_1 n_2 (n_3 + n_4) - n_3 n_4 (n_1 + n_2) \right\}, \tag{2.25}$$

where the denominator S arises from $\delta(\omega_1 + \omega_2 - \omega_3 - \omega_4)$ and is given by

$$S = \left| 1 + \frac{C_g(\mathbf{k}_2)}{C_g(\mathbf{k}_1)} \left\{ \frac{\mathbf{k}_1 - \mathbf{k}_a \cos(\theta_1 - \theta_a)}{\mathbf{k}_2} \right\} \right|, \tag{2.26}$$

where $\tilde{\theta}_1 = \theta_1 - \theta_a$, $\tilde{\theta}_2 = \theta_2 - \theta_a$, $\tilde{\theta}_3 = \theta_3 - \theta_4$, and $\tilde{\Omega} = \ln \tilde{\omega}_3$.

Equation (2.25) can be transformed to the following formula to calculate nonlinear energy transfer:

$$\frac{\partial \Phi(\omega_4, \theta_4)}{\partial t} = \frac{2\omega_4 \mathbf{k}_4}{C_g(\mathbf{k}_4)} \int_0^\pi d\tilde{\theta}_3 \int_0^\infty d\Omega \int_0^\pi d\tilde{\theta}_1 \times \sum_{\pm} \sum_{\pm} \sum_{\pm} \left\{ \frac{\mathbf{k}_1 \mathbf{k}_3}{C_g(\mathbf{k}_1) C_g(\mathbf{k}_3)} \frac{G}{S} \right\}, \tag{2.27}$$

$$\times \left\{ n_1 n_2 (n_3 + n_4) - n_3 n_4 (n_1 + n_2) \right\}$$

where

$$\int_{-\pi}^{\pi} d\tilde{\theta}_3 \int_{-\infty}^{\infty} d\Omega \int_{-\pi}^{\pi} d\tilde{\theta}_1 \tag{2.28}$$

has been replaced by

$$\int_0^\pi d\tilde{\theta}_3 \int_0^\infty d\Omega \int_0^\pi d\tilde{\theta}_1 \times \sum_{\pm} \sum_{\pm} \sum_{\pm} \,. \tag{2.29}$$

Figure 2.4 schematically shows the integration domain in the $(\tilde{\theta}_1, \Omega, \tilde{\theta}_3)$ space for the condition $\omega_1 \leq \omega_2$. With this condition, S vanishes only when $\omega_1 = \omega_2$ and $\tilde{\theta}_1 = 0$, i.e., the singular points are located along the curve $\gamma = 0$ in the plane $\tilde{\theta}_1 = 0$ (see Fig. 2.4). Therefore, special treatment is required to perform the integration in Eq. (2.27) around the singular point $\gamma = 0$.

Masuda also introduced a transformation of the frequency ω by dividing ω by the target frequency ω_4, at which nonlinear energy transfer is to be calculated. Nevertheless, the benefit of Masuda's transformation in significantly reducing the computational time for deep water waves is not valid for finite water waves.
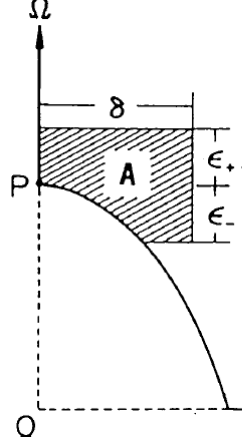
Figure 2.9. Schematic of the cross section ($\tilde{\theta}_3$ = constant) of the rectangular prism in Fig. 2.4. Adapted from "Nonlinear energy transfer between wind waves", by Masuda, 1980, Journal of Physical Oceanography, Vol.10, 2082-2092. Copyright (1980), American Meteorical Society.

The integration in Eq. (2.27) is carried out successively on the order of $\left(\tilde{\theta}_1, \Omega, \tilde{\theta}_3\right)$. Therefore, Hashimoto et al. (1998) integrated Eq. (2.27) first in the plane $\tilde{\theta}_3$ = constant. The singular point is denoted by P in Fig. 2.9. We can rewrite the integration as

$$\iint_A d\Omega d\tilde{\theta}_1 \frac{R}{S} \approx R_P \iint_A d\Omega d\tilde{\theta}_1 \frac{1}{S_P},$$

(2.30)

where the numerator R is given by

$$R = \frac{\mathbf{k}_1 \mathbf{k}_3 \omega_3 G}{C_g(\mathbf{k}_1) C_g(\mathbf{k}_3)} \left\{ n_1 n_2 (n_3 + n_4) - n_3 n_4 (n_1 + n_2) \right\},$$

(2.31)

R_P is the value of R at the singular point P, and S_P is given by

$$S_P = \sqrt{-\frac{2\mathbf{k}_a D_g(\mathbf{k}_a/2)}{C_g(\mathbf{k}_a/2)} \tilde{\theta}_1^2 - \frac{4\sqrt{2}\omega_a D_g(\mathbf{k}_a/2)}{\left\{C_g(\mathbf{k}_a/2)\right\}^2} \mu(\Omega - \Omega_p)},$$

(2.32)

where $D_g(k_a) = \partial C_g(k)/\partial k$ and

$$\mu = \left(\frac{\partial \gamma}{\partial \Omega}\right)_P = \left(\omega_3 \frac{\partial \gamma}{\partial \omega_3}\right)_{\gamma=0} = \frac{\omega_3}{\sqrt{2}\omega_a} \left\{ \frac{C_g(\mathbf{k}_a/2)}{C_g(\mathbf{k}_3)} \frac{\mathbf{k}_3 + \mathbf{k}_4 \cos \tilde{\theta}_3}{\mathbf{k}_a} - 1 \right\}.$$

(2.33)

Referring to Fig. 2.11, the integration in Eq. (2.30) can be performed by separating the area A as

$$\iint_A d\Omega d\tilde{\theta}_1 \frac{1}{S_P} = \int_{-\varepsilon_-}^0 d\Omega \int_\Theta^0 d\tilde{\theta}_1 \frac{1}{S_P} + \int_0^{\varepsilon_+} d\Omega \int_0^\delta d\tilde{\theta}_1 \frac{1}{S_P} .$$
(2.34)

Because around $\gamma \approx 0$ the lower limit Θ of the integral in the first term on the right-hand side of Eq. (2.34) can be approximated in terms of $\tilde{\theta}_1$ by

$$\Theta = \sqrt{-\frac{2\sqrt{2}\omega_a}{\mathbf{k}_a C_g (\mathbf{k}_a / 2)} \mu (\Omega - \Omega_p)} ,$$
(2.35)

the integration in Eq. (2.34) can be evaluated as

$$\iint_A d\Omega d\tilde{\theta}_1 \frac{1}{S_P} = \frac{\varepsilon_+}{\sqrt{a}} \ln \frac{\left| \sqrt{a}\delta + \sqrt{a\delta^2 - b\varepsilon_+} \right|}{\sqrt{b\varepsilon_+}} - \delta \frac{\sqrt{a}\delta + \sqrt{a\delta^2 - b\varepsilon_+}}{b}$$
$$+ \frac{\varepsilon_-}{\sqrt{a}} \ln \frac{\left| \sqrt{a}\delta + \sqrt{a\delta^2 - b\varepsilon_-} \right|}{\left| \left(\sqrt{ac} + \sqrt{ac-b} \right) \sqrt{\varepsilon_-} \right|} + \delta \frac{\sqrt{a}\delta + \sqrt{a\delta^2 - b\varepsilon_-}}{b}$$
(2.36)

where

$$\left. \begin{array}{l} a = \dfrac{2\mathbf{k}_a D_g (\mathbf{k}_a / 2)}{C_g (\mathbf{k}_a / 2)}, b = \dfrac{4\sqrt{2}\omega_a D_g (\mathbf{k}_a / 2)}{\left\{ C_g (\mathbf{k}_a / 2) \right\}^2} \\[4mm] c = \dfrac{2\sqrt{2}\omega_a}{\mathbf{k}_a C_g (\mathbf{k}_a / 2)} \mu \end{array} \right\} .$$
(2.37)

The above argument ceases to be valid near the zero of $\mu = (\partial \gamma / \partial \Omega)_P$, which is found at the origin $\tilde{\theta}_3 = \Omega = \tilde{\theta}_1 = 0$. This kind of singularity can be treated only by calculating the triple integral that Masuda derived for deep water waves. However, it is not necessary to take into consideration this singularity because contribution from this singularity is canceled out at the point where the resonant four waves have the same wave vectors.

As described above, the derivation for finite-depth gravity waves by extending the computational method of Masuda (1980) uses the identical equations and variables as in Masuda's derivation when the water depth h approaches infinity.

For numerical computations, Hashimoto et al. (1998) used the same resonant interaction symmetries as those used by Komatsu (1993) and by Komatsu and Masuda (1996), i.e.,

$\omega_3 \leq \omega_1 \leq \omega_2 \leq \omega_4$. Compared with the other methods for finite water depths, such as the EXACT-NL method (Hasselmann and Hasselmann, 1981), the Hashimoto method seems to be more accurate than the EXACT-NL method because the results for the latter are unstable even for deep water waves. However, Hashimoto's results still include instability for finite water depths. Komatsu and Masuda (2000) showed that the instabilities for finite water depths originate in the nature of the four wave resonance interactions in finite water depths. The shape of the resonance interaction contour lines becomes flat in finite water depths. A small change in $\tilde{\theta}_1$ causes a large difference in the magnitude of ω_1. Therefore, in order to eliminate instability in the computations, Komatsu and Masuda (2000) changed the sequence of frequencies to $\omega_1 \leq \omega_3 \leq \omega_4 \leq \omega_2$. By applying this modification, the special treatment around the singular points is no longer necessary.

2.7 Conclusion

The present chapter presents a brief overview of previous studies of the computation of nonlinear energy transfer in wave models. The third-generation wave models, which explicitly account for the nonlinear energy transfer for practical wave modeling, became a possibility with the development of the DIA method (Hasselmann et al., 1985). However, drawbacks of the DIA were already identified in the original paper.

Numerous methods have been developed for finding a more accurate and computationally feasible alternative to the DIA method. Komatsu and Masuda (1996) developed the RIAM method, which represents a reduced version of the exact interactions based on the Masuda method (1980). This method gives better accuracy for test spectra and has longer computational time than the DIA method because it processes a thousand of configurations. Komatsu and Masuda (1996) showed that the RIAM method cannot be used as an algorithm for operational wave prediction. Therefore, they developed the SRIAM method, which has a smaller number of resonance configurations of 20.

By using the same independent parameters as in the DIA method, Hashimoto and Kawaguchi (2001) developed alternative DIA methods called the EDIA and MDIA methods. In the EDIA and MDIA methods, it can be shown that by extending the number and definition of representative quadruplets, the performance of the DIA method can be improved. Although

nonlinear energy transfer is accurately computed in the RIAM, SRIAM, and MDIA methods compared with the DIA method, they only apply to deep-water waves. For infinite water depth, the FD-RIAM method developed by Hashimoto et al. (1998) is an accurate method for computing nonlinear energy transfer in infinite-water depth.

The optimum resonant configurations depend on the number of selected configurations and the number of directional and frequency bins constituting the directional spectrum in the model. For practical purposes, therefore, we need to select the values that are applicable to various types of directional spectra.

CHAPTER 3

NUMERICAL STUDY OF EVOLUTION OF A GRAVITY WAVE SPECTRUM IN DEEP WATER

3.1 Introduction

Studies of two-dimensional spectra of ocean waves are very important, not only for practical purposes, such as wave forecasting, but also for clarifying the fundamental processes of wave generation and development. As it is well known, the spectral shape of a fully developed wind–sea spectrum, including the development and frequency downshift, is controlled by nonlinear energy transfer. Numerous studies have been devoted to investigating the importance of nonlinear energy transfer in the frequency domain. In this chapter, the spatial and temporal characteristics of directional spectra are investigated by taking into account only nonlinear energy transfer in deep water under various conditions.

Long-term evolution of a gravity wave spectrum caused by nonlinear energy transfer is investigated by performing three different types of the third-generation wave model, i.e., the WAM, where each type is implemented with the DIA (Hasselmann et al., 1985), RIAM (Komatsu et al., 1993), and SRIAM (Komatsu et al., 1996) methods. We compared the numerical results of these methods for various directional spectra, including the multimodal spectra, to study the characteristics of the directional wave spectrum in space and time caused by nonlinear energy transfer.

3.2 Initial Conditions of Directional Spectrum

In this chapter, the original WAM implemented with the DIA method for computing nonlinear energy transfer and a modified WAM (implemented with the RIAM and SRIAM methods) are performed in deep water under duration-limited conditions for 120 h. The directional wave spectrum represents the spatial distribution of wave energy, not only in the frequency domain but also in the direction domain.

In this chapter, the wave spectrum is defined by the Mitsuyatsu-type for JONSWAP spectrum with the frequency spectrum $S(f)$ given by

$$S(f,\theta) = S(f)G(\theta|f),\tag{3.1}$$

where $S(f, \theta)$ is the directional wave spectrum and $G(\theta|f)$ is the directional spreading function

$$S(f) = \sum_i \alpha_i H_{1/3_i}^2 T_{pi} \left(f/f_{pi}\right)^{-m_i} \exp\left\{-(m_i/n_i)\left(f/f_{pi}\right)^{-n_i}\right\} \gamma_i^{\exp\left\{-\left(f/f_{pi}-1\right)^2/2\sigma^2\right\}},\tag{3.2}$$

where

$$f_p = \left[1 - 0.132(\gamma + 0.2)^{-0.559}\right]/T_{1/3},$$

$$\sigma = \begin{cases} 0.07 & \left(0.7f_p < f < f_p\right) \\ 0.09 & \left(f_p \le f < f_p\right) \end{cases},\tag{3.3}$$

and

$$G(\theta|f) = \sum_i \beta_i \cos^{2S_i}\left\{(\theta - \bar{\theta}_i)/2\right\},\tag{3.4}$$

$$S = \begin{cases} S_{max}\left(f/f_p\right)^5 & \left(f < f_p\right) \\ S_{max}\left(f/f_p\right)^{-2.5} & \left(f \ge f_p\right) \end{cases}\tag{3.5}$$

with f_p being the spectral peak frequency and S_{max} being the spreading parameter. The JONSWAP spectrum is characterized by the peak enhancement factor γ. This factor controls the sharpness of the spectral peak with values ranging from 1 to 10. In this study, we assume $\gamma = 1.0$ for the PM spectrum case and $\gamma = 3.3$ for the JONSWAP spectrum case. Equation (3.2) is the formulation of the JONSWAP spectrum, including the wind speed as a parameter for wave forecasting based on the results of the joint wave observation program in the North Sea by Hasselmann et al. (1973). Equation (3.2) reduces to the formulation for the fully developed wind wave spectrum when $\gamma = 1.0$.

The observations of Mitsuyasu et al. have shown that the peak value S_{max} increases as the parameter representing the state of wind wave grows. According to Goda (2010), Wilson's formula leads to the following values of S_{max} for engineering applications

(i)	Wind waves	$S_{max} = 10,$
(ii)	Swell with short decay distance	$S_{max} = 25,$
(iii)	Swell with long decay distance	$S_{max} = 75.$

In this study, various values (S_{max} = 10–75) are applied to the directional spectra.

For initial conditions, the significant wave height and period are assumed based on the following formula (Goda, 2010), which can be deduced from Wilson's formula for wind wave conditions by neglecting the differences caused by the wind speed:

$$T_{1/3} \approx 3.3 \left(H_{1/3} \right)^{0.63}. \tag{3.6}$$

Figure 3.1 gives the approximate range of the significant height and period of wind waves and swell in Eq. (3.6). The diagram consists of two regions marked as "zone of no waves" and "swell zone," which are divided by a red thick line marked as "wind waves." The line of wind waves shows the relationship between $H_{1/3}$ and $T_{1/3}$ in Eq. (3.6) (Goda, 2010).
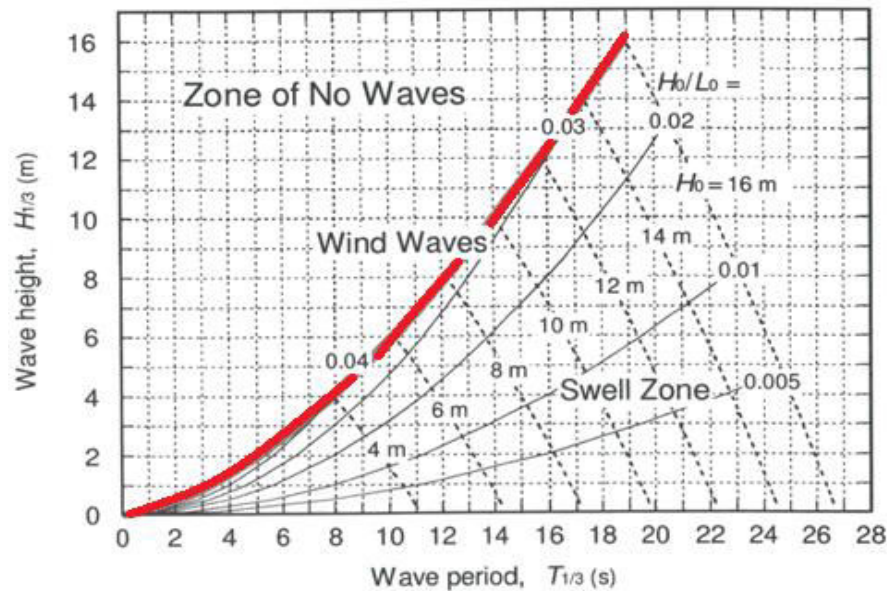
Figure 3.1. Relationship between the significant wave height and period of wind waves and swell (Adapted from Goda, Y. , 2010. Random Seas and Design of Maritime Structures, 3rd Edition, Advanced Series on Ocean Engineering, Vol.33, World Scientific Publishing, 708p).

3.3 Frequency Downshift in Gravity Wave Spectra caused by Nonlinear Energy Transfer
3.3.1 Long-term Evolution of Frequency Spectra

The values of γ = 3.3 and f_p = 0.1 Hz are assumed for the JONSWAP-type spectrum and Mitsuyatsu's directional function, and the directional spreading parameter S_{max} = 15 is an initial condition. Figure 3.2 shows the long-term evolution of the frequency spectra on the left side and

its nonlinear energy transfer spectra on the right side, which was computed by taking into account only the nonlinear energy transfer term (S_{nl}), without the wind input ($S_{in} = 0$) and dissipation ($S_{dis} = 0$). The frequency spectra and the nonlinear energy transfer frequency spectrum are computed in duration-limited conditions for 120 h using the original WAM model implemented with the DIA method, and the modified WAM implemented with the RIAM and SRIAM methods.

The blue line shows the initial spectrum, whereas the red line shows the spectrum after 120 h of simulation. The gray thin lines illustrate the evolution of the spectra at 15, 30, and 45 min, and 1, 2, 6, 12, 24, 48, 72, 96, and 120 h. The horizontal axis represents the frequency f, and the vertical axis shows the normalized energy density E divided by the maximum value of the initial spectrum.

As can be seen in the left column of Fig. 3.2, the peak frequency moves toward the low-frequency side in all cases. The modified WAM model implemented with the RIAM and SRIAM methods show smooth and continuous frequency downshift, whereas the original WAM implemented with the DIA method shows relatively discontinuous frequency downshift in the frequency spectra. The evolution of the spectra in the RIAM method shows narrower shapes than that in the SRIAM and DIA methods. The long-term evolution of each frequency spectra differs in each method. This seems to be caused by nonlinear energy transfer (right column of Fig. 3.2).

The right column of Fig. 3.2 shows the time evolution of the nonlinear energy transfer S_{nl} as a function of the frequency f, where $S_{nl}(f, \theta)$ is integrated with respect to the direction angle θ. The blue line shows the initial frequency distribution of the nonlinear energy transfer spectrum corresponding to the initial directional spectrum, whereas the red line shows the frequency distribution of the nonlinear energy transfer spectrum after 120 h of simulation. The thin lines illustrate the evolution of the nonlinear energy transfer spectrum corresponding to the spectra in the left column. The intensity of the nonlinear energy transfer spectrum gradually decreases with the downshift of the spectral peak. The RIAM and SRIAM methods show almost a similar frequency distribution for the nonlinear energy transfer spectrum. There are two negative extreme values. Whereas the negative extreme values of the nonlinear energy transfer spectrum in the RIAM method are slightly different from those in the SRIAM method, they are very different from those in the DIA method.

The left column of Fig. 3.3 shows the long-term evolution of the frequency spectra computed by taking into account the wind input S_{in} and energy dissipation S_{dis} under the same conditions as those in Fig. 3.2. The RIAM and SRIAM methods show continuous and smooth downshift of the spectral peak, whereas the DIA method shows significantly different results. The spectra computed in the DIA method show an unreasonable result, where the peaks become smaller initially and then increase thereafter. The right column of Fig. 3.3 shows the evolution of the nonlinear energy transfer spectrum corresponding to the spectra in the left column. The intensity of the nonlinear energy transfer spectrum in the RIAM and SRIAM methods gradually decreases with the downshift of the spectral peak and the decrease of wave steepness, while that of the DIA results shows two negative extreme values. Although the distributions of the nonlinear energy transfer spectrum in the RIAM and SRIAM methods seem similar, they are very different from those in the DIA method.
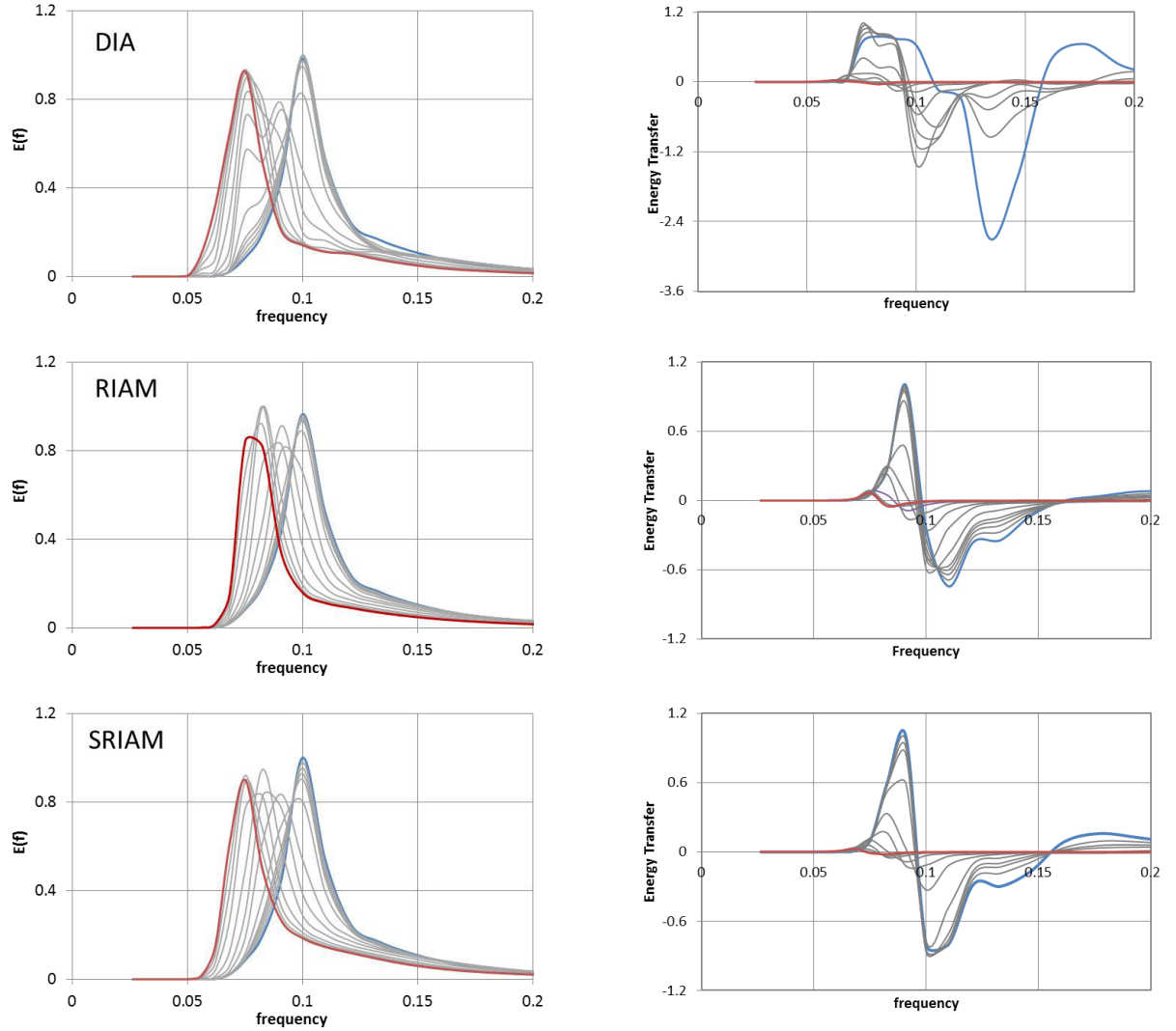
Figure 3.2. Long-term evolution of the frequency spectra (left column) and nonlinear energy transfer spectrum related to the frequency spectra (right column) in the original DIA, RIAM, and RIAM methods.
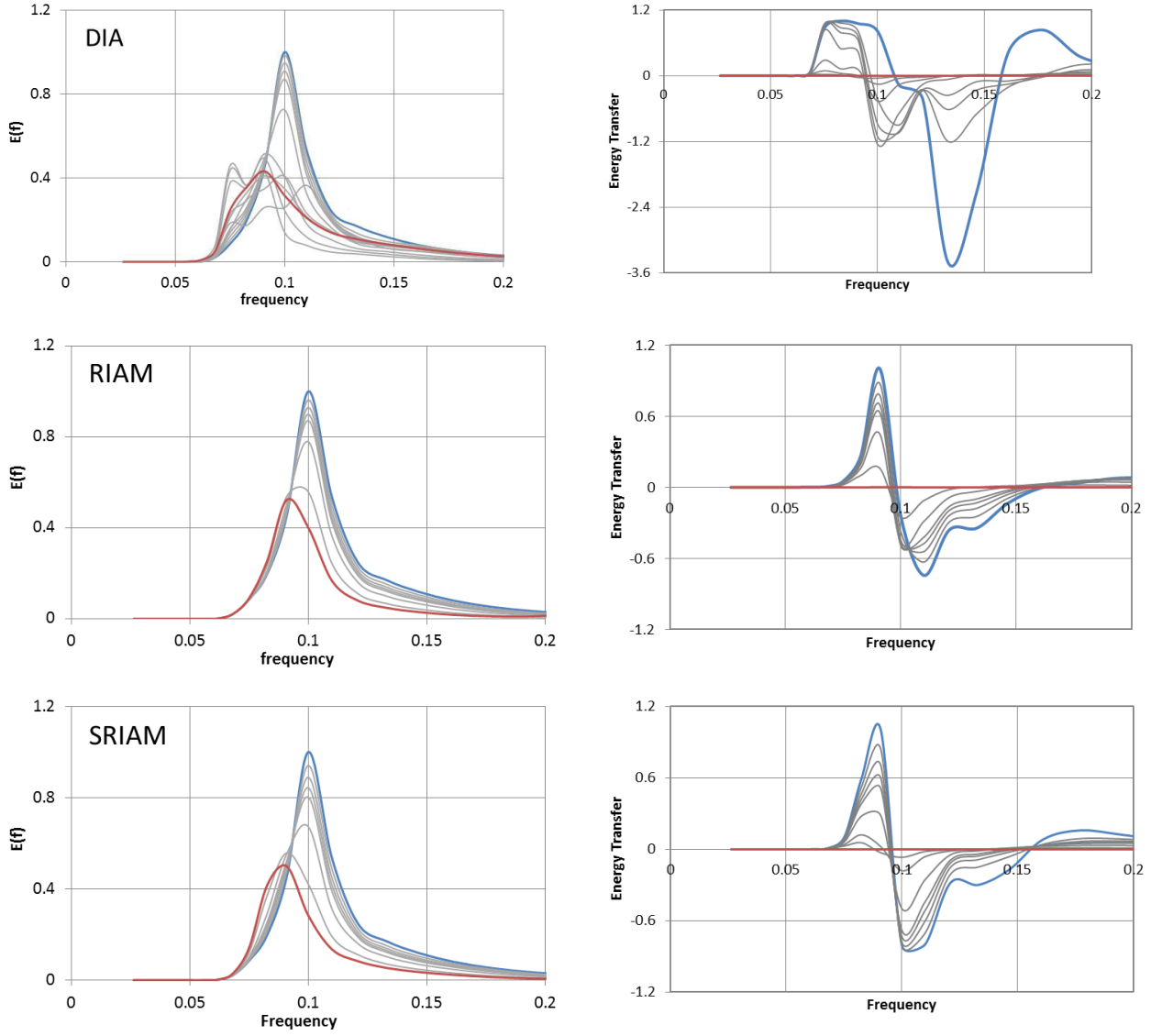
Figure 3.3. Long-term evolution of the frequency spectra (left column) and nonlinear energy transfer spectrum related to the frequency spectra (right column) in the original DIA, RIAM, and RIAM methods (S_{in} and S_{dis} are applied).

Based on these results, the RIAM and SRIAM methods have inherently similar characteristics. Therefore, in the following sections of this chapter, the characteristics of the frequency downshift are discussed on the basis of the numerical results computed using the SRIAM method, a practical computation method for deep water waves.

3.3.2 Relation Between Frequency Downshift and Wave Steepness

Figure 3.4 shows examples for the time evolutions of the frequency spectra, where the JONSWAP spectra and Mitsuyasu-type of directional functions are used for the initial conditions of the directional spectra computed in the SRIAM method. The peak frequencies are assumed to

be the same ($f_p = 0.1$ Hz) for these three methods, while the significant wave heights are different in each method. In Fig. 3.4(a) the maximum wave height is assumed according to Goda's formula (Eq. (3.6)) as the possible maximum significant wave height, i.e., the maximum wave steepness under the condition of $f_p = 0.1$ Hz. The values for wave steepness in Figs. 3.4(a), 3.4(b), and 3.4(c) are 0.031, 0.023, and 0.015, respectively. As can be seen in Fig. 3.4, the intensity of the frequency downshift decreases with the decreasing wave steepness, so does the corresponding nonlinear energy transfer spectrum as shown in Fig. 3.5.
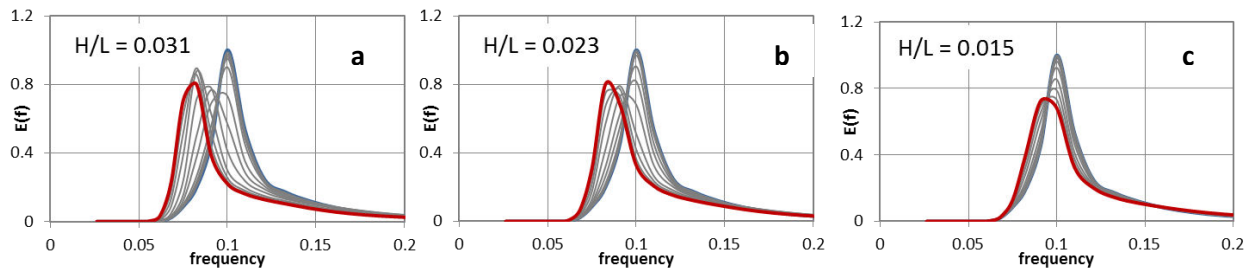
Figure 3.4. Relation between the frequency downshift and wave steepness H/L (f_p = constant) for the time evolution of the frequency spectra (S_{nl} is computed in the SRIAM method).
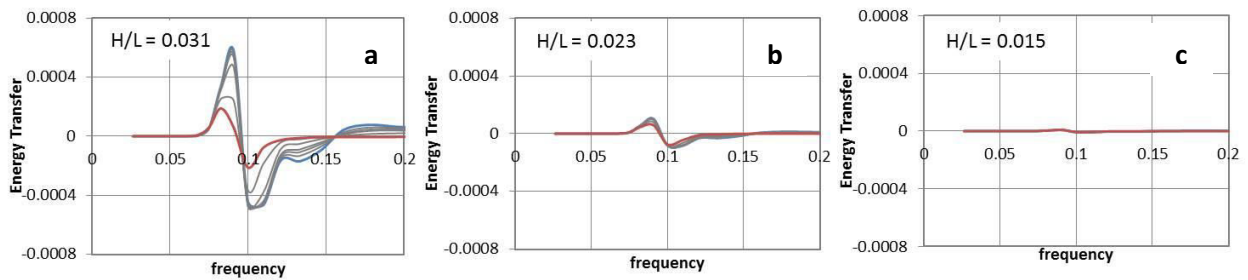
Figure 3.5. The relation between the distribution of nonlinear energy transfer spectrum and wave steepness H/L (f_p = constant) for time evolution of the frequency spectra (S_{nl} is computed in the SRIAM method).

3.3.3 Relation Between Frequency Downshift and Peak Frequency
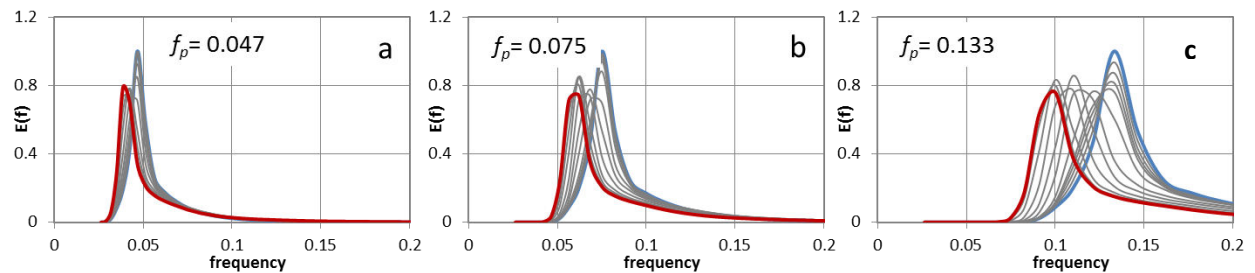
Figure 3.6. Relation between the frequency downshift and peak frequency f_p for the time evolution of the frequency spectra (S_{nl} is computed in the SRIAM method).

Figure 3.6 shows examples for the time evolution of the frequency spectra, where the energy concentration parameters are assumed to be $\gamma = 3.3$ and $S_{max} = 15$, the same in all cases, while the peak frequencies are assumed to be $f_p = 0.047$ Hz in Fig. 3.6(a), 0.075 Hz in Fig. 3.6(b), and 0.1333 Hz in Fig. 3.6(c). In each case, the significant wave periods are determined by Eq. (3.2) as $T_{1/3} = 20.03$ s in Fig. 3.6(a), 12.44 s in Fig. 3.6(b), and 7.02 s in Fig. 3.6(c). Then, the significant wave heights $H_{1/3}$ are determined by Eq. (3.6) as the possible maximum values of wind waves, i.e., the steepest waves in the statistical sense under each wave condition.

As can be seen in Fig. 3.6, the frequency downshift caused by nonlinear energy transfer is most intense in the case when the peak frequencies are at high frequencies, and then decreases with the decrease in f_p (with the increase in $T_{1/3}$) even under the condition of the maximum $H_{1/3}$. This may indicate that there seems to be a maximum limit in the significant wave period. Our numerical experiments indicate that the possible frequency downshift caused by nonlinear energy transfer is up to $T_{1/3} \approx 30$ s approximately at the maximum. Waves with periods longer than $T_{1/3} \approx 30$ s cannot be generated by nonlinear energy transfer under reasonable initial wind wave conditions for $H_{1/3}$ and $T_{1/3}$.

3.3.4 Relation Between Frequency Downshift and Energy Concentration Parameters
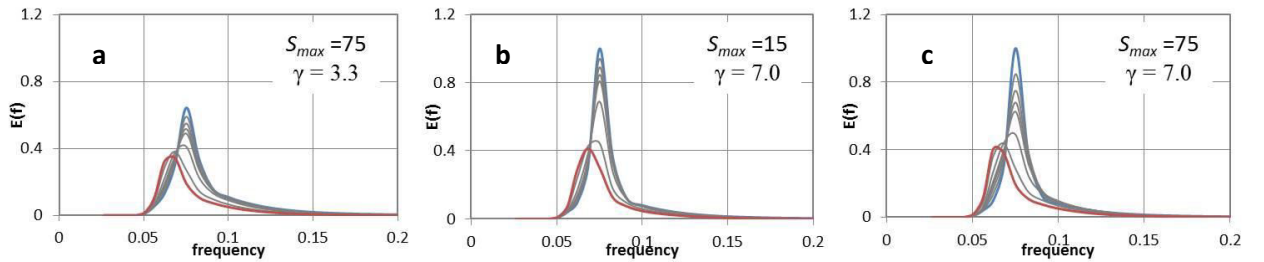
Figure 3.7. Relation between the frequency downshift and energy concentration parameters (S_{max} and γ) for the time evolution of the frequency spectra (S_{nl} is computed in the SRIAM method).

Figure 3.7 shows examples for the evolution of the frequency spectra computed under the same condition of the peak frequency, i.e., $f_p = 0.075$ Hz. The combination of the energy concentration parameters γ and S_{max} are assumed to be different in each case: $\gamma = 3.3$ and $S_{max} = 75$ in Fig. 3.7(a), $\gamma = 7.0$ and $S_{max} = 15$ in Fig. 3.7(b), and $\gamma = 7.0$ and $S_{max} = 75$ in Fig. 3.7(c). The values for the significant wave height $H_{1/3}$ and period $T_{1/3}$ are $H_{1/3} = 8.26$ m and $T_{1/3} = 12.44$ s in Fig. 3.7(a), $H_{1/3} = 8.56$ m and $T_{1/3} = 12.73$ s in Fig. 3.7(b), and $H_{1/3} = 8.56$ m and $T_{1/3} = 12.73$ s in Fig. 3.7(c). In addition, Fig. 3.6(b) and Fig. 3.7(a) are computed with almost the same conditions except for

S_{max}, i.e., $S_{max} = 15$ in Fig. 3.6(b), while $S_{max} = 75$ in Fig. 3.7(a). Comparisons were conducted for Figs. 3.6(b) and 3.7(a), and for Figs. 3.7(b) and 3.7(c). The intensity of frequency downshift seems to increase with the increase in the energy concentration parameters γ and S_{max}.

3.3.5 Characteristics of Frequency Downshift in Bimodal Spectra

The characteristics of nonlinear energy transfer in various bimodal frequency spectra are investigated in this section. Figure 3.8 shows the evolution of the bimodal frequency spectra computed in the SRIAM method, where $f_p = 0.1$ Hz, $\gamma = 3.3$, and $S_{max} = 15$ are assumed in Figs. 3.8(a), 3.8(b), and 3.8(c), while the spectra on the low-frequency side are assumed at $f_p = 0.08$ Hz with $\gamma = 7.0$ and $S_{max} = 75$ in Fig. 3.8(a), $f_p = 0.075$ Hz with $\gamma = 7.0$ and $S_{max} = 75$ in Fig. 3.8(b), and $f_p = 0.07$ Hz with $\gamma = 7.0$ and $S_{max} = 75$ in Fig. 3.8(c). The crossing angle $\Delta\theta$ between the principal wave propagation directions of the two wave groups is assumed to be $\Delta\theta = 0°$ in Figs. 3.8(a), 3.8(b), and 3.8(c), i.e., the ratios between the two peak frequencies are 0.8 in Fig. 3.8(a), 0.75 in Fig. 3.8(b), and 0.7 in Fig. 3.8(c). The computations are performed under duration-limited conditions for 12 h using the WAM implemented in the SRIAM method by taking into account only the nonlinear energy transfer S_{nl}, and without the wind input ($S_{in} = 0$) and dissipation ($S_{dis} = 0$).
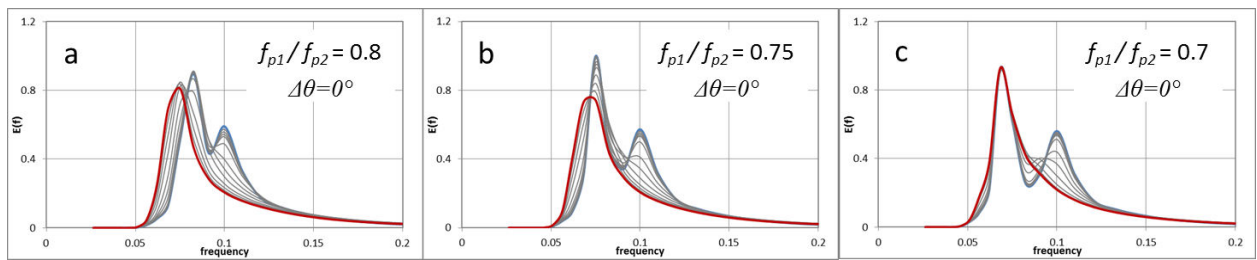
Figure 3.8. Characteristics of the frequency downshift in the bimodal spectra for different values of f_{p1}/f_{p2} (S_{nl} is computed in the SRIAM method).
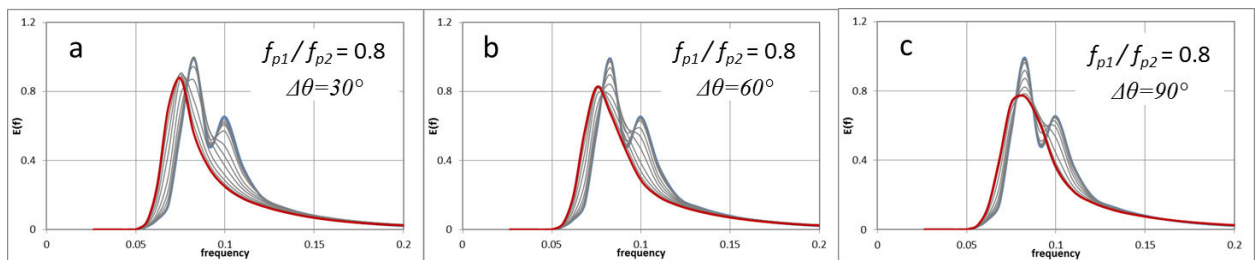
Figure 3.9. Characteristics of the frequency downshift in the bimodal spectra for different values of $\Delta\theta$ (S_{nl} is computed in the SRIAM method).

As can be seen in Fig. 3.8, the energy distributions of the bimodal spectra gradually change to unimodal ones where the peaks at higher frequency gradually disappear because of the influence of the nonlinear energy transfer S_{nl}. In Fig. 3.8(a), where the ratio between the two peak frequencies is relatively large (f_{p1}/f_{p2} = 0.80), the frequency downshift can be seen clearly. Meanwhile, no frequency downshift is observed in Fig. 3.8(c), where f_{p1}/f_{p2} = 0.70. The intensity of the frequency downshift in Fig. 3.8(b) is between those of Figs. 3.8(a) and 3.8(c), i.e., the intensity of the frequency downshift decreases with the decrease in the frequency ratio f_{p1}/f_{p2}. Similar phenomena have been reported in previous studies (e.g., Masuda, 1980 and Komatsu et al., 1996).

Figure 3.9 shows examples for the evolution of the frequency spectra computed under the same condition as that in Fig. 3.8(a) except for the assumption for the crossing angle $\Delta\theta$. The results in Figs. 3.9(a), 3.9(b), and 3.9(c) are computed with $\Delta\theta = 30°, 60°$, and $90°$, respectively. The most intense frequency downshift can be seen in Fig. 3.9(a), where $\Delta\theta = 0°$. As can be seen in Figs. 3.8(a) and 3.9, the intensity of the frequency downshift decreases with increasing $\Delta\theta$. Masson (1993) investigated nonlinear energy transfer for a swell of finite bandwidth and indicated a maximum coupling when the swell direction is about 40° relative to the mean direction of the short waves. The results in Figs. 3.8 and 3.9 seem to differ from that of Masson.

3.4 Directional Characteristics of Nonlinear Energy Transfer
3.4.1 Long-term Evolution of Directional Spectra

The evolution of the directional energy distribution is examined in the WAM by taking into account only the nonlinear term S_{nl} and without wind input and dissipation. For the initial spectrum, we use the same assumption as in Figs. 3.2 and 3.3. Figure 3.10 shows the long-term evolution of the directional energy (left column) and the corresponding nonlinear energy transfer distribution (right column) using the WAM implemented with the DIA, RIAM, and SRIAM methods. The blue line shows the initial spectrum, while the red line shows the spectrum after 12 h of simulation. The figure below shows the time evolution of the directional energy distribution and directional nonlinear energy transfer distribution as a function of the direction θ, where $E(f, \theta)$ and $S_{nl}(f, \theta)$ are integrated with respect to the frequency f.

As can be seen in the Fig. 3.10, after 12 h of simulation, the directional peak energy decreases and the directional energy distribution spreads. Although the changes in $E(\theta)$ seem similar in

three methods, the distribution of the directional energy spectrum in the DIA method shows a broader shape than those in the RIAM and SRIAM methods, and the SRIAM spectrum is a little broader than the RIAM spectrum. The evolution of the directional distribution of nonlinear energy transfer is shown in the right column of Fig. 3.10. The natural shape of the directional distribution is always shown as two positives lobes and one negative lobe. The RIAM and SRIAM methods show the natural shape continuously, while the DIA method shows it differently.
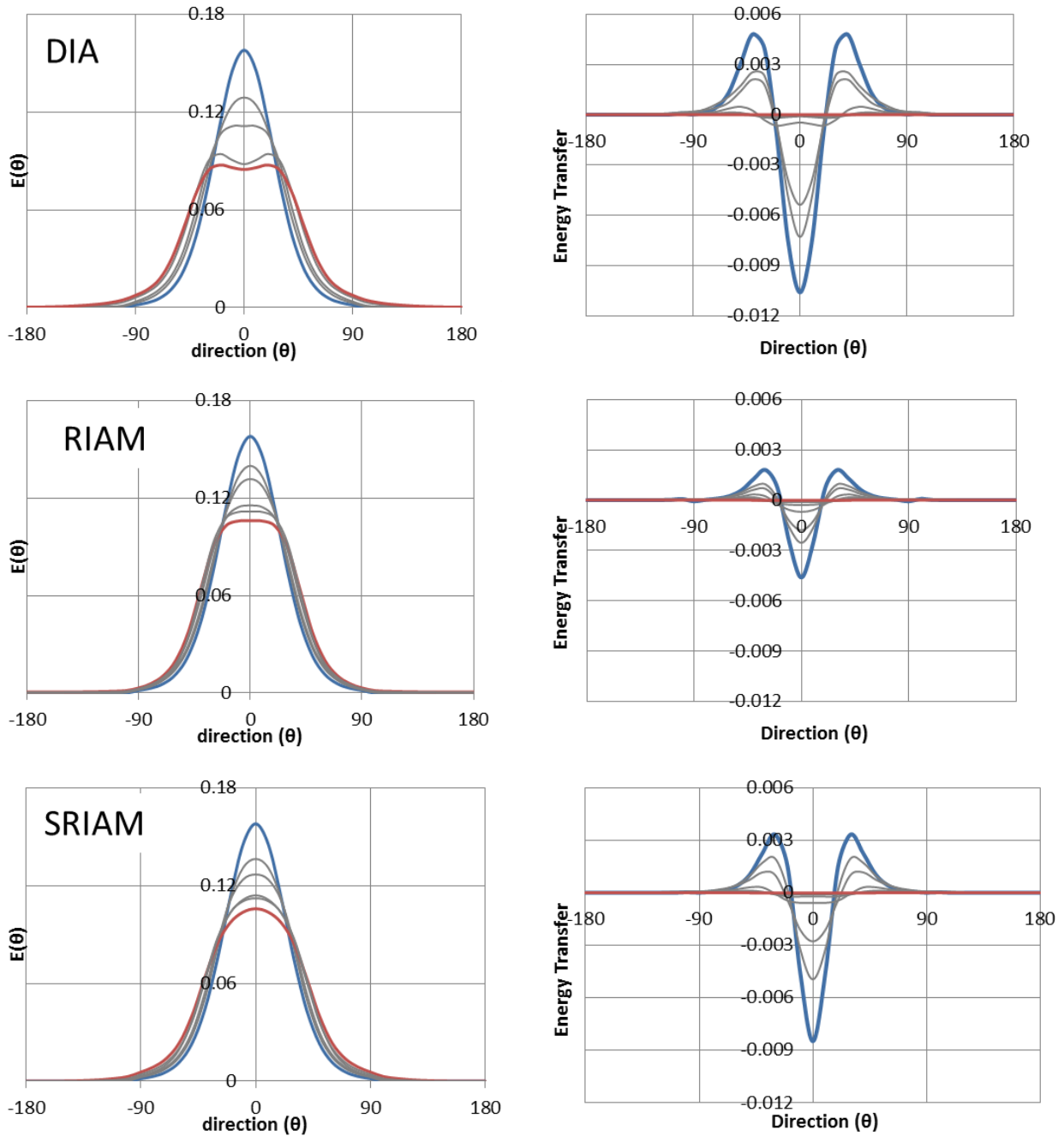
Figure 3.10. Long-term evolution of the directional spectra (left column) and distribution of nonlinear energy transfer spectrum corresponding to the directional spectra (right column) in the DIA, RIAM, and RIAM methods.
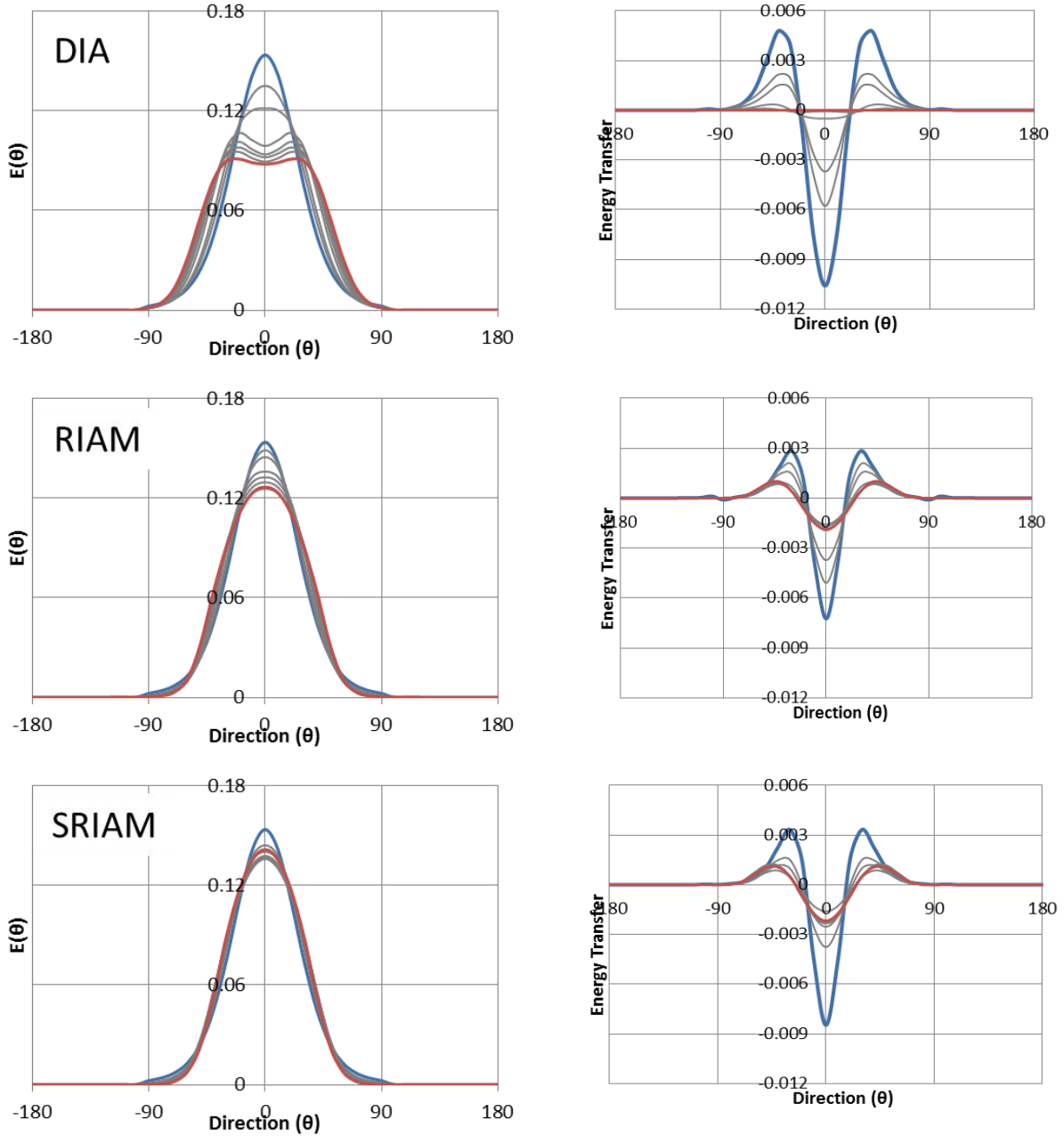
Figure 3.11. Long-term evolution of the directional spectra (left column) and distribution of nonlinear energy transfer spectrum corresponding to the directional spectra (right methods) in the DIA, RIAM, and RIAM methods (S_{in} and S_{dis} are applied).

Figure 3.11 shows the long-term evolution of the directional energy distribution (left column) and the corresponding directional nonlinear energy transfer distributions (right column) by taking into account wind input and dissipation term. After 12 h of simulation, the peak energy in each method decreases. However, the spreading distribution of $E(\theta)$ in each method is different. The shape of the directional energy distribution in the RIAM and SRIAM methods is narrower than the broad shape in the DIA method. Although the shape of the directional spectrum in the DIA

method different from that in the RIAM and SRIAM methods, the corresponding nonlinear energy transfer distribution continuously shows the natural shape of nonlinear distributions.

3.4.2 Directional Distributions for Various Energy Concentration Parameters
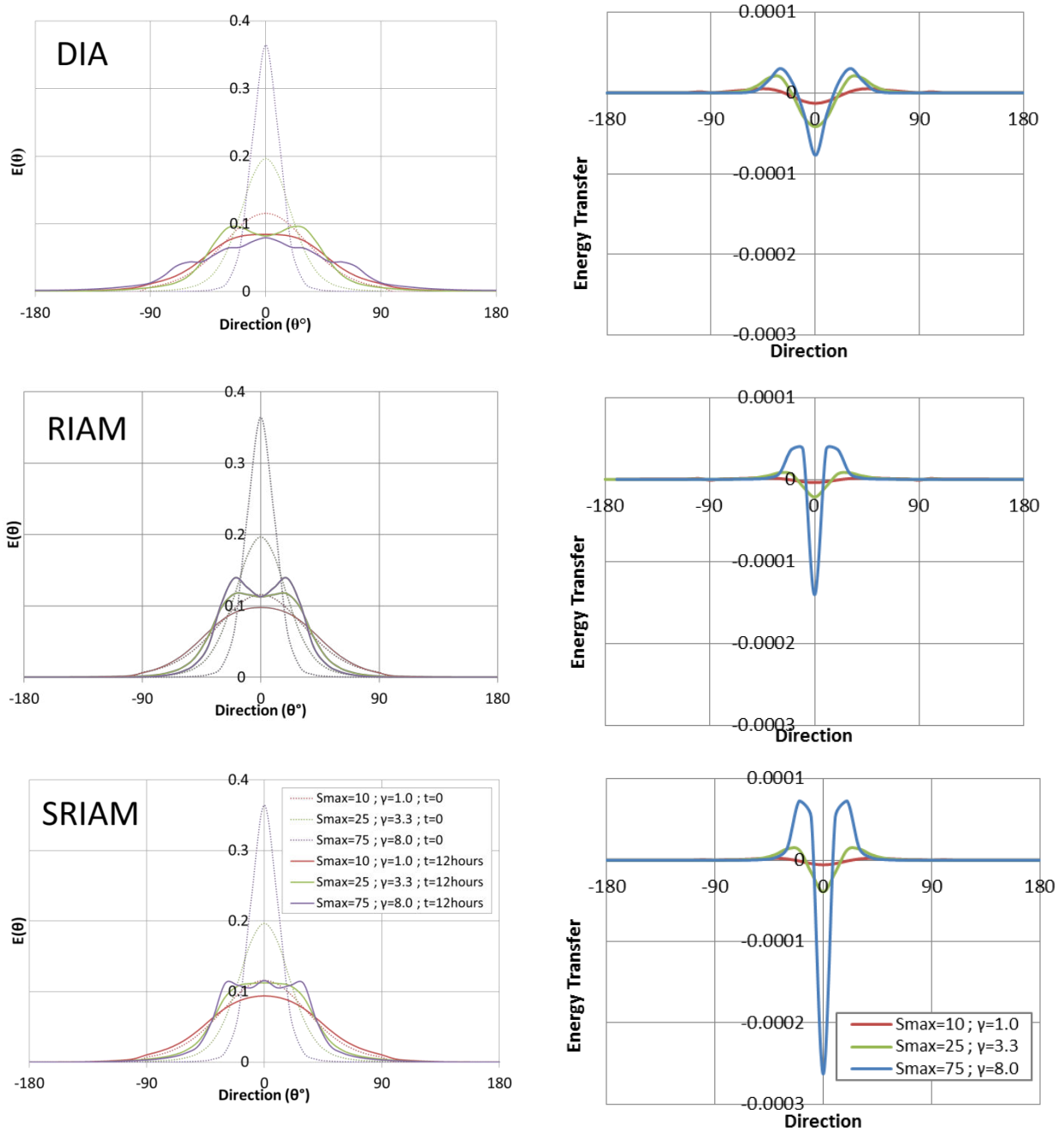
Figure. 3.12. Directional energy distribution and directional nonlinear energy transfer spectrum for various values of the energy concentration parameters γ and S_{max} computed using the WAM implemented in the DIA, RIAM, and SRIAM methods.

In order to clarify the changes in the characteristics of the directional distribution caused by nonlinear energy transfer, numerical simulations are performed for various energy concentration parameters S_{max} and γ. The left column of Fig. 3.12 shows examples for the directional energy distributions computed with various values of the energy concentration parameters S_{max} and γ listed in Table 2.1. The dash lines show the initial value of the directional energy distribution $E(\theta)$, while the solid lines show the result after 12 h of simulation. As can be seen in the left column of Fig. 3.12, after 12 h, the directional peak energy decreases and the directional energy distribution spreads in three methods. Although the changes in $E(\theta)$ are similar in three methods, the DIA result is more diffusive than those of the other methods. The SRIAM result is less diffusive than the RIAM result.

The right column of Fig. 3.12 shows the directional energy distribution of the nonlinear energy transfer spectrum computed for various energy concentration parameters. As can be seen in the right column of Fig. 3.12, the directional distributions of the nonlinear energy transfer always show a pattern of two positive lobes and one negative lobe. The magnitude of the peak absolute value for the directional distribution increases as the energy concentration S_{max} increases in three methods. A comparison of the three methods shows that the magnitude of nonlinear energy transfer is in the order of SRIAM >RIAM > DIA for large energy concentration parameter S_{max}. However, the magnitude of nonlinear energy transfer in the DIA is larger than those in the other methods for small energy concentration parameter S_{max}. These characteristics of the DIA, RIAM, and SRIAM methods seem to be slightly different as can be seen in Fig. 3.12.

Furthermore, in the next subsection, the characteristics of the nonlinear energy transfer spectrum in the direction domain are investigated for various directional spectra based on numerical results computed in the SRIAM method, since the latter seems to be superior in efficiency and accuracy.

3.4.3 Directional Energy Distributions for Various Wave Steepness Values

Figure 3.13 shows examples for the time evolution of the directional energy distributions, where the JONSWAP spectra and Mitsuyasu-type of directional functions are used as the initial conditions of the directional spectra computed in the SRIAM method. In each panel of Fig. 3.13, the peak frequencies are assumed at $f_p = 0.1$ Hz, while the significant wave heights are different. The values of the wave steepness in Figs. 3.13(a), 3.13(b), and 3.13(c) are 0.031, 0.023, and

0.015, respectively. As can be seen in these figures, the peak energy increases as the wave steepness decreases whereas the spreading is more diffusive for higher wave steepness values.
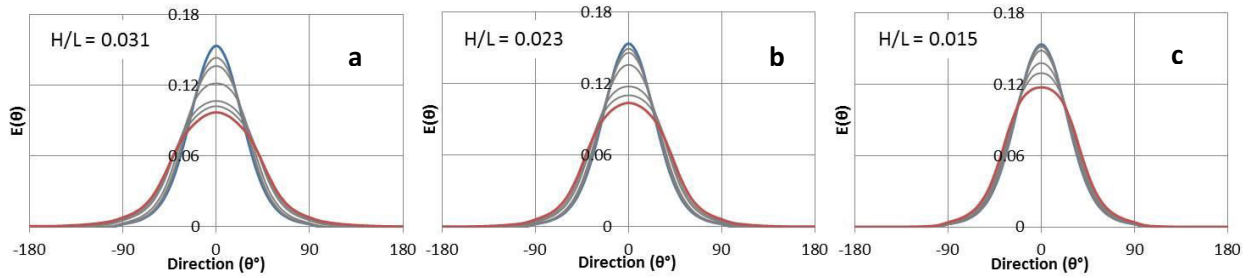
Figure 3.13. Relation between the directional energy distribution and wave steepness H/L (f_p = constant) for the time evolution of the directional spectra (S_{nl} is computed in the SRIAM method).

3.4.4 Directional Energy Distributions for Various Peak Frequencies
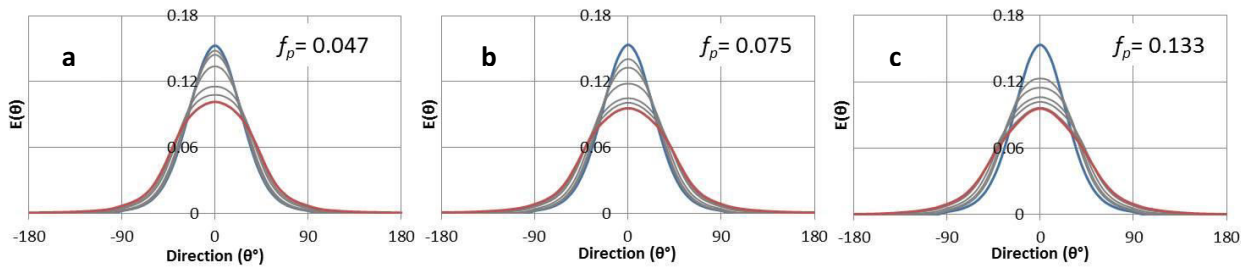
Figure 3.14. Relation between the directional energy distributions and peak frequency f_p for the time evolution of the directional spectra (S_{nl} is computed in the SRIAM method).

Figure 3.14 shows examples for the time evolution of the directional energy distribution for various peak frequencies. We set the peak frequencies for Figs. 3.14(a), 3.14(b), and 3.14(c) to 0.047, 0.075, and 0.133, respectively. As can be seen in Fig. 3.14, the peak energy for higher peak frequency decreases faster. The directional spreading is also more diffusive when the peak frequency is higher.

3.4.5 Bimodal Directional Spectra for Various Crossing Angles

Figure 3.15(a-1) shows the bimodal directional spectrum, where the peak frequencies are at f_p = 0.13 Hz and f_p = 0.1 Hz and the crossing angle between the propagation directions is 0°. This bimodal spectrum is used as the initial condition for the duration-limited condition. Figure 3.15(a-2) shows the temporal change in the directional spectrum after 12 h. As can be seen in these figures, the energy distribution gradually changes to a unimodal spectrum. The high-frequency peak disappears and the directional spectrum broadens as shown in Fig. 3.15(a-2).
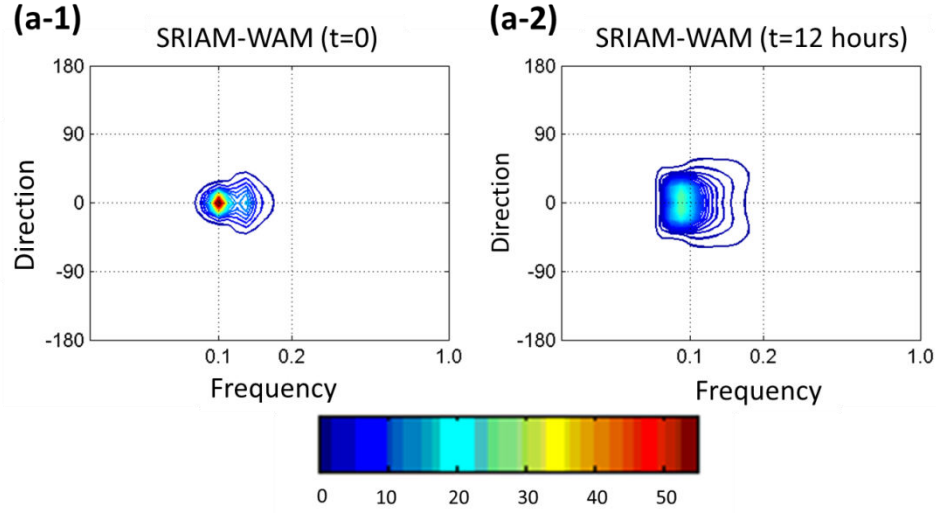
Figure 3.15. Directional spectra of the bimodal spectrum for the crossing angle $\Delta\theta = 0°$ at $t = 0$ (a-1) and $t =12$ h (a-2).
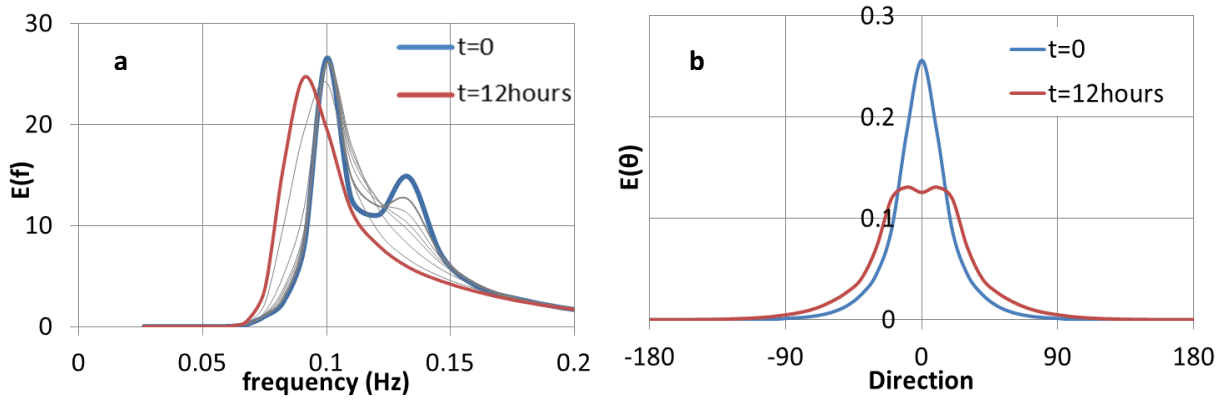
Figure 3.16. Temporal change in the (a) frequency spectra corresponding to the directional spectra in Fig. 3.15 and (b) directional functions (blue line is the initial condition).

Figures 3.16(a) and 3.16(b) show the frequency spectrum and the integrated directional function with respect to frequency f, respectively. The blue line shows the initial bimodal spectrum, where the energy concentration parameters are $\gamma = 3.3$ and $S_{max} = 15$ for the higher peak frequency spectrum, and $\gamma = 7.0$ and $S_{max} = 75$ for the lower peak frequency one. The red line shows the results after 12 hours of simulation. The shape of the spectrum changes into unimodal one with frequency downshift. While, the shape of the directional function changes to wider distribution.

Figures 3.17 and 3.18 show the results for the same parameters used in Figs. 3.15 and 3.16, respectively, except for a crossing angle of 30° between the two wave groups; Figs. 3.19 and 3.20 show the results for a crossing angle of 90° between the two wave groups. As can be seen in Figs. 3.18(a) and 3.20, after 12 h of simulation, both frequency spectra change to unimodal ones.

45

Although the frequency spectrum in Fig. 3.18(a) shows comparably large frequency downshift compared with Fig. 3.16(a), Fig. 3.20(a) does not show clear frequency downshift. Moreover, the directional function in Fig. 3.20(b) still shows clear bimodal peaks in directional energy diffusion even after 12 h. The differences seem to arise from the difference in the nonlinear energy transfer intensity, which depends on the crossing angle between the two wave groups.
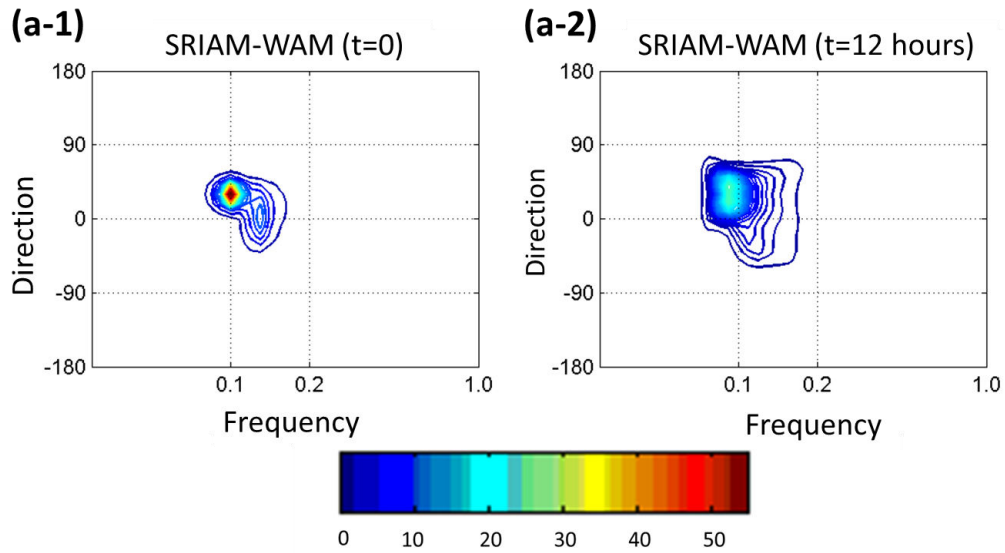
Fig 3.17. Directional spectra of the bimodal spectrum for the crossing angle $\Delta\theta = 30°$ at $t = 0$ (a-1) and $t = 12$ h (a-2).
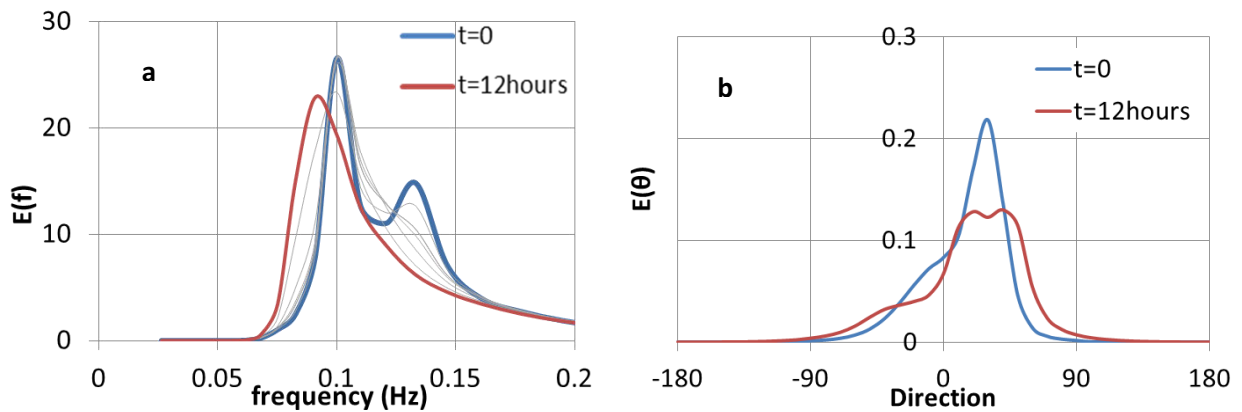
Figure 3.18. Temporal change in the (a) frequency spectra corresponding to the directional spectra in Fig. 3.17 and (b) directional functions (blue line is the initial condition).
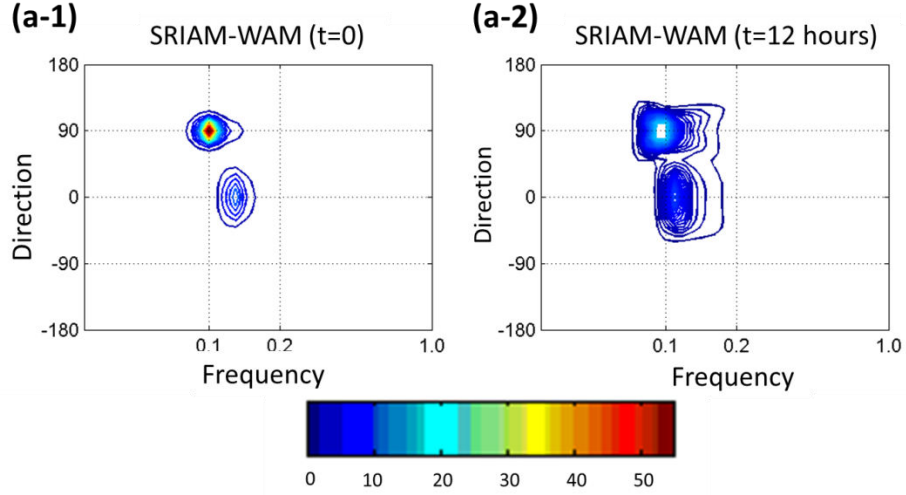
Figure 3.19. Directional spectra of the bimodal spectrum for the crossing angle $\Delta\theta = 90°$ at $t = 0$ (a-1) and $t = 12$ h (a-2).
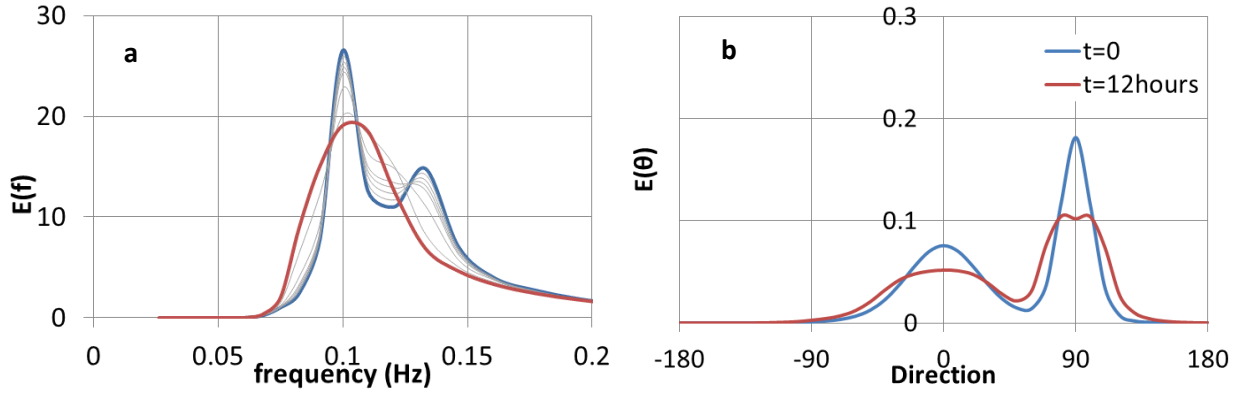
Figure 3.20. Temporal change in the (a) frequency spectra corresponding to the directional spectra in Fig. 3.19 and (b) directional functions (blue line is the initial condition).

Figures 3.21(a), 3.21(b), and 3.21(c) show the directional distributions of the integrated nonlinear energy transfer with respect to the frequency f corresponding to Figs 3.15, 3.17, and 3.19, respectively. The blue lines show the results at $t = 0$, while the red lines show the ones at $t = 12$ h. Figure 3.21(a) shows the symmetric distribution with two positive lobes and one negative lobe, which gradually reduces the nonlinear energy transfer intensity over time.

Figures 3.21(b) and 3.21(c) show the asymmetric distribution. Compared with Figs. 3.21(a) and 3.21(b), Figs. 3.21(c) seems to have different characteristics in that the directional distributions of the negative and positive lobes around the two peak frequencies in are rather independent (a weak interaction) of each other. This may lead to the temporal change in the directional spectra shown in Fig. 3.19.

47
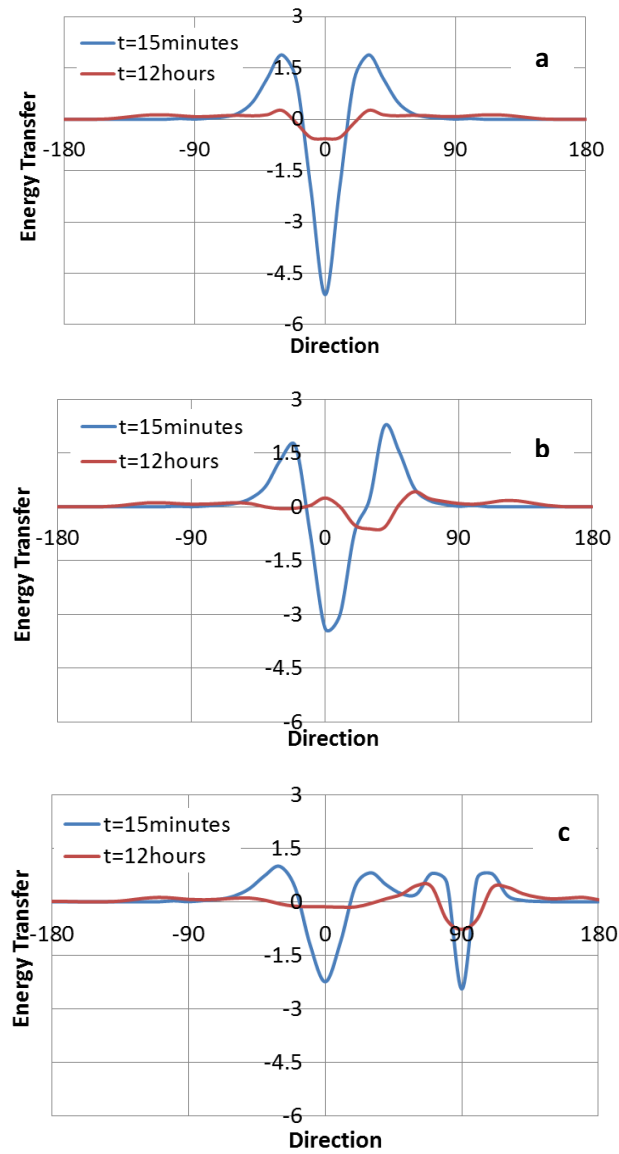
Figure. 3.21. Directional distributions for the nonlinear energy transfer spectrum of the bimodal spectra at a crossing angle of (a) 0˚, (b) 30˚, and (c) 90˚.

3.5 Conclusion

The characteristics of the evolution of the gravity wave spectra caused by nonlinear energy transfer are evaluated in the frequency and direction domains. Numerical simulations are performed using the WAM implemented with the DIA, RIAM, and SRIAM methods in deep water under duration-limited conditions for various initial conditions of the directional spectra and various energy distributions in frequency and direction.

As a result, interesting features of the relation between the frequency downshift and the energy concentration parameters of the directional spectra are clarified. Particularly, the intensity of the

frequency downshift caused by nonlinear energy transfer increases with the increasing energy concentration in frequency and direction.

The characteristics of the frequency downshift and of the directional distribution of the bimodal spectra are also discussed. An interesting characteristic influenced by the crossing angle $\Delta\theta$ between two wave groups in the bimodal spectrum is observed, i.e., a large coupling between the two wave groups can be seen when the two peak frequencies in the bimodal spectrum are relatively narrow in direction.

CHAPTER 4

NUMERICAL STUDY ON FREQUENCY DOWNSHIFT GRAVITY WAVE SPECTRA IN FINITE-WATER DEPTHS

4.1 Introduction

The water depth significantly affects the processes of wave development and wave generation and increases the complexity of wave models (Young and Verhagen, 1996a, 1996b). The spectral shape and magnitude of nonlinear energy transfer also are changed in finite water depths, because nonlinear energy transfer is very sensitive to both the spectrum shape and the water depth.

Computations of nonlinear energy transfer in finite water depths are more complex and more time consuming than computations in deep water. Although the RIAM and SRIAM methods compute nonlinear energy transfer much better than the DIA method in terms of accuracy, they can only be applied to deep water waves. In the RIAM method, the values of the resonant wave vectors for deep-water waves are simply replaced by those of the nearest wave number grid points (Komatsu and Masuda, 1996). However, this replacement does not apply to finite-depth water computations, where interpolated values of the surrounding four wave numbers are needed (Komatsu and Masuda, 2000). The nonlinear energy transfer computations in the WAM and the SWAN model could not capture the frequency downshifts and spectral changes that occur as the water depth decreases (Hashimoto et al., 2002). Currently, there is no computation method that can accurately and efficiently calculate nonlinear energy transfer in finite water depths.

Hashimoto et al. (1998) developed a computational method called the FD-RIAM method for nonlinear energy transfer in finite-depth gravity waves by extending the theories of Masuda (1980) and Komatsu et al. (1993). The method was applied to common wave spectra in finite-water depths. Some characteristics of nonlinear energy transfer in infinite water depths were clarified. In this chapter, we investigate in more detail the characteristics of nonlinear energy transfer in deep- and finite-water depths using the FD-RIAM methods for various directional wave spectra in different water depths.

4.2 Investigation of Frequency Downshift in Finite-Water Depths Using the FD-RIAM Method

As mentioned in Chapter 2, the FD-RIAM method is expressed as

$$\frac{\partial \Phi(\omega_4, \theta_4)}{\partial t} = \frac{2\omega_4 k_4}{C_g(k_4)} \int_0^\pi d\tilde{\theta}_3 \int_0^\infty d\Omega \int_0^\pi d\tilde{\theta}_1 \times \sum_\pm \sum_\pm \sum_\pm \left\{ \frac{k_1 k_3}{C_g(k_1) C_g(k_3)} \frac{G}{S} \right\},$$
$$\times \left\{ n_1 n_2 (n_3 + n_4) - n_3 n_4 (n_1 + n_2) \right\}$$

(4.1)

where $\partial \Phi(\omega, \theta)/\partial t$ is the energy density of a two-dimensional wave spectrum, ω is the angular frequency, k is the wave vector, G is the coupling coefficient, $\tilde{\theta}_1 = \theta_1 - \theta_a$, $\tilde{\theta}_2 = \theta_2 - \theta_a$, $\tilde{\theta}_3 = \theta_3 - \theta_4$, $\Omega = \ln \omega_3$, and the denominator S, arising from $\delta(\omega_1 + \omega_2 - \omega_3 - \omega_4)$, is given by

$$S = \left| 1 + \frac{C_g(k_2)}{C_g(k_1)} \left\{ \frac{k_1 - k_a \cos(\theta_1 - \theta_a)}{k_2} \right\} \right|.$$

(4.2)

We assumed that the directional spectrum $S(f, \theta)$ is a product of the JONSWAP-type frequency spectrum and the Mitsuyatsu-type directional function. The nonlinear energy transfer spectrum is computed under the conditions of $k_p h$ = 8.0, 1.0, 0.8, 0.65, and 0.6, where k_p is the wave number corresponding to the peak frequency of the power spectrum. In the following section, the characteristics of nonlinear energy transfer are examined in one dimension in terms of the function $T_1(\omega)$ defined by

$$T_1(\omega) = \int \frac{\partial \Phi(\omega, \theta)}{\partial t} d\theta.$$

(4.3)

Figures 4.1–4.3 show the one-dimensional nonlinear energy transfer functions $S_{nl}(f)$ as a function of the frequency f, obtained by integrating $S_{nl}(f, \theta)$ with respect to the direction angle θ. Figures 4.1 and 4.2 are computed with γ = 1.0 for a PM-type spectrum. Figures 4.1(a) and 4.1(b) show the directional function as a function of frequency f for S_{max} = 2.0, and Fig. 4.2 shows the directional energy concentration for S_{max} = 10. Meanwhile, Figs. 4.3(a) and 4.3(b) are computed with γ = 3.3 for a JONSWAP-type spectrum with the directional energy concentration S_{max} = 10. The horizontal axis is the ration of the frequency divided and the peak frequency f/f_p, and the vertical axis shows the nonlinear energy transfer spectrum normalized by its maximum value.

Figures 4.1(a), 4.2(a), and 4.3(a) show the $S_{nl}(f)$ computed under the conditions of $k_p h$ = 8.0, 1.0, and 0.8, respectively, and Figs. 4.1(b), 4.2(b), and 4.3(b) are the ones computed under the

51

conditions of k_ph = 0.8, 0.65, and 0.6, respectively. It should be noted that the $S_{nl}(f)$ computed with k_ph = 0.8 is shown in Figs. 4.3(a) and 4.1(b) for convenience of presentation. The absolute values of $S_{nl}(f)$ increase with decreasing k_ph, and the value of $S_{nl}(f)$ for k_ph = 8.0 is very different from that for k_ph =0.6 in all cases. Therefore, it seems inconvenient to show all the results in a single plot. Instead, these results are separated into two plots, and the value for k_ph =8.0 is shown in both panels as a reference.

The distributions of the nonlinear energy transfer spectrum $S_{nl}(f)$ are very different for the cases under consideration, as shown in the figures above, depending on the shape of the directional spectrum and the magnitude of the relative water depth k_ph. As can be seen in Figs. 4.1 and 4.2, for the case of the PM spectrum, the nonlinear energy transfer spectrum for k_ph = 8.0 shows the maximum value around the peak frequency f_p and the minimum value around $1.5f_p$. When k_ph decreases, the maximum and minimum values of the nonlinear energy transfer spectrum move to the low frequency end and their absolute values are increased. For the case of the JONSWAP spectrum, as can be seen in Fig. 4.3, the results are different from those of the PM spectrum in that the nonlinear energy transfer spectrum for k_ph = 8.0 shows the maximum value around the peak frequency $0.95f_p$ and the minimum value around $1.1f_p$. Their magnitudes are also increased as k_ph decreases. However, there seem to be common features in that the intensity of the nonlinear energy transfer spectrum $S_{nl}(f)$ increases with decreasing relative water depth k_ph and that the positive peak of $S_{nl}(f)$ moves toward the low frequency end as k_ph decreases.
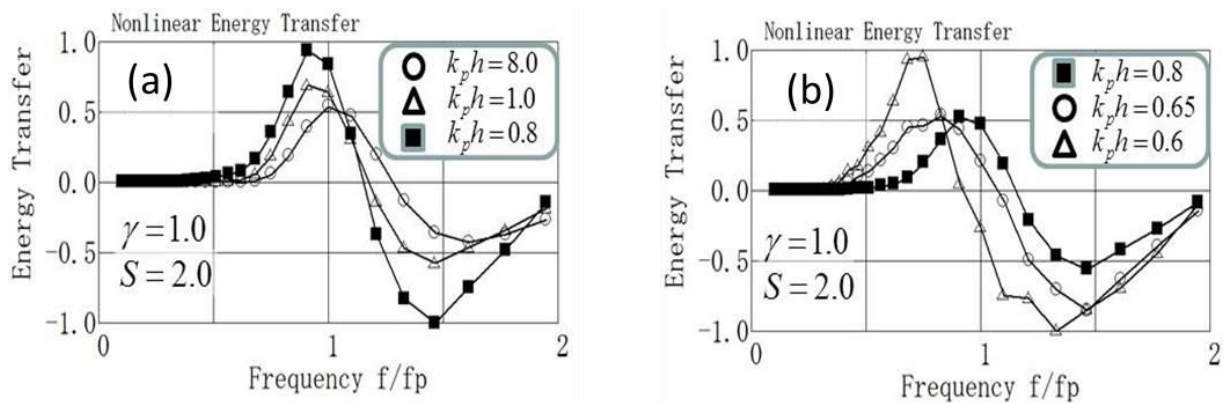
Figure 4.1. One-dimensional nonlinear energy transfer functions for the PM spectrum for S_{max} = 2.0, and (a) k_ph = 8.0, 1.0, 0.8 and (b) k_ph = 0.8, 0.65, 0.6.
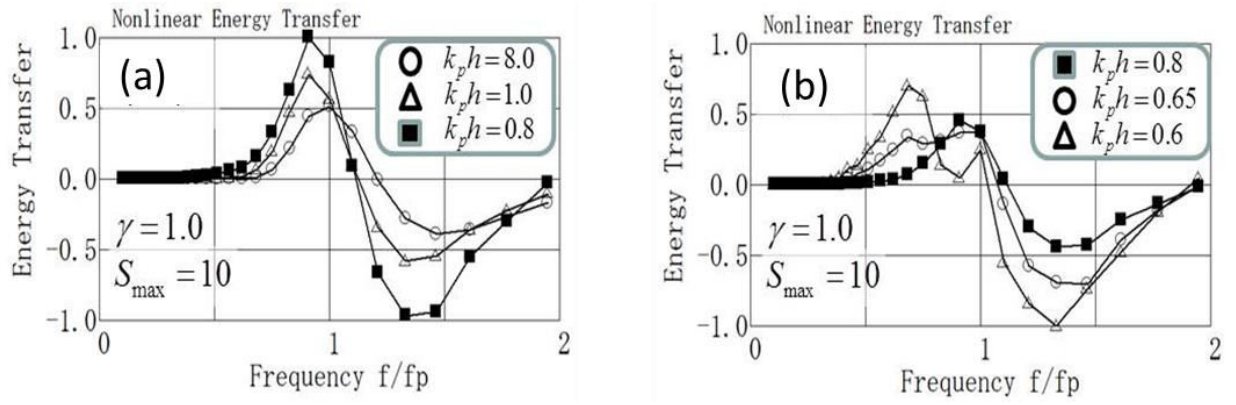
Figure 4.2. One-dimensional nonlinear energy transfer functions for the PM spectrum for $S_{max} = 10$, and (a) $k_p h = 8.0$, 1.0, 0.8 and (b) $k_p h = 0.8, 0.65, 0.6$.
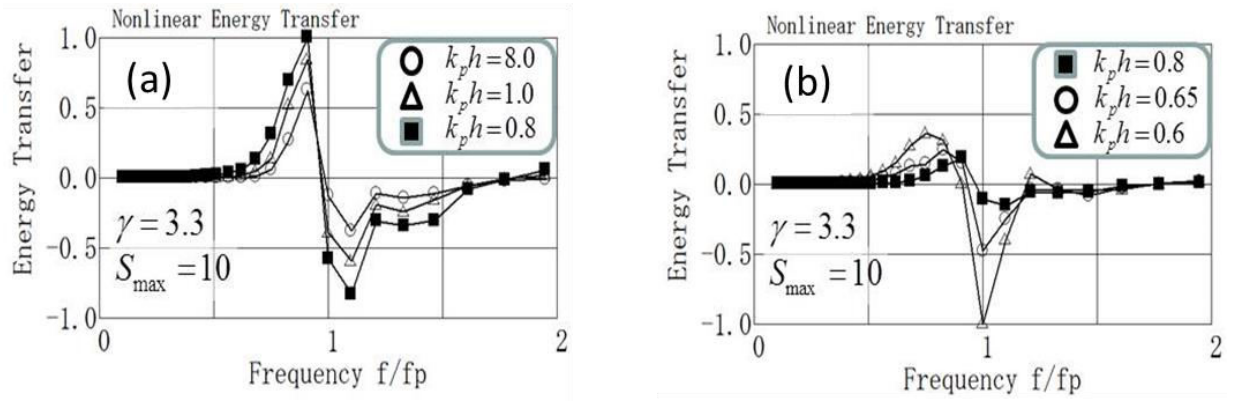
Figure 4.3. One-dimensional nonlinear energy transfer functions for the JONSWAP spectrum for $S_{max} = 10$, and (a) $k_p h = 8.0$, 1.0, 0.8 and (b) $k_p h = 0.8, 0.65, 0.6$.

4.3 Enhancement Factor

In the third-generation wave models the enhancement factor R is introduced to convert the nonlinear energy transfer spectrum in deep water to represent that in finite water depths, and thus making the computations of the nonlinear energy transfer simpler. The enhancement factor R is defined by

$$S_{nl}(\text{finite depth}) = R(\bar{k}h)S_{nl}(\text{infinite depth}), \tag{4.4}$$

where $\bar{k}$ is the mean wave number and S_{nl} (infinite depth) is the nonlinear energy transfer spectrum calculated at kh for a specified directional spectrum.

53

Hasselmann and Hasselmann (1981, 1985) obtained the enhancement factor R in the DIA method using numerical computations by assuming the Mitsuyasu–Hasselmann-type directional spreading function, which can be expressed as

$$R(x) = 1 + \frac{5.5}{x}\left(1 - \frac{5x}{6}\right)\exp\left(-\frac{5x}{4}\right), \quad \text{where} \quad x = (3/4)\bar{k}h. \tag{4.5}$$

The enhancement factor R is a very useful way to make the computations of nonlinear energy transfer in finite water depth faster. This enhancement factor is used in the SWAN model (Booij et al, 1999).

In this study, the differences in the characteristics of nonlinear energy transfer and frequency downshifts in deep and finite water waves are investigated. We apply the same types of directional spectra used for deep water waves by assuming that the directional spectrum $S(f,\theta)$ is a product of the JONSWAP-type frequency spectrum $S(f)$ and the Mitsuyatsu-type directional function $G(\theta|f)$ even though the Texel–Marsen–Arsloe spectrum (Bouws, 1985) seems more suitable for shallow water waves (Tsagareli et al., 2005).

We computed the enhancement factors R for various directional spectra in several water depths. The enhancement factor R in Fig. 4.4 is determined by the ratio of the maximum of nonlinear energy transfer for finite-depth waves and that for deep water waves computed in the FDRIAM method. The marks ■, ○, and △, in Fig. 4.4 show the enhancement factor R for directional spectra with γ = 1.0, 3.3, and 7.0, respectively. As a reference, the enhancement factor R adopted in the WAM is shown as the solid line in Fig. 4.4(a).

The results shown in the Fig. 4.4(a)–4.4(c) are computed for the directional spectra with the directional energy concentration parameter S = 2, 10, and 25, respectively. As can be seen in Fig 4.4, the directional distributions of the directional spectra in Fig. 4.4(b) are wider than those in Fig. 4.4(c). It is clearly shown that the characteristics of the enhancement factor R depend on the energy distribution of the directional spectra. The enhancement factor R, however, shows better agreement with those computed in the FD-RIAM method for smaller S_{max} and γ. Otherwise, R shows better agreement for broader directional spectra in frequency and direction, but not for narrow directional spectra. It should be noted that R is not a monotonic function for narrow directional spectra.
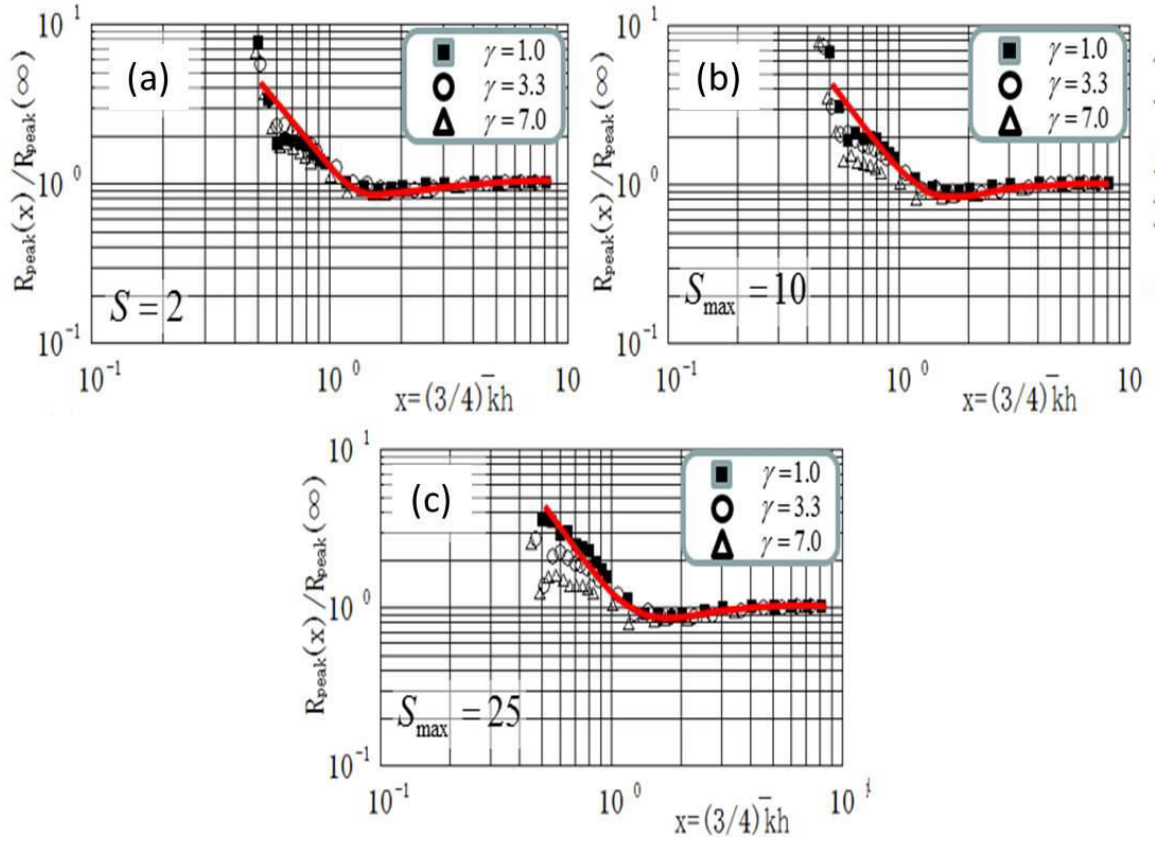
Figure 4.4. Enhancement factor for various directional spectra in several water depths. ($x = (3/4)kh$ is the dimensionless depth)

However, the downshift factor seems to be more important than the enhancement factor because the latter works only for enhancement of the energy distribution but not for the frequency downshift. The downshift factor is defined by the ratio of the frequency of maximum transfer for finite-depth waves and that for deep water waves computed in the FD-RIAM method.

As can be seen in Fig. 4.5, the frequency downshift factors for broad spectra with $\gamma = 1.0$ gradually decrease and return to around the initial values as the relative water depth x decreases, while those of narrow spectra with $\gamma = 3.3$ and 7.0 decrease sharply as the relative water depth x decreases. In other words, although the behavior of the frequency downshift factors for broad spectra shows characteristics similar to those for narrow spectra, the onset of their decrease is at water depths deeper than that for narrow spectra. In very shallow water depths, the downshift factors for broad spectra decrease sharply to very small values. This sudden change might be caused by an applicable limit of nonlinear energy transfer in the Boltzmann Integral.
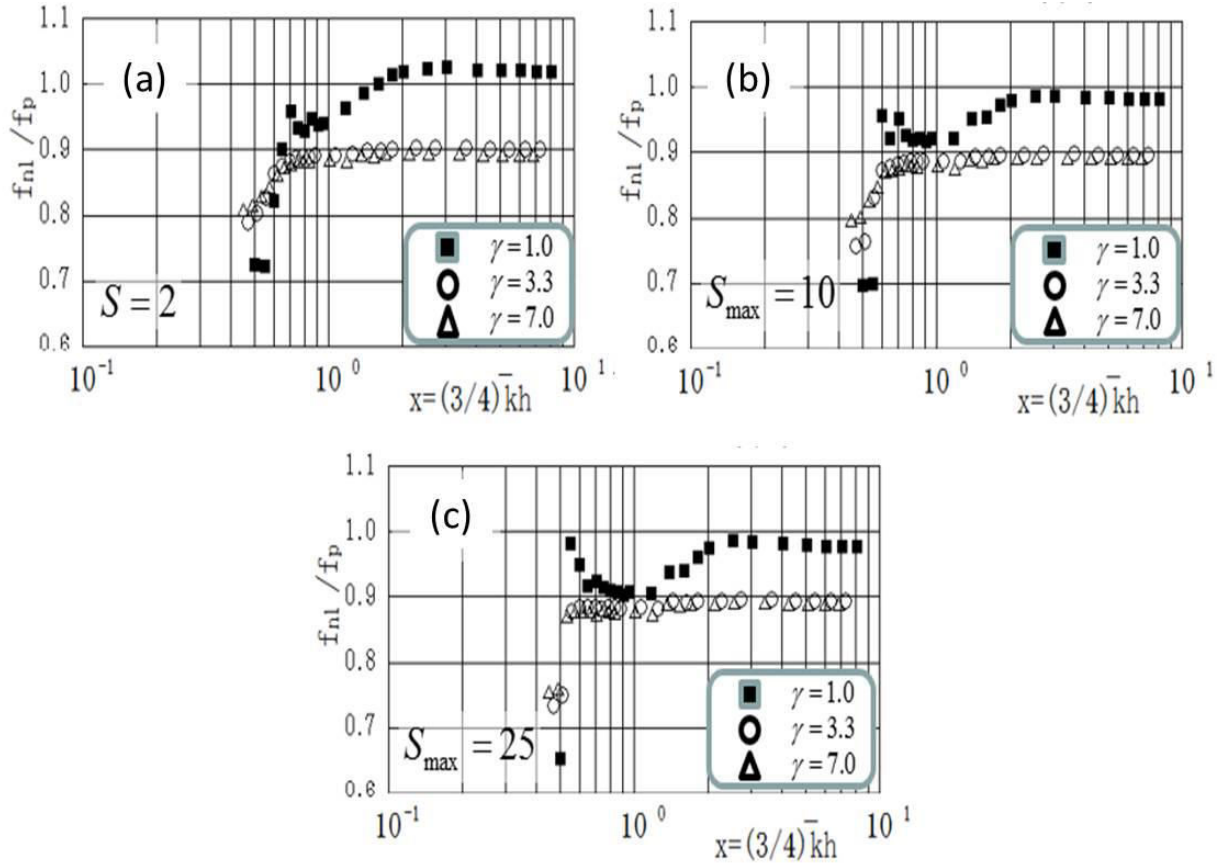
Figure 4.5. Downshift factor for various directional spectra in several water depths. ($x = (3/4)kh$ is the dimensionless depth).

4.4 Characteristics of Duration-Limited Evolutions and Frequency Downshifts in Finite-Water Depths in the FD-RIAM Method

We evaluated the characteristics of wave spectrum evolution under duration-limited conditions in finite water depths. Figure 4.6 show the long-term frequency spectrum evolution (2 h) computed in the WAM implemented with the FD-RIAM method by taking into account of only the nonlinear energy transfer term $S_{nl}(k_p h)$ for $k_p h = 1.0$, 0.8, and 0.6. The numerical simulations are carried out for the PM spectrum ($\gamma = 1.0$). The energy concentration parameter is $S_{max} = 10$, and the same value is used for the JONSWAP spectrum ($\gamma = 3.3$). The numerical results of the JONSWAP spectrum are show in Fig. 4.7. The horizontal axis is the frequency f divided by the frequency peak f_p, and the vertical axis is the energy density normalized by its peak value for the initial spectrum.

As can be seen in Figs. 4.6 and 4.7, the evolution of the spectra in finite-water depths is much faster than that in deep water. The frequency spectra in Figs. 4.6 and 4.7 are slightly different, but

the frequency spectra for $k_ph = 0.6$ seems very different from the others spectra. Although the spectra evolve by moving the peak frequency toward the low frequency end for deep water waves, as can be seen in Figs. 4.6 and 4.7, the spectra for $k_ph = 0.6$ in Figs. 4.6(c) and 4.7(c) evolve by transferring the energy toward the low frequency end by approximately keeping the peak frequency while decreasing the magnitude.

In addition, we applied the original WAM with the DIA method under the same conditions as those in Figs. 4.6 and 4.7. The results are shown in Fig. 4.8, where the evolution of the spectra is almost the same regardless of the water depth. This unusual condition may be caused by a "limiter" introduced in the WAM to suppress divergence of the computation.
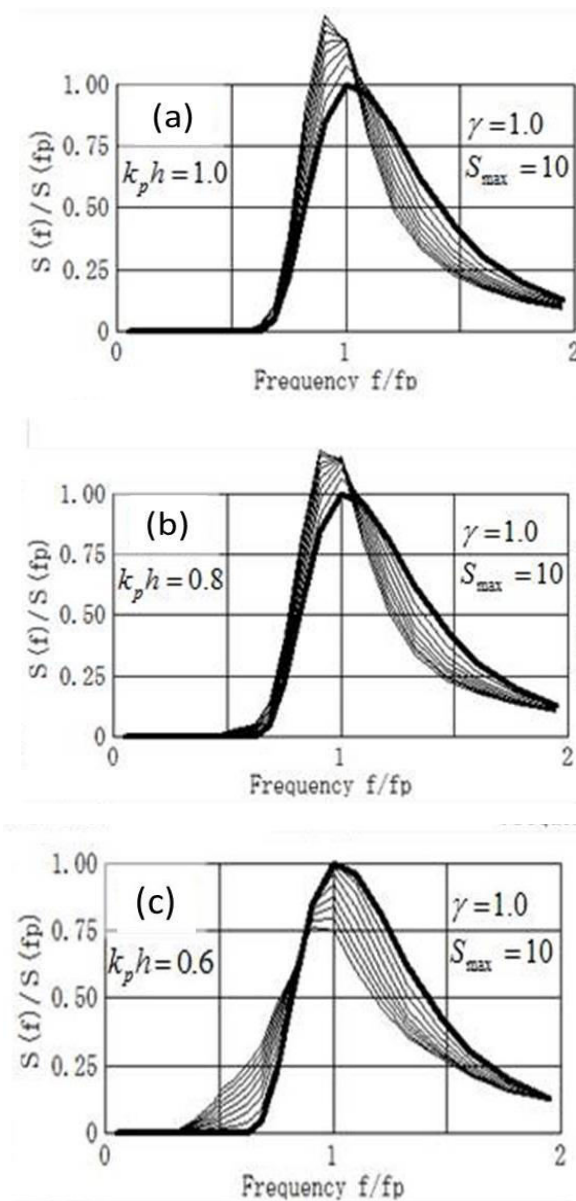
Figure 4.6. Duration-limited evolution (for 2 h) of the frequency spectra in the FD-RIAM method for the PM spectra in several water depths (only S_{nl} is applied).
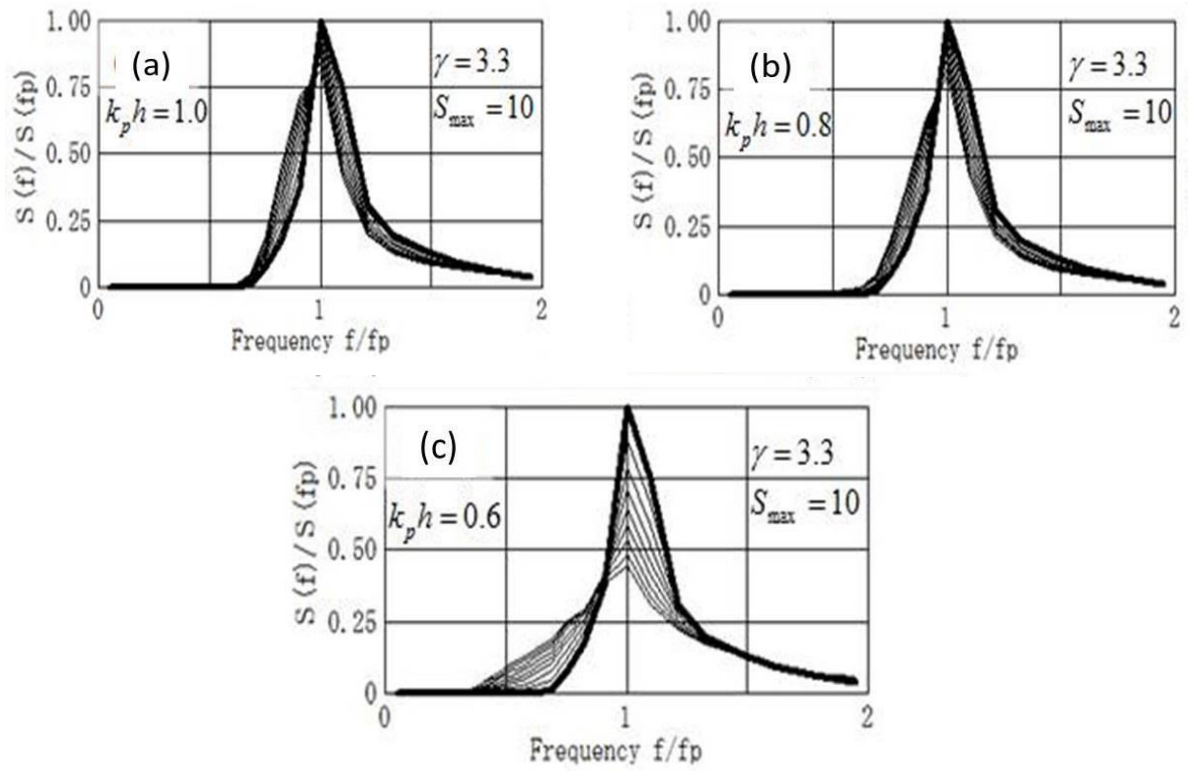
Figure 4.7. Duration-limited evolution (for 2 h) of the frequency spectra in the FD-RIAM method for the JONSWAP spectra in several water depths (only S_{nl} is applied).
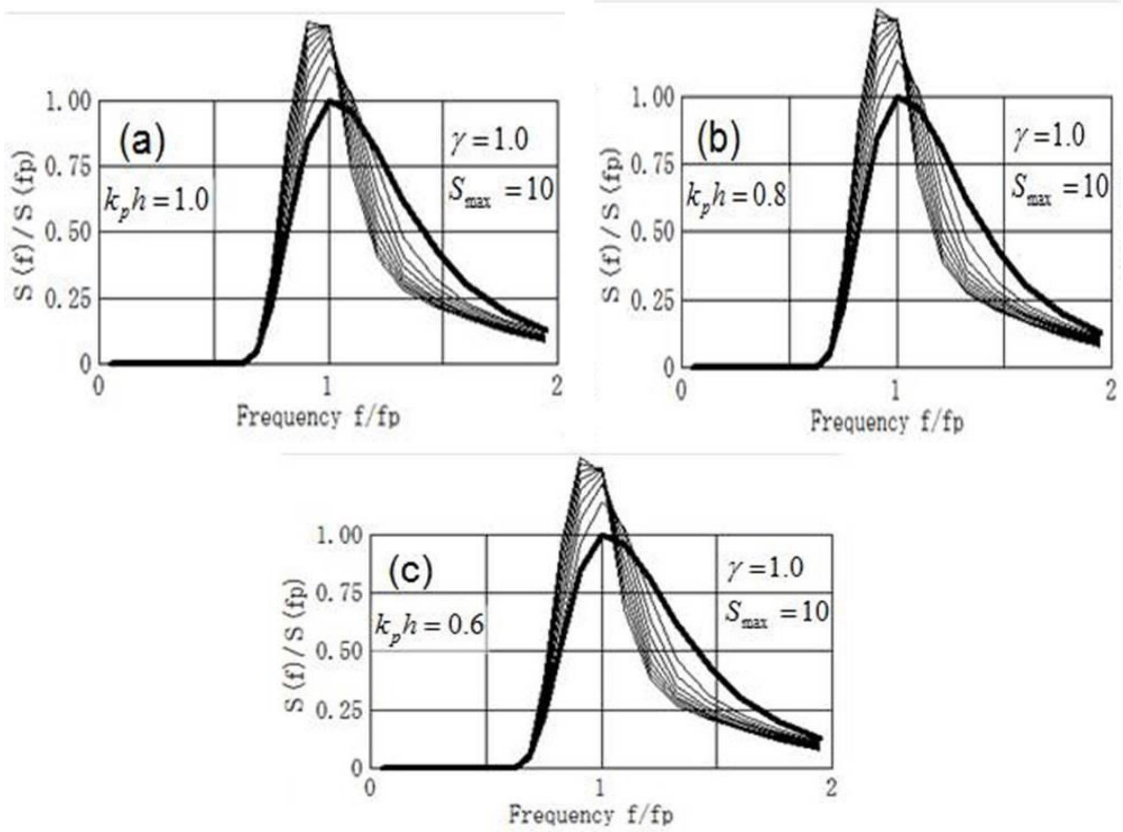
Figure 4.8. Duration-limited evolution (for 2 h) of the frequency spectra in the DIA methods with the enhancement factor R for the PM spectra in several water depths.

4.5. Conclusion

Characteristics of duration-limited evolutions and frequency downshift of the frequency spectra in finite water depths were investigated using a modified WAM implemented with the FD-RIAM method by Hashimoto et al. (1998, 2002). The evolution of the directional spectra in finite water depths caused by nonlinear energy transfer was confirmed in the FD-RIAM method to be much faster than that in deep water. The spectra evolve with their peak frequencies moved toward low frequencies for both the PM and JONSWAP spectra, thus maintaining the peak frequencies at almost the same frequency while decreasing the peak magnitude.

In this chapter, we also evaluated the enhancement factor and downshift factor used in the WAM. The enhancement factor R adopted in the WAM shows good agreement with those computed in the FD-RIAM method for small S_{max} and γ.

CHAPTER 5

EFFICIENT CONFIGURATIONS FOR COMPUTING NONLINEAR ENERGY TRANSFER

5.1 Introduction

Among the source terms in the third-generation wave models, the nonlinear energy transfer source term is known as the most important component in the evolution of wave spectra. To predict the evolution of wave spectra with high accuracy, the nonlinear energy transfer source functions must be estimated accurately. A precise evaluation of nonlinear energy transfer requires a large number of resonant configurations. Nevertheless, such calculations need huge computational costs and hence not suitable for operational wave models. Numerous efforts have been made to improve nonlinear energy transfer computations. However, the simplest method known as the DIA (Hasselmann et al., 1985) method is currently the most commonly used method for evaluating the nonlinear energy transfer spectrum S_{nl} in practical wave models because of its low computational cost. The DIA method used only a single configuration of resonant four waves for an infinite number of configurations. Hence, the DIA method is considered to have a limitation in accuracy.

Hashimoto and Kawaguchi (2001) developed the MDIA method by increasing the number of configurations in the DIA method so as to obtain more accurate nonlinear energy transfer computations. Each of the configurations uses different parameters λ and C, where λ is the parameter determining the combination of component waves. The optimum parameter C is estimated for each λ using the least-square method to exact the value computed in the RIAM method (Komatsu, et al., 1993). However, the applicability of the MDIA method has not been examined in wave models. In this chapter, as a preliminary study of the efficient number of resonance configurations, we examine the validity and effectiveness of the MDIA method under duration-limited conditions.

Moreover, Tamura et al. (2008) suggested the SRIAM method developed by Komatsu (1996), which is able to reduce computational costs by utilizing 20 configurations, to be incorporated

into operational wave models. As a result, wave model performance is significantly improved. However, even though there is an improvement, the computational cost is still 20 times larger than that of existing operational wave models using the DIA method. It is hence necessary to develop a method that can provide sufficient accuracy and efficiency, and practically be incorporated into wave models. Therefore, we modified the SRIAM method by reducing the number of resonant configurations. The resulting method is called the R-SRIAM method. The configurations for the R-SRIAM method are expected to be efficient configurations for nonlinear energy transfer computations.

In kernel function analysis, quasi-singular quadruplets contribute the most to nonlinear energy transfer, whereas regular quadruplets are expected to contribute far less (Masuda, 1980). This analysis is suitable for studying configurations of the R-SRIAM method. Consequently, the efficient resonant configuration numbers are proposed by selecting configurations only from the quasi-singular quadruplets. The resulting method is called the AM-DIA method. We compare numerical results of the R-SRIAM and AM-DIA methods with those of the RIAM and SRIAM method, which has been proved to have the same degree of accuracy as the exact methods developed by Komatsu et al. (1993) and Komatsu and Masuda (1996).

5.2 Numerical Examinations of the Multiple Discrete-Interaction Approximation Method

The validity and the effectiveness of the MDIA method are examined based on the previous numerical computation of Hashimoto and Kawaguchi (2001). This study is limited to deep water waves, and uses the JONSWAP-type frequency spectrum and Mitsuyatsu-type directional function (Eq. (3.2)). The PM spectrum ($\gamma = 1.0$) and the JONSWAP spectrum ($\gamma = 3.3$) with S_{max} = 10 are used for energy concentration parameter initial values of the directional spectrum. For initial conditions, the significant wave height and period are used based on Goda's formula (Eq. (3.6)). The optimum parameters of the MDIA method proposed by Hashimoto and Kawaguchi (2001) are shown in Table 2.4 in Chapter 2. The optimum parameters of λ and C are listed for each configuration.

Figure 5.1 shows the nonlinear energy transfer spectrum for a test wave spectrum as a function of frequency in the RIAM and MDIA methods for various configuration numbers. The upper panels of Fig. 5.1 show the nonlinear energy transfer spectrum for the PM spectrum, and the lower panels show the JONSWAP spectrum. The solid red line shows the nonlinear energy transfer in

the RIAM method, and the dotted black line is in the MDIA method. It can be seen that the accuracy of the MDIA method is improved as the number of configurations increases under the some spectrum conditions. However, a negative value of C is used in the computation although C should be positive in the original Boltzmann integral. This is because the parameter C is estimated using the simple least-square method.
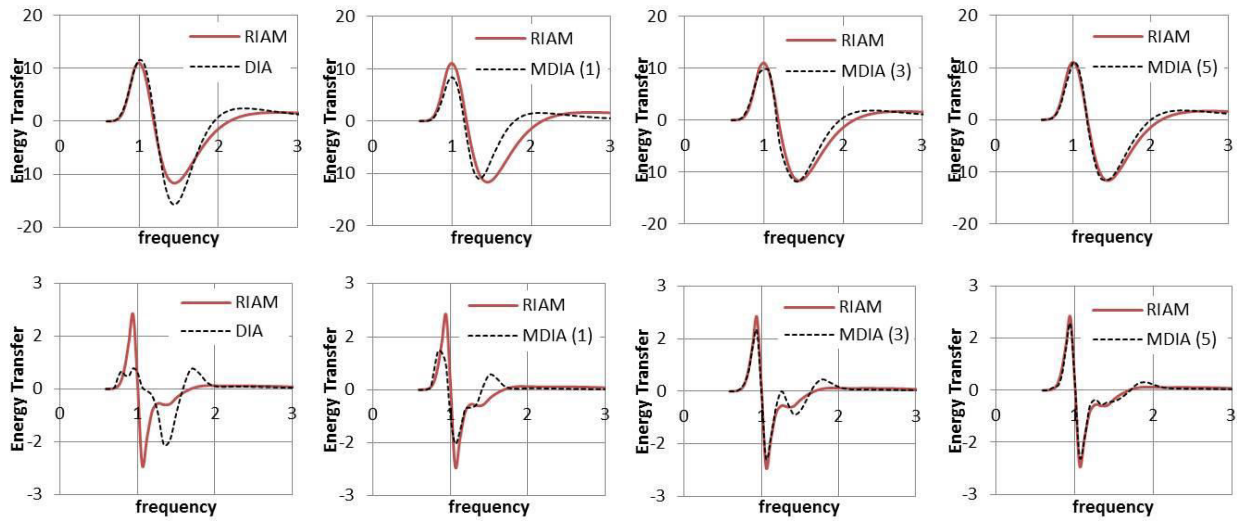
Figure 5.1. Nonlinear energy transfer spectra for a test wave with the PM (upper panels) and JONSWAP (lower panels) spectra.

In order to confirm the behavior of the nonlinear energy transfer spectrum in the MDIA method, the optimum configurations are incorporated into the WAM. It was found that under duration-limited condition the MDIA method is applicable only in a short time for the time integration. The negative value of C seems to make the computation unstable as time evolves. Although for the test wave spectrum the MDIA method has higher accuracy than the original DIA method, it is still impractical to be implemented in wave models.

5.3 Reduced Simplified Research Institute for Applied Mathematics Method

The SRIAM method is known as a superior method for computing nonlinear energy transfer compared with the DIA and RIAM methods (Hashimoto, 2012). It have been demonstrated that computations in the SRIAM method are 100 times faster than those in the RIAM method. The SRIAM method is almost perfect in accuracy and practicality for adoption in wave models. The performance of wave models was remarkably improved in the SRIAM method. However, the computational cost of the SRIAM method, which uses 20 configurations, is still larger than that of existing wave models using the DIA method.

Table 5.1. Optimum parameters for the R-SRIAM method: singular quadruplets (i_rep: 1–7) and regular quadruplets (i_rep: 8–9).

i_rep	$\tilde{\theta}_1$	$\tilde{\omega}_3$	$\tilde{\theta}_3$	γ	$\log_{10}\tilde{K}$	C_irep
1	0	0.88	10	0.000	2.15	1.00
2	0	0.78	20	0.000	1.85	1.00
3	0	0.7	30	0.000	1.11	1.00
4	0	0.63	40	0.000	0.40	1.00
5	0	0.57	50	0.000	-0.29	1.00
6	0	0.52	60	0.000	-0.92	1.00
7	0	0.49	70	0.000	-1.51	1.00
8	0	0.62	30	0.009	-0.64	2.01
9	10	0.75	30	-0.004	0.98	1.96

In order to reduce the computational costs, in this study, we modified the SRIAM method by reducing the number resonant configurations. It was found that nine configurations yield a nonlinear energy transfer spectrum as accurate as that in the original SRIAM method. The modified method is called the R-SRIAM method.

The optimum parameters in the R-SRIAM method are shown in Table 5.1, which consists of seven quasi-singular quadruplets and two regular quadruplets. It is verified that the quasi-singular quadruplets contribute to nonlinear energy transfer more than the regular quadruplets. The leftmost column in Table 5.1 is the number of resonant configurations, $\tilde{\theta}_1$ and $\tilde{\theta}_3$ are the angles of the wave vectors $\boldsymbol{k}_1$ and $\boldsymbol{k}_3$, respectively, $\tilde{\omega}_3$ is the normalized angular frequency $(\tilde{\omega}_4 = 1)$, and $\tilde{K}$ is the kernel function for a specific quadruplet.
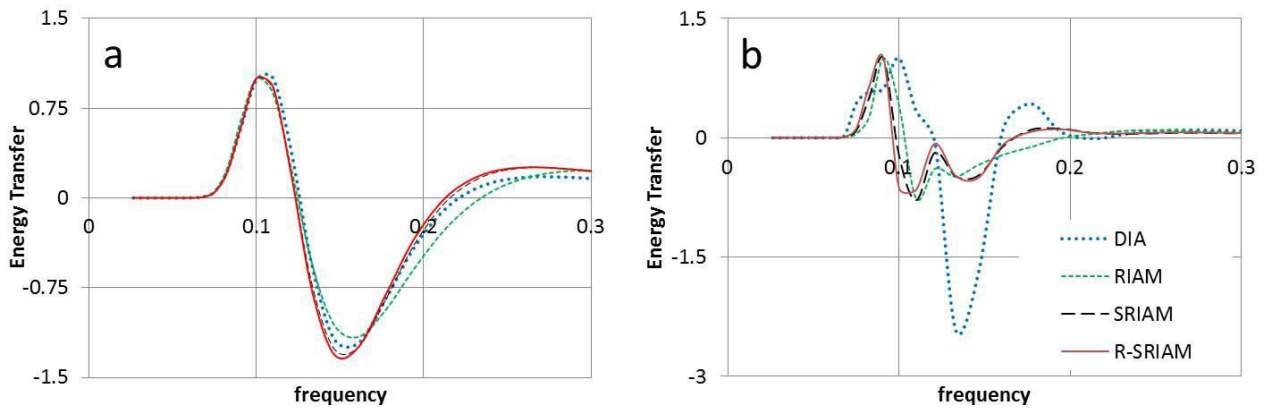
Figure 5.2. Comparison of the nonlinear energy transfer spectrum for a test wave with the (a) PM and (b) JONSWAP spectra in the R-SRIAM, DIA, RIAM and the original SRIAM methods.

Figure 5.2 shows a comparison of the nonlinear energy transfer spectrum for a test wave with the (a) PM and (b) JONSWAP spectra in the R-SRIAM, DIA, RIAM and the original SRIAM methods. The horizontal axis is the frequency, and the vertical axis is the nonlinear energy transfer normalized by the maximum value in the RIAM method. It is clearly shown that the R-SRIAM method has a result slightly different from that of the RIAM method, while the result has almost the same degree of accuracy as that of the original SRIAM method. However, it is very different from the result of the DIA method, especially for the JONSWAP spectrum. The nonlinear energy transfer spectrum in the DIA method for the JONSWAP spectrum shows an overshoot in the maximum negative lobe (Fig. 5.2(b)).

Figures 5.3 and 5.4 show a comparison of the two-dimensional nonlinear energy transfer spectrum calculated using the DIA, RIAM, original SRIAM, and R-SRIAM methods with the same nonlinear energy transfer functions as those in Fig. 5.2 (a) and (b), respectively. As can be seen in Fig. 5.3, the R-SRIAM method obviously agrees well with those obtained in the original RIAM method as shown in Fig. 5.2(a). This result indicates that the reduced configuration number used in the SRIAM method yields the same accuracy as that in the original SRIAM method. Meanwhile, for the JONSWAP spectrum the result of the R-SRIAM method is slightly different from those of the RIAM and SRIAM method, but significantly different from that of the DIA method.
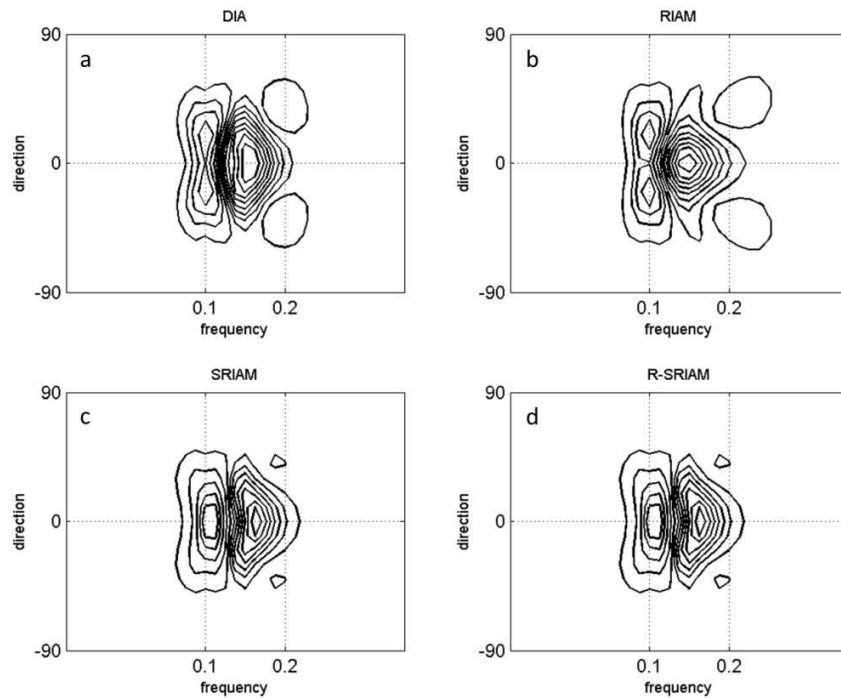
Figure 5.3. Comparison of the two-dimensional nonlinear energy transfer spectrum obtained using the (a) DIA, (b) RIAM, (c) SRIAM, and (d) R-SRIAM methods for the PM spectrum.
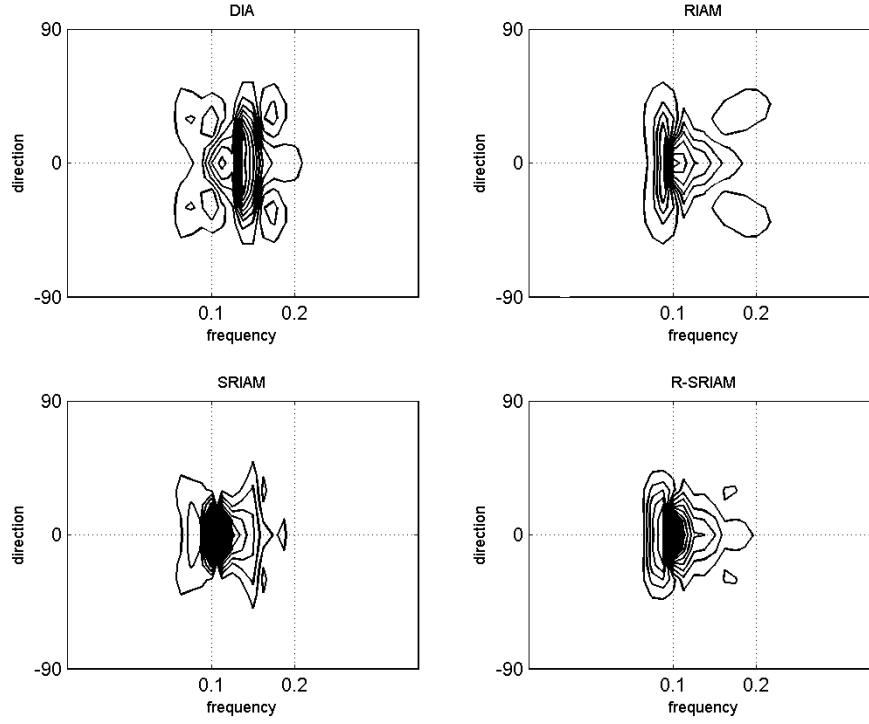
Figure 5.4. Comparison of the two-dimensional nonlinear energy transfer spectrum obtained using the (a) DIA, (b) RIAM, (c) SRIAM, and (d) R-SRIAM methods for the JONSWAP spectrum.

Furthermore, the R-SRIAM method is implemented in the WAM for 12 h simulations. The simulations were performed by taking into account only the nonlinear energy transfer (S_{nl}), without the wind input ($S_{in} = 0$) and dissipation ($S_{dis} = 0$). The energy concentration parameters are $\gamma = 3.3$ and $S_{max} = 15$. The peak frequency f_p is set at 0.12 Hz. The initial frequency spectrum and the frequency spectra after 6 h and 12 h of simulations in the R-SRIAM, DIA, RIAM, and the original SRIAM methods are shown in Figs. 5.5(a) and 5.5(b), respectively. It can be seen that the initial peak frequency at 0.12 Hz moves toward the low frequency end after 6 h and 12 h of simulation in all of the methods. Moreover, the energy transfer spectrum seems to be different in all of the methods. After 6 h and 12 h of simulation, the spectra peak value in the RIAM method tends to overshoot. However, it should be noted that the R-SRIAM method yields a smooth and continuous frequency downshift as the original SRIAM method does, whereas the original WAM in the DIA method shows relatively distorted frequency downshift for the frequency spectra.

Figures 5.5 and 5.6 show the nonlinear energy transfer spectrum at $t = 0$, 6, and 12 h. The intensity of the nonlinear energy transfer spectrum decreases as time evolves. While the nonlinear energy transfer spectrum in each method seems to be different, the one in the R-

SRIAM method is in agreement with that in the original SRIAM method. Meanwhile, at $t = 0$, the nonlinear energy transfer spectrum in the DIA method shows a different pattern and it tends to overshoot at the peak of the negative lobe.

Figure 5.5. Initial frequency spectrum and the frequency spectra in the R-SRIAM, DIA, RIAM, and the original SRIAM methods at (a) $t = 6$ h and (b) $t = 12$ h (only S_{nl} is applied).

Fig 5.6. Nonlinear energy transfer spectrum corresponding to the frequency spectrum in Figs. 5.5(a) and 5.5(b) at (a) $t = 0$, (b) $t = 6$ h, and (c) $t = 12$ h.
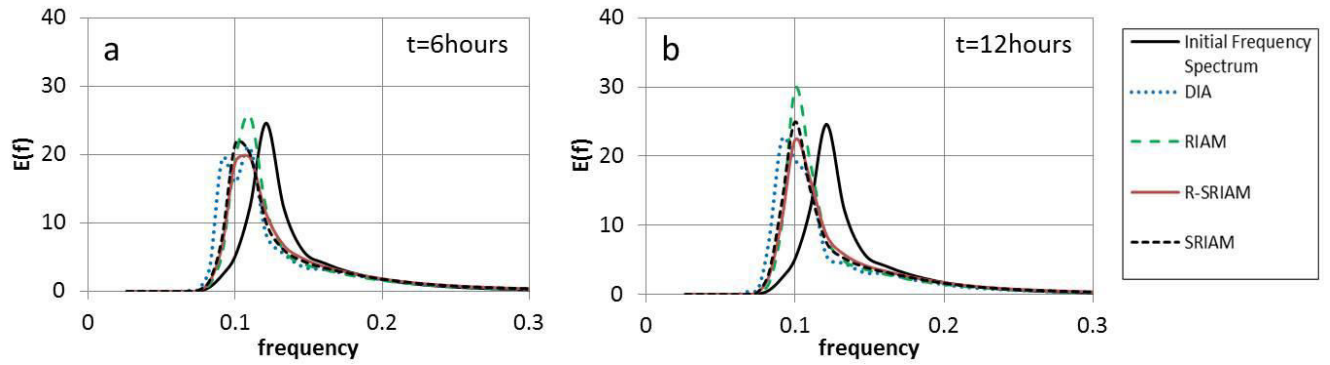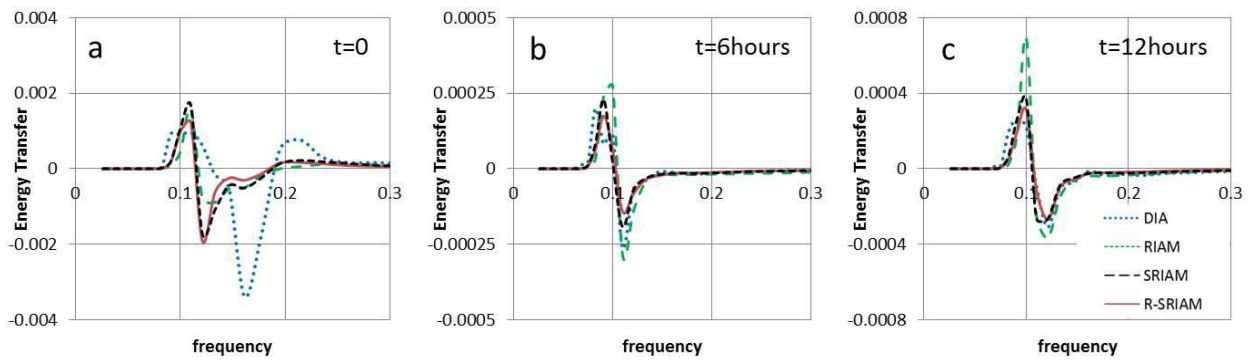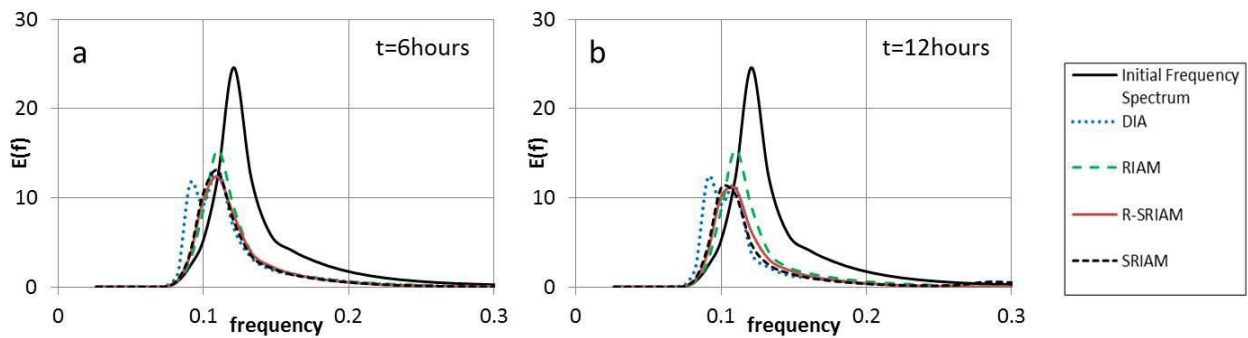

Figure 5.7. Initial frequency spectrum and the frequency spectra in the R-SRIAM, DIA, RIAM, and the original SRIAM methods at (a) $t = 6$ h and (b) $t = 12$ h (S_{in} and S_{dis} are applied).
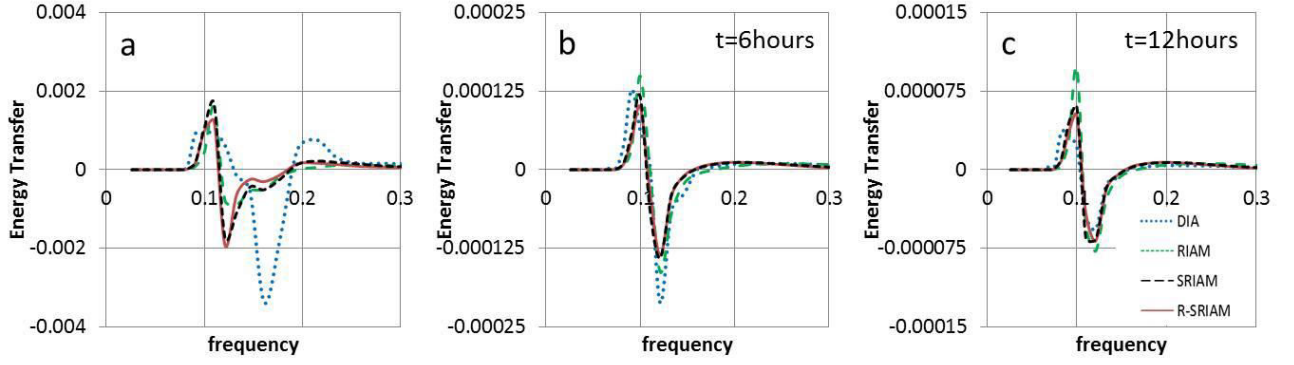
Figure 5.8. Nonlinear energy transfer spectrum corresponding to the frequency spectrum in Figs. 5.7(a) and 5.7(b) at (a) t = 0, (b) t = 6 h, and (c) t = 12 h.

The R-SRIAM method is also incorporated in WAM by taking into account the wind input S_{in} and dissipation S_{dis} under conditions similar to those in previous simulations. The frequency spectrum in the R-SRIAM method shows the same degree of accuracy as that in the original SRIAM method. The energy density decreases and the peak frequency downshifts after 6 h and 12 h of simulation are shown in Fig. 5.7. The spectral peak magnitude and corresponding nonlinear energy transfer spectrum in the RIAM method seem slightly different from those in the SRIAM and R-SRIAM methods, but significantly different from those in the DIA method. The DIA method seems to yield the approximate frequency downshift as shown by the double peak of the frequency spectrum after 6 h and 12 h of simulation. The maximum negative value of the nonlinear energy transfer spectrum in the DIA method tends to overshoot at the initial time. This result shows that by reducing the number of configurations, the R-SRIAM method can be incorporated in wave models without sacrificing the accuracy of the original SRIAM method. Because only nine configurations are used, the R-SRIAM method is more economical than the original SRIAM method. However, compared with the DIA method, the R-SRIAM method yields better accuracy but has longer computational time.

5.4 Alternative Multiple Discrete-Interaction Approximation Method

It is preferred to process singular configurations because it improves the accuracy with less computation time. Therefore, the effective configurations for computing nonlinear energy transfer are proposed using only the quasi-singular quadruplets, known as the AM-DIA method. The independent variables of this method are the frequency and direction angles $(\theta_1, \omega_3, \theta_3)$, same as those of the RIAM and SRIAM methods.

67

The optimized quadruplets are up to five configurations used to represent the infinite number of resonant configurations. The coefficients of those parameters were defined similarly to those in the SRIAM method, based on the RIAM method for eight test spectra with the JONSWAP-type spectrum. The optimum parameters of the AM-DIA method for various configuration numbers are listed in Table 5.2. The leftmost column is the number of quasi-singular quadruplets used in the calculation. The optimization of those coefficient parameters is carried out using the nonnegative least square method.

Table 5.2. Optimum parameters in the AM-DIA method for various configuration numbers.

No. of Conf	$\tilde{\theta}_1$	$\tilde{\omega}_3$	$\tilde{\theta}_3$	$\tilde{K}$
1	0	0.78	20	102.59
2	0	0.78	20	58.78
	0	0.7	30	21.13
3	0	0.78	20	45.72
	0	0.70	30	9.05
	0	0.63	40	17.34
4	0	0.88	20	63.90
	0	0.70	30	10.36
	0	0.63	40	7.72
	0	0.57	50	1.91
5	0	0.88	10	176.68
	0	0.78	20	88.76
	0	0.63	40	13.58
	0	0.57	50	0.35
	0	0.49	70	0.18

Each configuration number listed in Table 5.2 is implemented in the WAM. The numerical simulations are performed under duration-limited conditions for 12 h for the PM and JONSWAP spectra, without taking into account the wind input and dissipation. Figures 5.9 and 5.11 show a comparison of the nonlinear energy transfer spectrum in the AM-DIA, DIA, RIAM, and SRIAM methods for the PM and JONSWAP spectra, respectively. The nonlinear energy transfer spectrum in the AM-DIA method for up to five configurations is denoted in the figures by solid red lines. Moreover, Figs 5.10 and 5.12 shows the two-dimensional nonlinear energy transfer spectrum in the AM-DIA method for up to five configurations.

As shown in the Fig. 5.9, the accuracy of the nonlinear energy transfer spectrum for the PM spectrum in the AM-DIA method generally improves as the number of configurations increases. For the JONSWAP spectrum in Fig. 5.11, the AM-DIA method with more than 2 configurations

turns out to give an unrealistic pattern for nonlinear energy transfer spectrum. When only one configuration is used, the accuracy of the nonlinear energy transfer spectrum for the PM spectrum in the AM-DIA method is low compared with those in the RIAM and SRIAM methods, while the magnitude of the nonlinear energy transfer spectrum in the DIA method is larger than that in the RIAM and SRIAM methods. However, for the JONSWAP spectrum, the AM-DIA method with one configuration yields the nonlinear energy transfer spectrum similar to those in the RIAM and SRIAM methods, in contrast to the DIA method.

Incidentally, the AM-DIA method is incorporated in the WAM and the integration is carried out under duration-limited conditions for 12 h of simulation to investigate stability of the computation during the integration procedure. The simulations are performed for up to five configurations for the PM and JONSWAP spectra. The simulation results are shown in Figs. 5.14–5.20.

Figure 5.9. Comparison of the nonlinear energy transfer spectrum for the PM spectrum in the AM-DIA, DIA, RIAM, and SRIAM methods at $t = 0$.
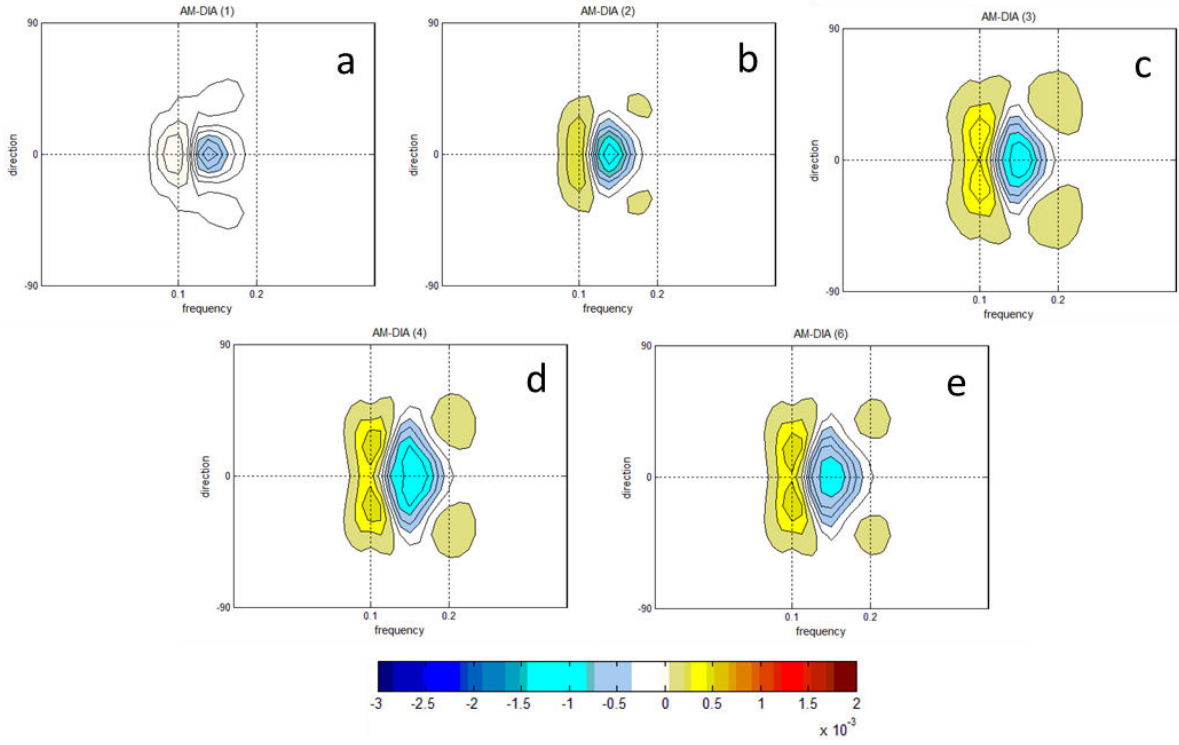
Figure 5.10. Two-dimensional nonlinear energy transfer spectrum in the (a) AM-DIA (1), (b) AM-DIA (2), (c) AM-DIA (3), (d) AM-DIA (4), and (e) AM-DIA (5) methods with the same model parameters and wave spectrum as those in Fig. 5.9.
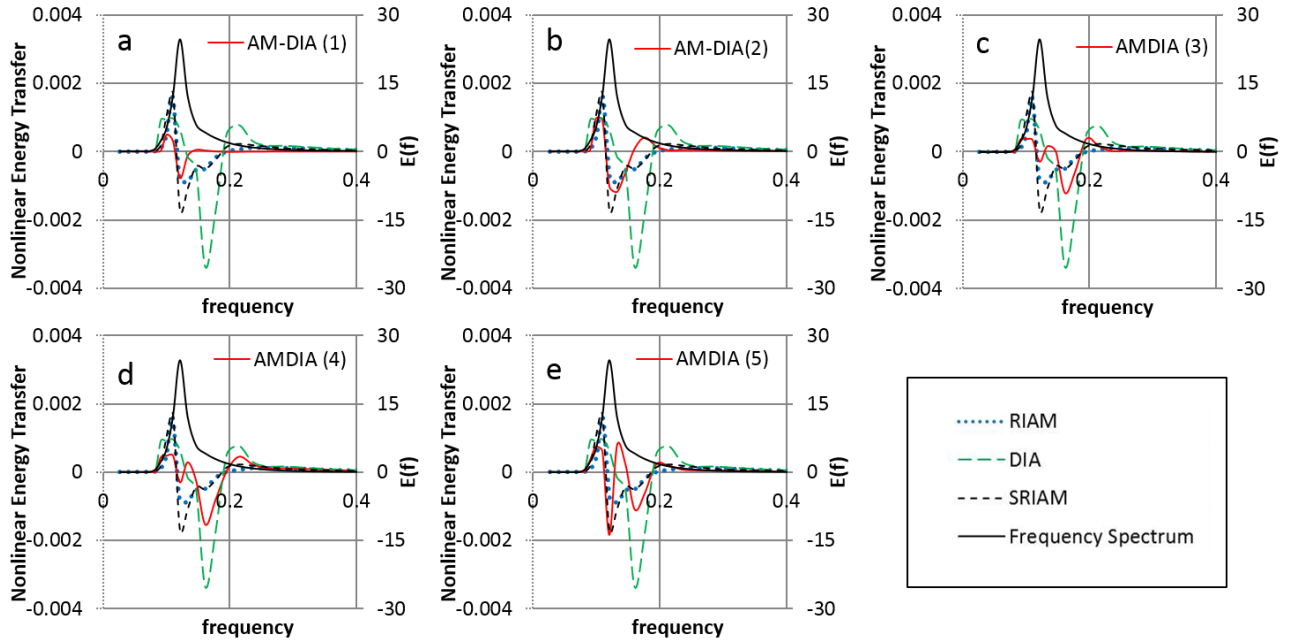
Figure 5.11. Comparison of the nonlinear energy transfer spectrum for the JONSWAP spectrum in the AM-DIA, DIA, RIAM, and SRIAM methods at $t = 0$.
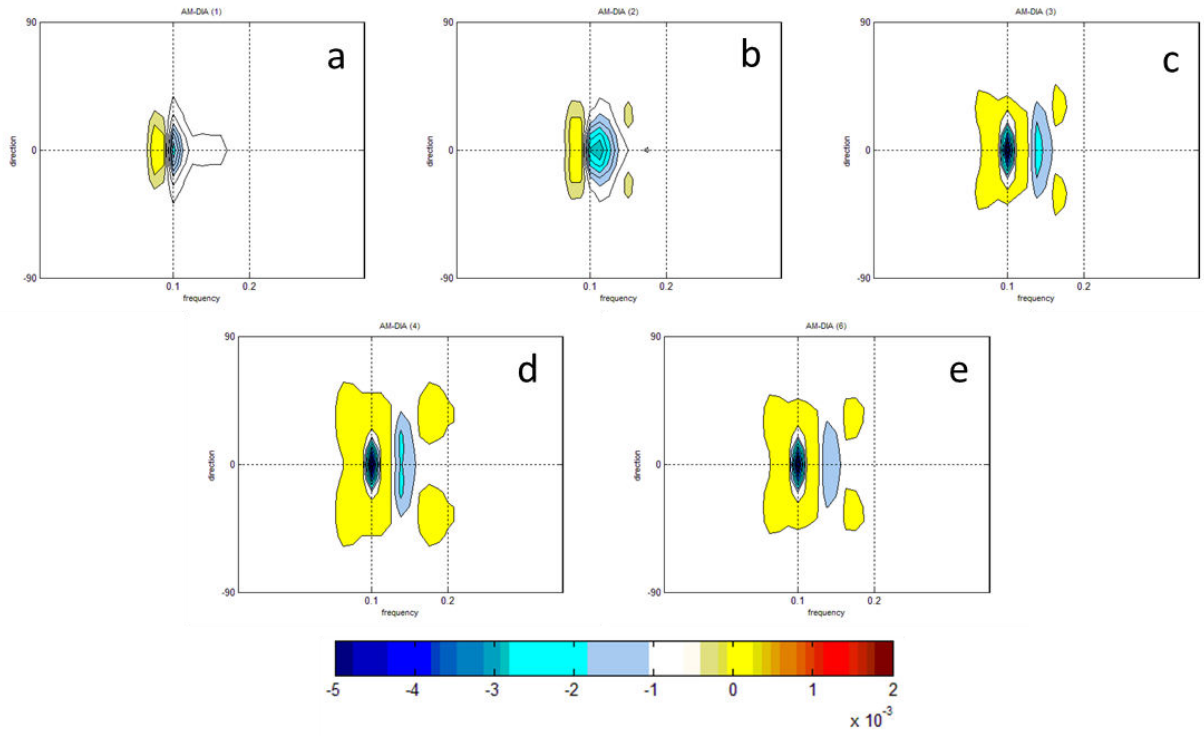
Figure 5.12. Two-dimensional nonlinear energy transfer spectrum in the (a) AM-DIA (1), (b) AM-DIA (2), (c) AM-DIA (3), (d) AM-DIA (4), and (e) AM-DIA (5) methods with the same model parameters and wave spectrum as those in Fig. 5.9.

Figure 5.13. Comparison of the frequency spectrum for the PM spectrum in the AM-DIA, DIA, RIAM, and SRIAM methods at t = 12 h.
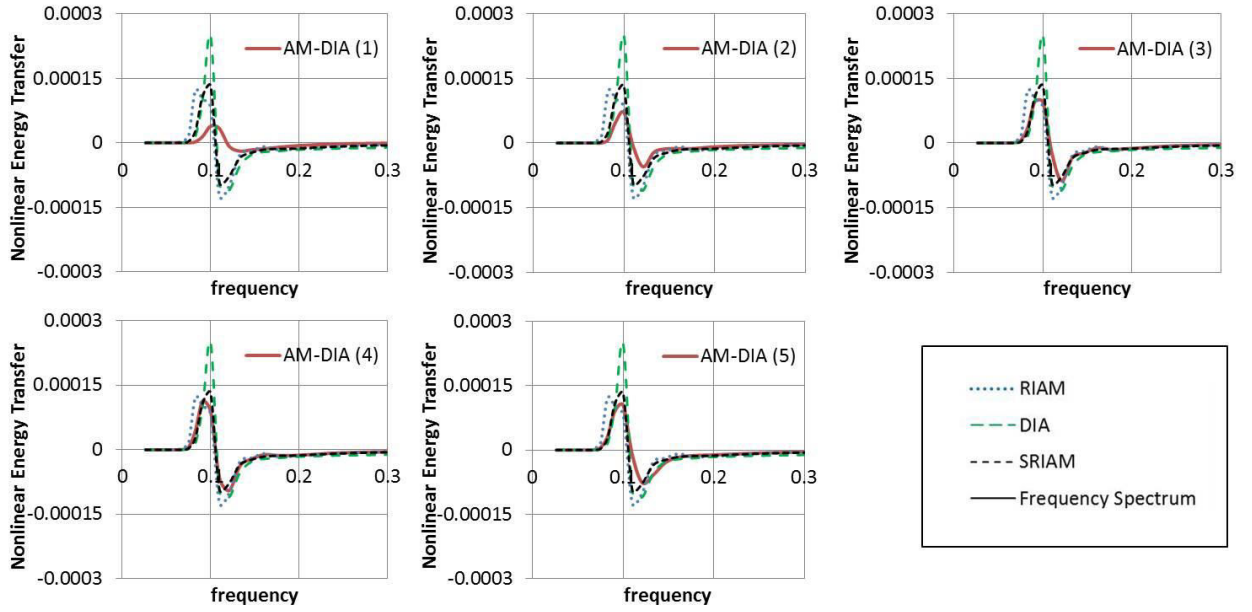
Figure 5.14. Comparison of the nonlinear energy transfer spectrum for the PM spectrum in the AM-DIA, DIA, RIAM, and SRIAM methods at t = 12 h.
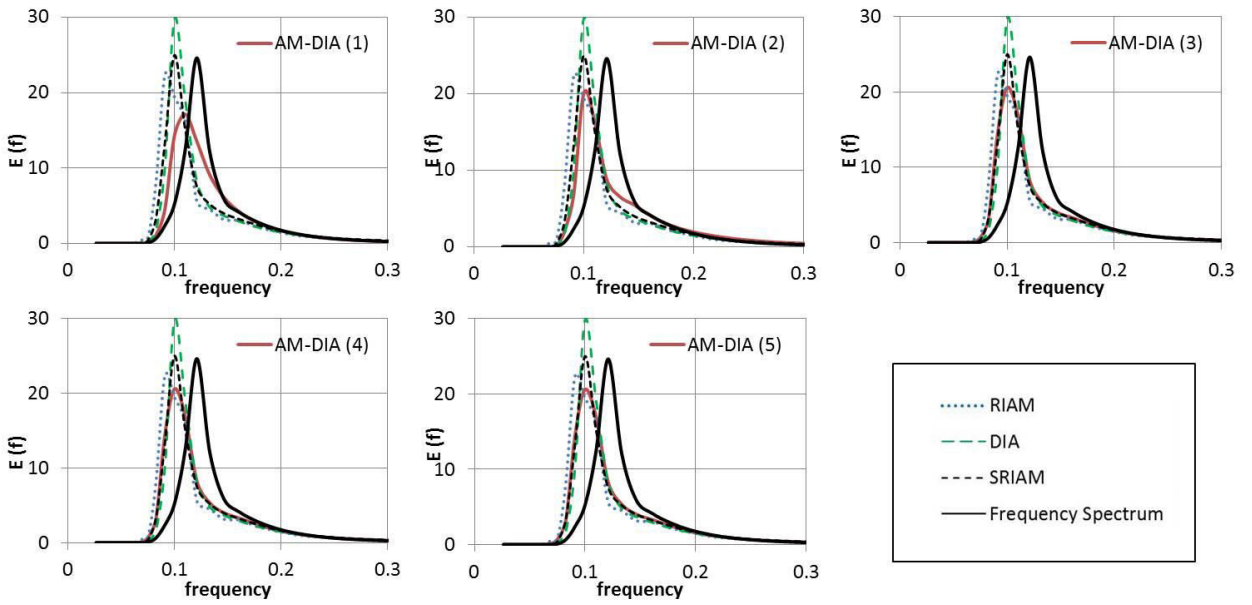
Figure 5.15. Comparison of the frequency spectrum for the JONSWAP spectrum in the AM-DIA, DIA, RIAM, and SRIAM methods at t = 12 h.
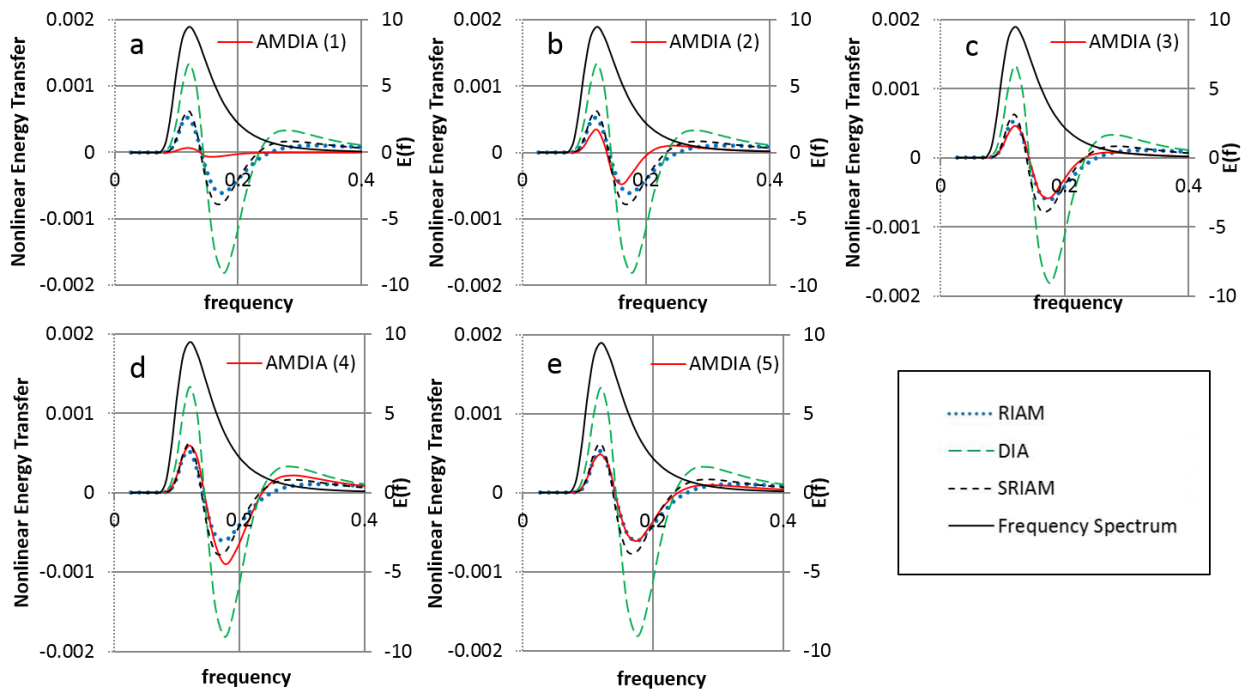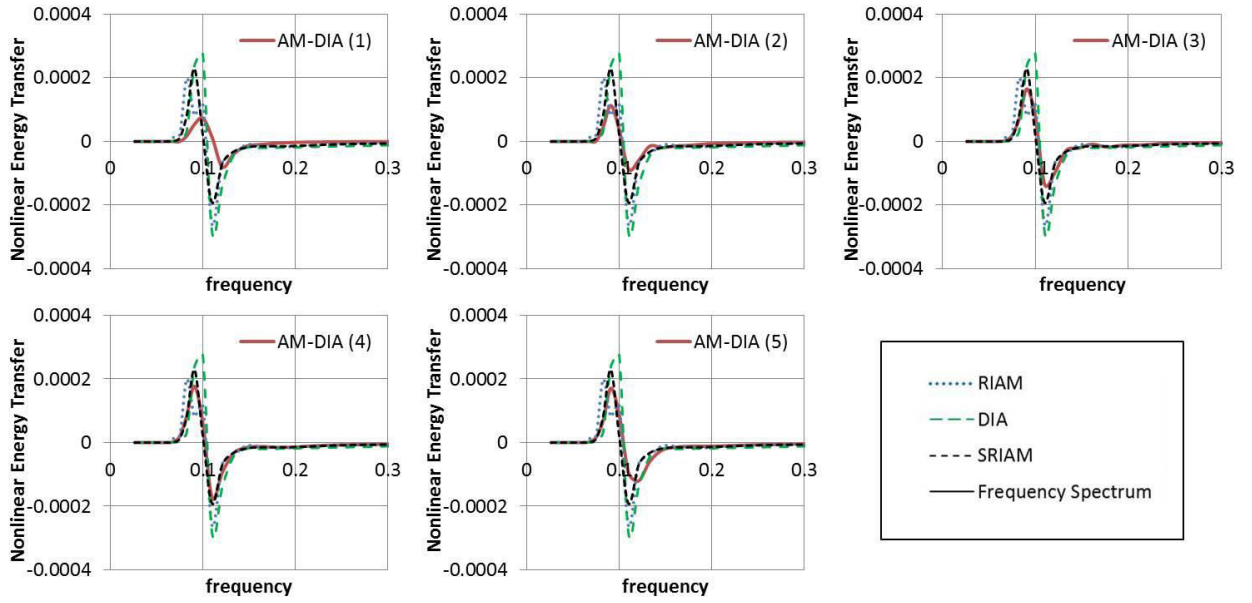
Figure 5.16. Comparison of the nonlinear energy transfer spectrum for the JONSWAP spectrum in the AM-DIA, DIA, RIAM, and SRIAM methods at t = 12 h.
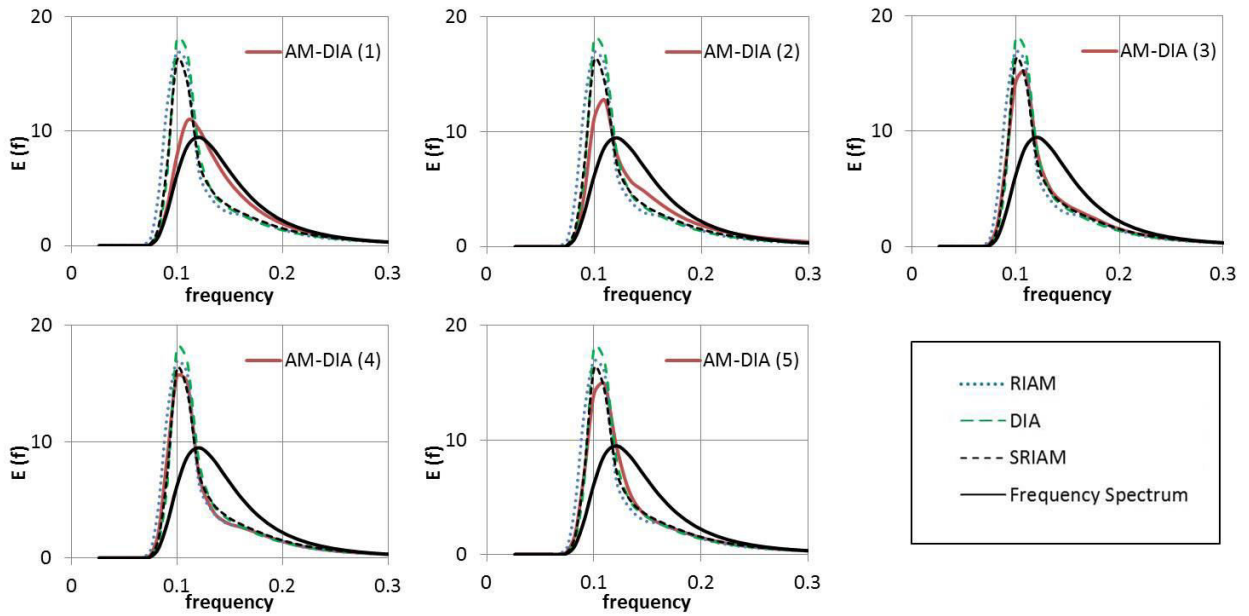
Figures 5.13 and 5.15 show a comparison of the frequency spectra for the PM and JONSWAP spectrum, respectively, between the AM-DIA, DIA, RIAM and SRIAM methods after 12 h of simulations. Up to five configurations are used in the AM-DIA method, and the number of configurations used is denoted by the number inside the parentheses, e.g., AM-DIA (3) means three configurations are used. Meanwhile, the corresponding nonlinear energy transfer spectra are shown in Figs. 5.14 and 5.16 for the PM and JONSWAP spectra, respectively. The AM-DIA results are denoted by red solid lines in all of these figures.

The frequency downshift of the PM spectrum is clearly shown in Fig. 5.13, except for the frequency spectrum in the AM-DIA method with only one configuration (Fig. 5.13 (a)). After 12 h of simulation, the spectra in the RIAM, SRIAM, and DIA methods show a narrow shape. For the JONSWAP spectrum, all of the frequency spectra show obvious frequency downshift and a shape similar to the initial spectrum (Fig. 5.15). However, for the PM spectrum the AM-DIA (1) result does not show frequency downshift at t =12 h, in contrast to the other AM-DIA results. The AM-DIA (1) frequency downshift for the PM spectrum seems slower than the other AM-DIA results. The same feature is observed for the JONSWAP spectrum. The magnitude and location of the frequency peak slightly in the AM-DIA (1) method differs from those in the RIAM, SRIAM, and DIA methods.

The frequency spectrum in the AM-DIA (2) method agrees well with that in the SRIAM method for both the PM and JONSWAP spectra, so does the nonlinear energy transfer spectrum after 12 h of simulation. As can be seen in Fig. 5.16, the unrealistic pattern of the nonlinear energy transfer spectrum in AM-DIA (2) method shows up only at the initial time but not at late times. The nonlinear energy transfer spectra in the AM-DIA (3) and (4) methods seem to have the same accuracy as those in the SRIAM method.
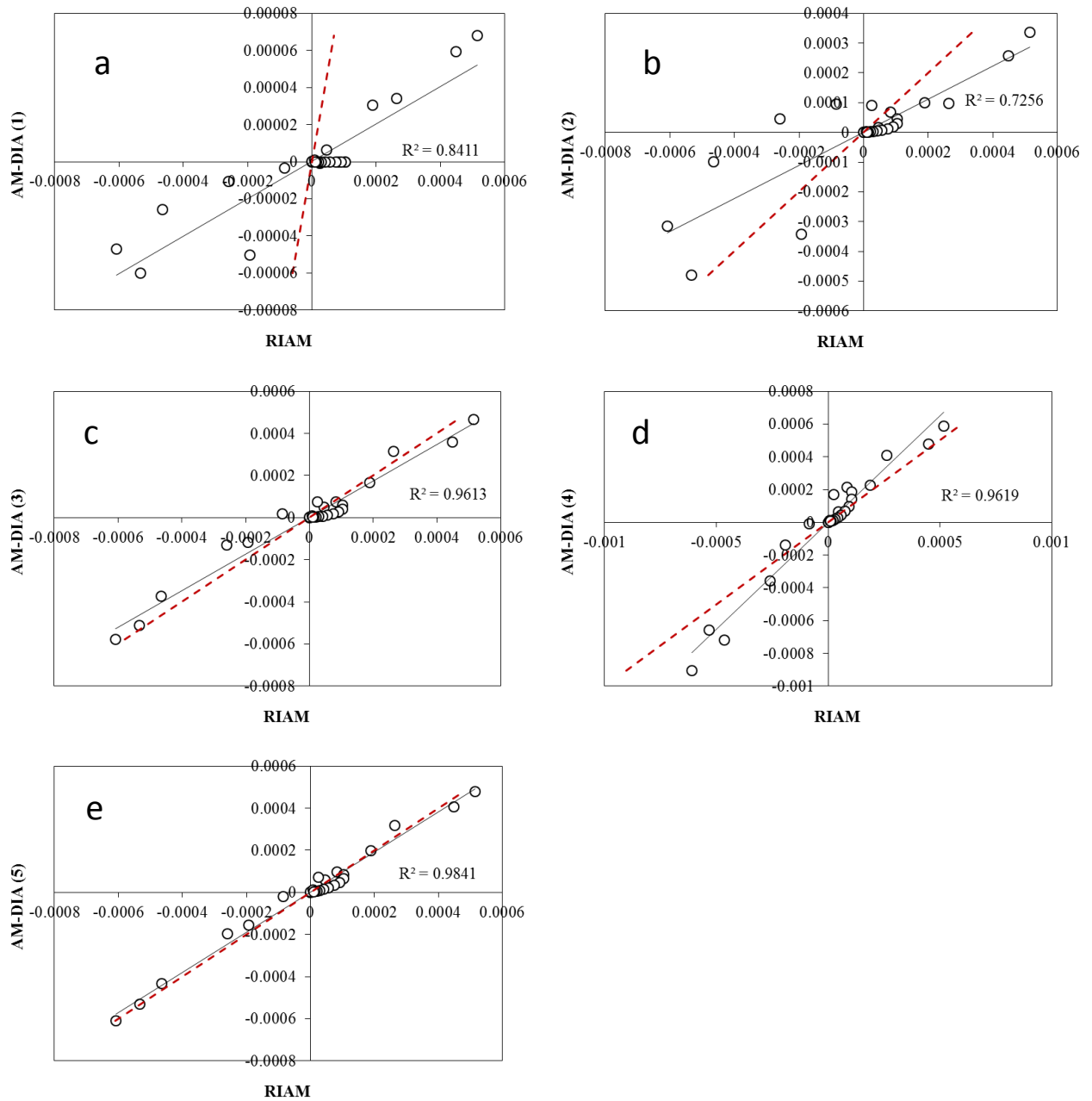
Figure 5.17. Correlation of the nonlinear energy transfer spectrum for the PM spectrum between the RIAM method and the AM-DIA (1), (2), (3), (4), and (5) in (a), (b), (c), (d), and (e), respectively, at the initial time.
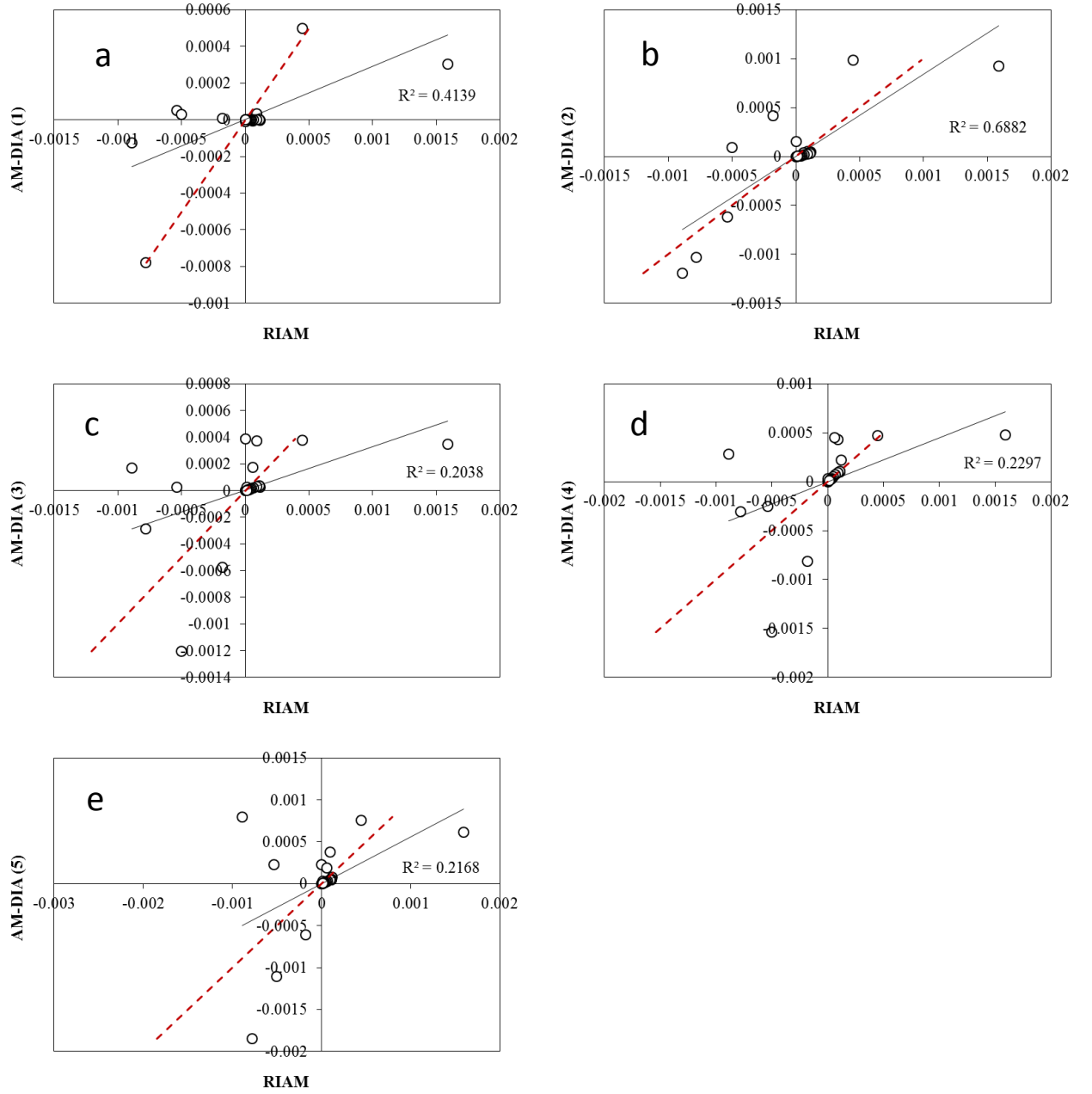
Figure 5.18. Correlation of the nonlinear energy transfer spectrum for JONSWAP spectrum by AM-DIA (1), (2), (3), (4), and (5) in (a), (b), (c), (d), and (e), respectively, at the initial time.

To quantify the accuracy of the nonlinear energy transfer spectrum in the AM-DIA method and hence to find the most efficient configuration number, the correlation of the nonlinear energy transfer spectra in the AMDIA and RIAM methods are examined. The result is shown in Figs. 5.17 and 5.18, for the PM and JONSWAP spectra, respectively. The horizontal and vertical axes are the nonlinear energy transfer spectra as a function of frequency in the RIAM and AM-DIA methods, respectively. The nonlinear energy transfer was integrated with respect to direction

angles. The black solid line is the trend line of the AM-DIA data, while the red dash line is the trend line of the RIAM data.

As can be seen in Figs. 5.17 and 5.18, the correlation between the AM-DIA and RIAM methods for the PM spectrum is stronger than that for the JONSWAP spectrum. The AMDIA (5) method has the strongest correlation with the RIAM method for the PM spectrum than the other AM-DIA methods. However, for the JONSWAP spectrum, the correlation of the nonlinear energy transfer spectrum in the AM-DIA (3), (4), and (5) methods is moderately strong. Only the AM-DIA (2) method has good correlation with the RIAM method for both the PM and JONSWAP spectra.

Table 5.3 Residual mean and variance of the nonlinear energy transfer spectrum for the PM and JONSWAP spectra in the AM-DIA method normalized by the residual mean and variance in the DIA method.

Number of configurations	Residual Mean		Residual Variance	
	PM	JONSWAP	PM	JONSWAP
1	0.57	0.42	0.25	0.19
2	0.37	0.37	0.09	0.10
3	0.16	0.57	0.01	0.26
4	0.25	0.56	0.05	0.30
5	0.10	0.67	0.00	0.40

Figure 5.19. Residual variance in the MDIA method normalized by that in the DIA method.

Furthermore, the residual mean and variance of the nonlinear energy transfer spectrum in the AM-DIA and RIAM methods for the PM and JONSWAP spectra are calculated and listed in Table 5.3. Figure 5.19 shows the AM-DIA residual mean and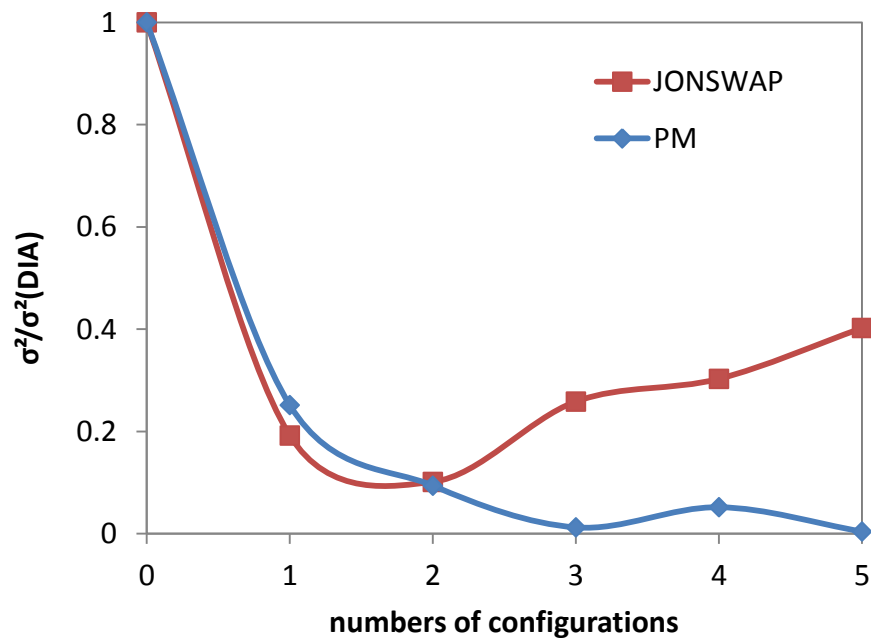 variance, which are normalized by those of the DIA method. As shown in Table 5.3 and Fig. 5.19, their accuracy for the PM and JONSWAP spectra is different. For the PM spectrum, the highest accuracy is obtained for the AM-DIA (5) method, whereas for the JONSWAP spectrum, the highest accuracy is obtained for the AM-DIA (2) method. For the JONSWAP spectrum, the residual variance in the AM-DIA method first decreases as the configuration number increases from one to two, and then it increases from two up to five configurations. Moreover, for the PM spectrum the residual variance decreases as the number of configurations increases, although there is a small increase for four configurations. The AM-DIA (2) seems "fairly" accurate for both spectra compared with the other AM-DIA methods.

5.5 Practical Applicability of the Alternative Multiple Discrete-Interaction Approximation Method to Complex Situations

Although the AM-DIA method seems has a shortcoming for the JONSWAP spectrum, the superiority of the AM-DIA method is examined for double-peak spectra. Two different wave groups are simulated with different sets of parameters $H_{1/3}$, $T_{1/3}$, γ_i, S_i, and θ_i ($i = 2$) for double-peak spectra. Particularly, the double-peak spectra examined has peak frequencies at $f_{p1} = 0.13$ Hz and $f_{p2} = 0.1$ Hz, and $f_{p1} = 0.2$ Hz and $f_{p2} = 0.1$ Hz, and the energy concentration parameters are $\gamma = 3.3$ and $S_{max} = 15$ for the higher peak frequency spectrum, and $\gamma = 7.0$ and $S_{max} = 75$ for the lower peak frequency spectrum.

Figure 5.20 shows the initial frequency spectrum and distributions of the nonlinear energy transfer spectrum for the lower peak frequency spectrum ($f_{p1} = 0.13$ Hz and $f_{p2} = 0.1$ Hz) in the AM-DIA method with up to five configurations in comparison with those in the DIA, RIAM, and SRIAM methods for the crossing angle $\Delta\theta = 0°$. The numerical simulations were performed under duration-limited conditions for 12 h. As can be seen in Fig. 5.20, at the initial time the three-lobe pattern of the nonlinear energy transfer spectrum is clearly shown at the higher and lower peak frequencies, meaning that energy is transferred from intermediate frequencies to higher and lower frequencies. As the number of configurations increases, the AM-DIA results are similar to those estimated in the RIAM and SRIAM methods even though the DIA method can only show one three-lobe pattern of the nonlinear energy transfer spectrum at the high-frequency

peak. The AM-DIA method with more than one configuration is relatively more accurate than that with only one configuration. The unrealistic pattern of the nonlinear energy transfer spectrum in the AM-DIA (3)–(5) methods in the single-peak spectrum case, as shown in Fig. 5.11, does not appear in double-peak spectrum case.

Figure 5.21 shows a comparison of the frequency spectra in the AM-DIA method and in the DIA, RIAM, and SRIAM methods after 12 h of simulation. After $t = 12$ h, the energy spectra gradually change to a single-peak spectrum; the high-frequency peak disappears and the frequency downshifts. However, the frequency downshift at $t = 12$ h is only clearly visible in the AM-DIA (2) result, as shown in Fig. 5.21(b). The AM-DIA (1)–(5), except the AM-DIA (2) methods, need longer computational time to yield frequency downshift.

A comparison of the nonlinear energy transfer spectrum in the AM-DIA method and in the DIA, RIAM, and SRIAM methods after 12 h of simulation are shown in Fig. 5.22. Although the magnitudes of positive extreme values of the nonlinear energy transfer spectrum in the RIAM method are slightly different from those in the SRIAM, AM-DIA, and DIA methods, the nonlinear energy transfer spectrum in the AM-DIA (2) method seems similar to those in the SRIAM methods.

Figure 5.20. Comparison of the nonlinear energy transfer spectrum for double-peak spectrum with peak frequencies at $f_{p1} = 0.13$ Hz and $f_{p2} = 0.1$ Hz in the AM-DIA, DIA, RIAM, and SRIAM methods at $t = 0$.

Figure 5.21. Comparison of the frequency spectrum for the double-peak spectrum with peak frequencies at $f_{p1} = 0.13$ Hz and $f_{p2} = 0.1$ Hz in the AM-DIA, DIA, RIAM, and SRIAM methods at $t = 12$ h.

Figure 5.22. Comparison of the nonlinear energy transfer spectrum for the double-peak spectrum with peak frequencies at $f_{p1} = 0.13$ Hz and $f_{p2} = 0.1$ Hz in the AM-DIA, DIA, RIAM, and SRIAM at $t = 12$ h.

Figure 5.23. Comparison of the nonlinear energy transfer spectrum for double-peak spectrum with peak frequencies at f_{p1} = 0.2 Hz and f_{p2} = 0.1 Hz in the AM-DIA, DIA, RIAM, and SRIAM methods at t = 0.

Figure 5.24. Comparison of the frequency spectrum for the double-peak spectrum with peak frequencies at f_{p1} = 0.2 Hz and f_{p2} = 0.1 Hz in the AM-DIA, DIA, RIAM, and SRIAM methods at t = 12 h.

Figure 5.25. Comparison of the nonlinear energy transfer spectrum for the double-peak spectrum with peak frequencies at $f_{p1} = 0.2$ Hz and $f_{p2} = 0.1$ Hz in the AM-DIA, DIA, RIAM, and SRIAM methods at $t = 12$ h.
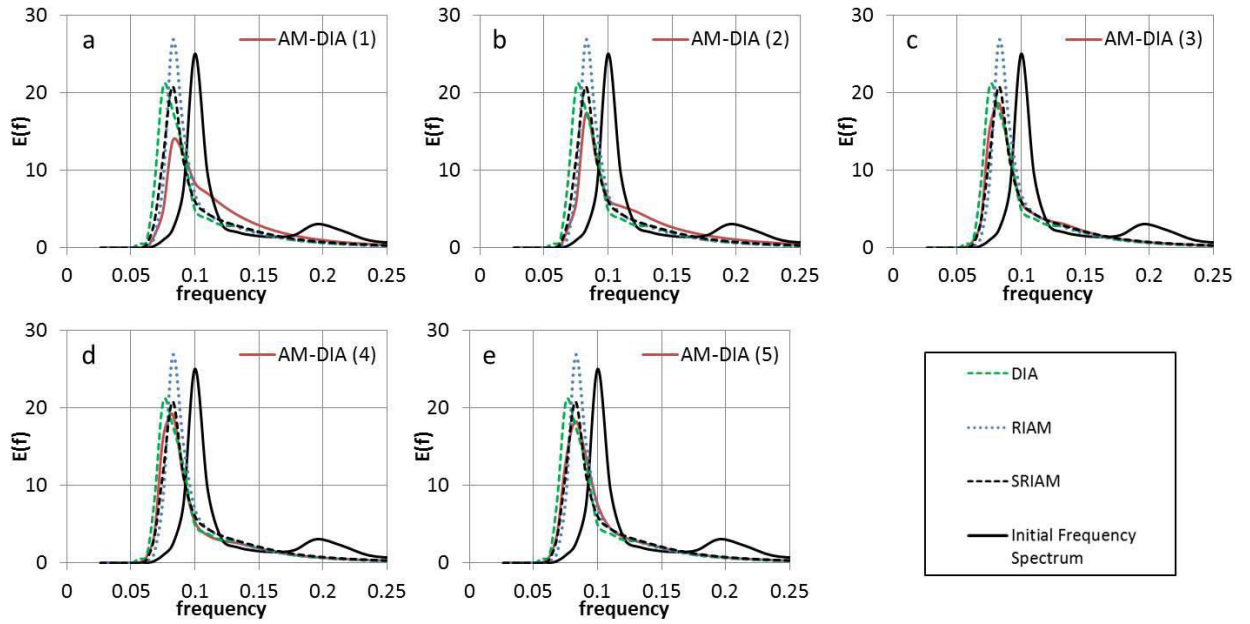
Figure 5.26. Comparison of the frequency spectrum for the double-peak spectrum with peak frequencies at $f_{p1} = 0.2$ Hz and $f_{p2} = 0.1$ Hz in the AM-DIA, DIA, RIAM, and SRIAM method at $t = 120$ h.
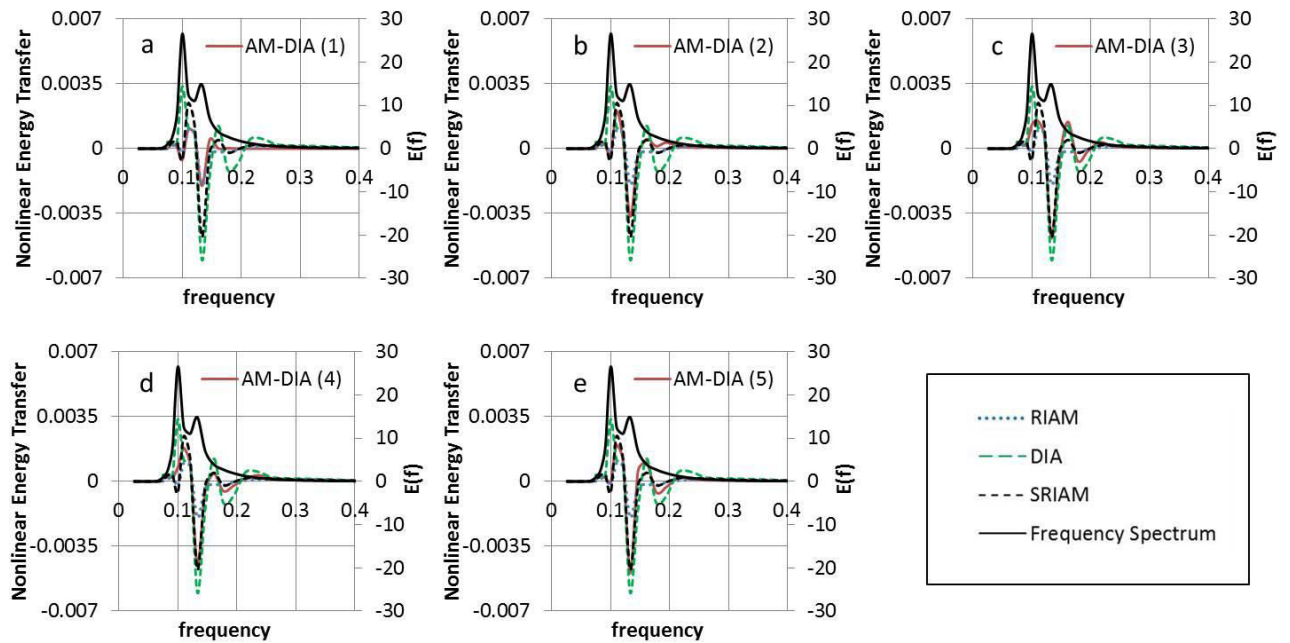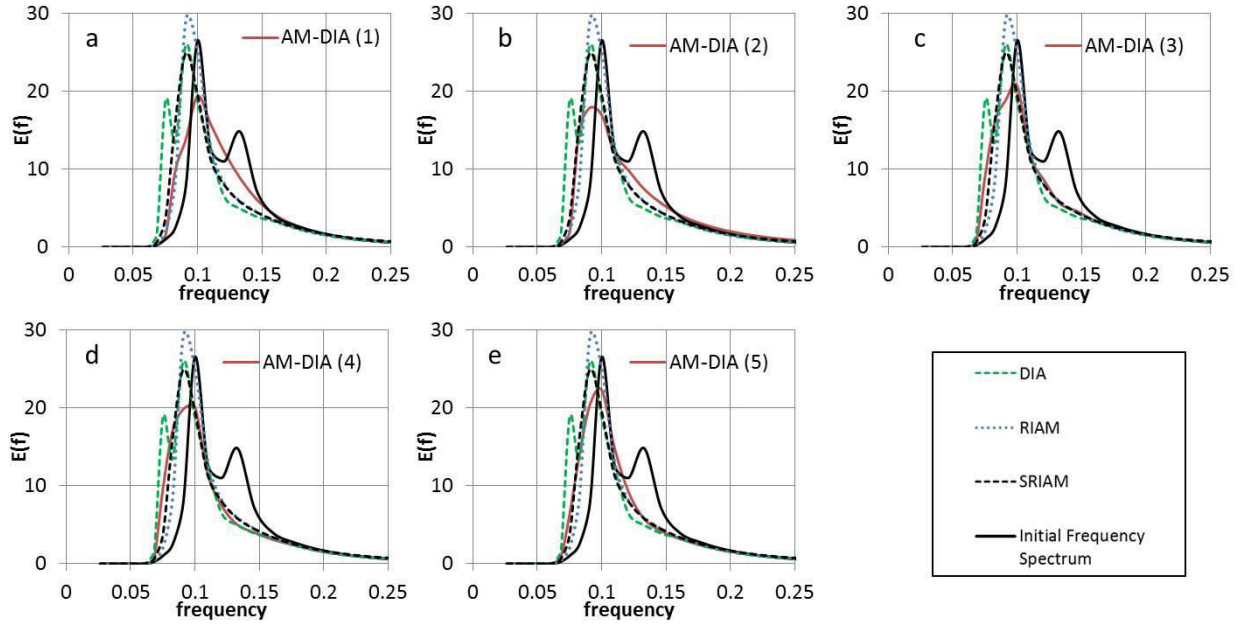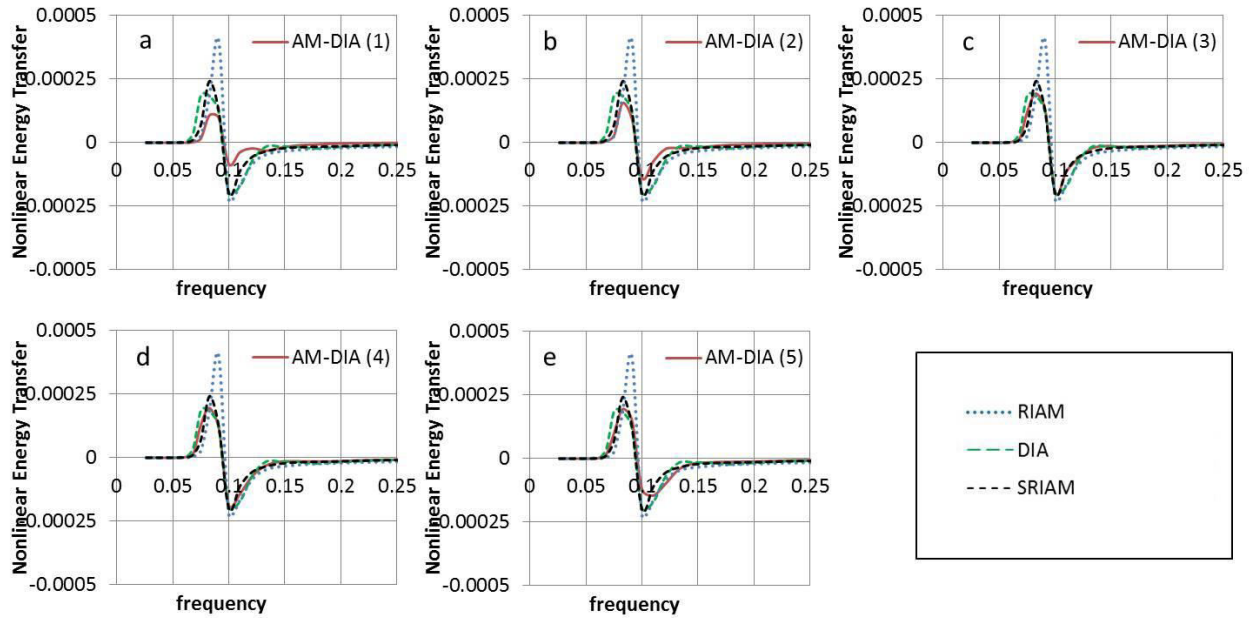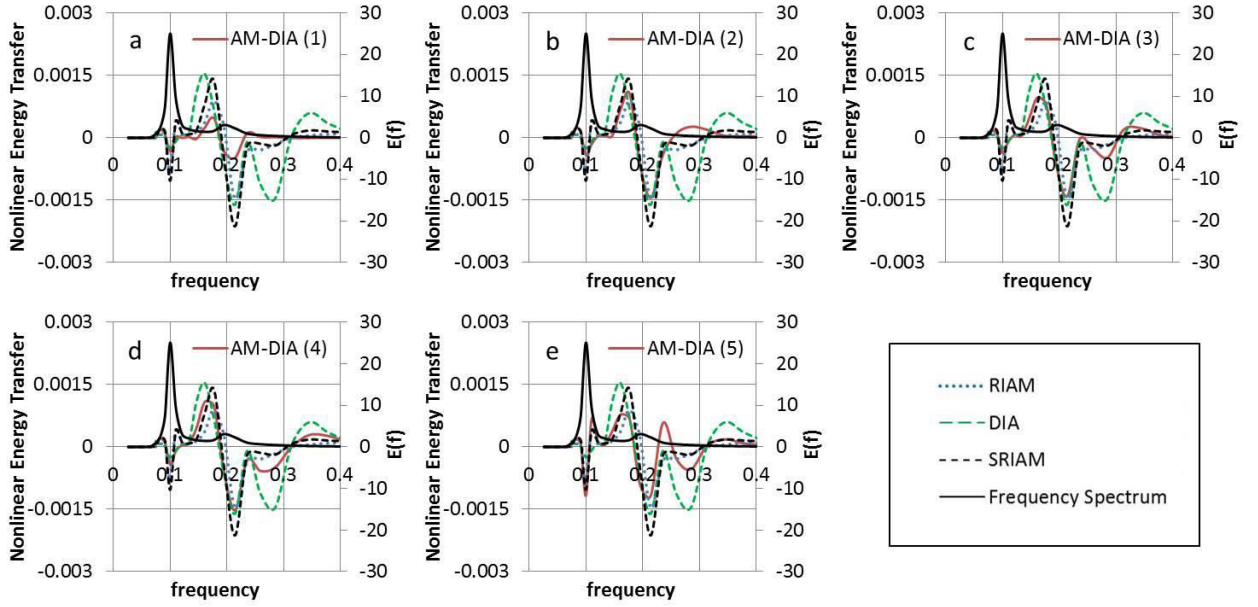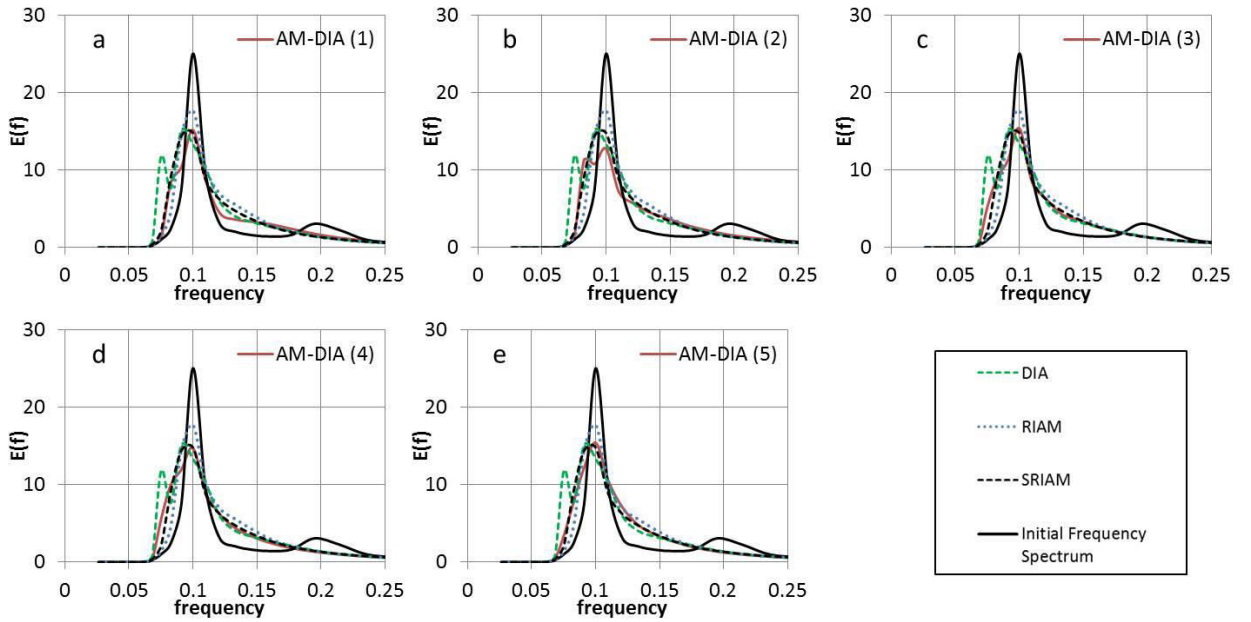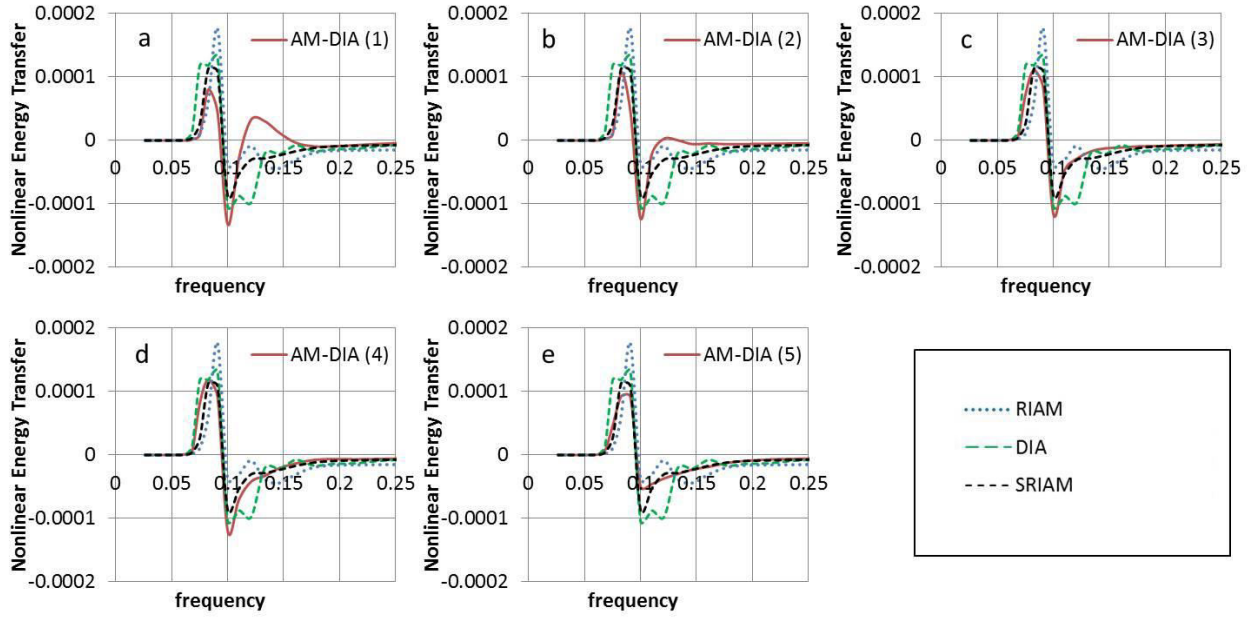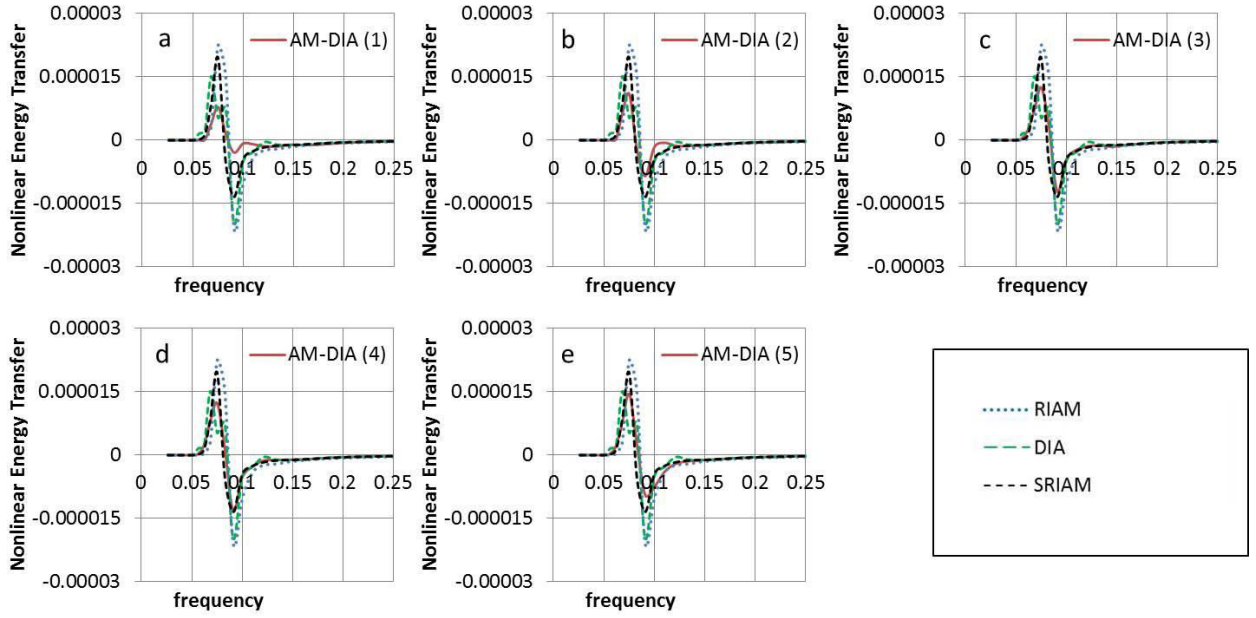
Figure 5.27. Comparison of the nonlinear energy transfer spectrum for the double-peak spectrum with peak frequencies at f_{p1} = 0.2 Hz and f_{p2} = 0.1 Hz in by the AM-DIA, DIA, RIAM, and SRIAM methods at t = 120 h.

Figure 5.23 shows the double-peak spectra for the higher peak frequency spectrum (f_{p1} = 0.2 Hz and f_{p2} = 0.1 Hz) at t = 0. The nonlinear energy transfer spectrum in the AM-DIA method for this case is different from that for the lower peak frequency case. The three-lobe pattern of the nonlinear energy transfer spectrum is observed for both the higher and lower peak frequency case, however, the results in the AM-DIA (3)–(5) methods show the unrealistic pattern at high frequencies. There are two negative extreme values at high frequencies. The AM-DIA (2) method seems more superior to the other AM-DIA methods. The nonlinear energy transfer spectrum in the AM-DIA (2) method is very similar to those estimated in the RIAM and SRIAM methods, but very different with those in the DIA method.

Figure 5.24 shows a comparison of the frequency spectrum after 12 h of simulation in the AM-DIA method and in the DIA, RIAM, and SRIAM methods. The results in all of the AM-DIA methods agree well with the large coupling between the two wave systems. The energy flows from the peak frequencies of the short waves to frequencies on both sides of the peak frequencies (Masson, 1993). The role of nonlinear energy transfer in stabilizing the shape of the wave spectrum was confirmed, and it tends to remove any perturbations such as local sea spectra in the spectral distribution. Although the AM-DIA (2) method clearly shows frequency downshift after t = 12 h for the lower peak frequency spectrum, it is not the case for the higher peak frequency

spectrum. As can be seen in Fig. 5.24, at t = 12 h the double-peak frequency spectra changes to single-peak spectra; nevertheless only the frequency spectrum in the DIA method clearly shows frequency downshift. However, the nonlinear energy transfer spectrum in the AM-DIA, RIAM, and SRIAM methods are similar to each other, but slightly different from those in the DIA method (Fig. 5.25).

Because frequency downshift did not appear after t = 12 h, the simulation of the higher peak frequency spectrum were performed for 120 h. Figure 5.26 shows a comparison of the frequency spectrum in the AM-DIA, DIA, RIAM, and SRIAM methods at t = 120 h. As can be seen in Fig. 5.26, the shape of the frequency spectrum changes to single peak and the peak frequency moves toward low frequencies at t = 120 h. The frequency spectrum and nonlinear energy transfer spectrum in the AM-DIA method are similar to those in the DIA, RIAM, and SRIAM methods. This result shows that the AM-DIA method is applicable to long-time integrations and complex situations.

5.6 Conclusion

It can be concluded that reducing the number of configurations for nonlinear energy transfer is possible to achieve less computational costs without losing the accuracy. In the R-SRIAM method, nice configurations are able to show almost the same degree of accuracy as the original SRIAM method. As a result, the R-SRIAM method is less time consuming than the original SRIAM method, but still more time consuming than the DIA method.

The configurations for the R-SRIAM method show that the quasi-singular quadruplets contribute the most to nonlinear energy transfer, whereas the regular quadruplets contribute less. Hence, the AM-DIA method is an efficient configuration in which only the quasi-singular quadruplets are selected. Various configuration number for the AM-DIA method shown different results in the cases considered. However, the AM-DIA method with two configurations is suggested to be more superior to the other methods. It is also able to show frequency downshift in single-peak spectra after 12 h of simulation for both the PM and JONSWAP spectra. For double-peak spectra, the AM-DIA method is more superior to the other methods. Although it is not as accurate as the RIAM, SRIAM, and R-SRIAM methods, the AM-DIA method is obviously better in accuracy than the DIA method, even for double-peak spectra. This result suggests that the reduction of resonant configuration number is efficient in practical applications, even in

complex situations. In terms of efficiency, the advantage of the AM-DIA method is more economically acceptable compared with the RIAM, SRIAM, and R-SRIAM methods.

CHAPTER 6

SUMMARY AND FUTURE WORK

6.1 Summary

In this study, a numerical study of nonlinear energy transfer computation for a gravity wave spectrum is carried out and discussed. The efficient configuration numbers for computing nonlinear energy transfer are presented to obtain methods with sufficient accuracy and efficiency that can be practically incorporated in wave models. The results and conclusions from the study are summarized as follows.

An intercomparison of the DIA, RIAM, and SRIAM methods in the WAM shows interesting characters of the wave spectrum, especially the relation between the frequency downshift and the energy concentration parameters of the directional spectra. In other words, the intensity of frequency downshift caused by nonlinear energy transfer increases with increasing energy concentration in frequency and direction.

Characteristics of the directional distribution of bimodal directional spectra are also discussed in Chapter 3. An interesting characteristic influenced by the crossing angle $\Delta\theta$ between two wave groups in the bimodal spectrum is observed, i.e., a large coupling between the wave groups can be seen when the two peak frequencies in the bimodal spectrum are relatively narrow in direction.

The evolution of directional spectra in finite water depths caused by nonlinear energy transfer was confirmed to be much faster in the FD-RIAM method than in the other methods in deep water. Although the spectra evolve with its peak frequency moved to low frequencies in both the PM and JONSWAP spectra, the peak frequency is maintained at almost the same frequency by decreasing its magnitude. The enhancement factor R and downshift factor used in the WAM are also evaluated. The enhancement factor R adopted in the WAM shows a better agreement with those computed in the FD-RIAM method for small S_{max} and γ.

Moreover, in Chapter 5, the efficient configuration numbers for computing nonlinear energy transfer are proposed. First, the SRIAM method is modified by reducing the resonance number of configurations. The resulting method is called the R-SRIAM method, in which nine configurations are found to be able to show almost the same degree of accuracy as the original SRIAM method with 20 configurations. The R-SRIAM method is also shown to be applicable to long-time integrations.

Furthermore, various efficient resonance configuration numbers are proposed by selecting configurations only from the quasi-singular quadruplets. The method is called the AM-DIA method. Five configuration numbers are identified and the corresponding coefficients are optimized using the nonnegative least-square method. Although the AM-DIA method has different result for different configuration numbers in many cases, the AM-DIA method with two configurations is suggested as the most efficient method for computing nonlinear energy transfer. Examples in Chapter 5 show that the AM-DIA method is more accurate than the DIA method. In terms of accuracy, the AM-DIA method seems to have a shortcoming for the JONSWAP spectrum; however, it evidently has better accuracy than the DIA method. The computational costs of the AM-DIA method is more economical compared with the RIAM, SRIAM, and R-SRIAM methods. The AM-DIA method uses almost the same computational time as the original DIA, which is 20 times faster than the SRIAM method.

In summary, both R-SRIAM and AM-DIA methods can be considered the promising methods for nonlinear energy transfer computations in deep water.

6.2 Future Work

In this study, to evaluate the practical capability of the R-RIAM and AMDIA methods in the third-generation wave model, the methods were incorporated into the WAM, which originally was implemented with the DIA method as the conventional method for nonlinear energy transfer computations. However, in conventional wave model codes, the formulations used for the wave action density balance equations were developed to conform to the DIA method, including the wind input and dissipation term. Thus, the numerical simulations in this study were conducted without taking the wind input and dissipation term into account. In the near future, recalibration or reconfirming of other source terms is required when replacing the DIA method with more accurate algorithms to develop a new operational wave model. Another interesting future work is

to examine how the different physics for wind input and dissipation will react to the change in methods for computing nonlinear energy transfer.

BIBLIOGRAPHY

Ardhuin, F., Herbers, T.H.C., O'Reilly, W.C., 2001. A hybrid Eulerian–Lagrangian model for spectral wave evolution with application to bottom friction on the continental shelf, *Journal of Physical Oceanography* 31 (6), 1498–1516.

Banner, M. L. and Young, I. R., 1994. Modelling Spectral Dissipation in the Evolution of Wind Waves – Part 1. Assessment of existing model performances, *J. Phys. Oceanogr.*, 24, 1550-1671.

Benoit, M., Marcos, F., Becq-Girard, F., 1997. Development of a third generation shallow-water wave model with unstructured spatial meshing. In: Edge, Billy L. (Ed.). *Proceedings of the 25th International Conference on Coastal Engineering*, 1996, vol. 1. American Society of Engineers Publications, pp. 465–478.

Booij, N., Ris, R.C., Holthuijsen, L.H., 1999. A third generation wave model for coastal regions, Part I: model description and validation, *Journal of Geophysical Research* 104 (C4), 7649–7666.

Goda, Y. , 2010. Random Seas and Design of Maritime Structures, 3rd Edition, *Advanced Series on Ocean Engineering*, Vol.33, World Scientific Publishing, 708p.

Hashimoto N., H. Tsuruya and Y. Nakagawa, 1998, Numerical computations of the nonlinear energy transfer of gravity-wave spectra in finite-water depths, *Coastal Engineering Journal*, 40, World Scientific, 23-40.

Hashimoto, N and K. Kawaguchi, 2001. Extension and Modification of Discrete Interaction Approximation (DIA) for Computing Nonlinear Energy Transfer of Gravity Wave Spectra, *Proc. 4th Int. Symp. Waves* 2001, 530-539.

Hashimoto, N., I. G. Haagsma and L. H. Holthuijsen, 2002. Four-wave interactions in swan. In *Proc. 28th Int. Conf. Coastal Eng.*, Cardiff, Wales. ASCE, In Press.

Hasselmann, K., 1960. Grundgleichungen der Seegangsvoraussage, *Schiffstechnik*, 191-195.

Hasselmann, K., 1962. On the non-linear energy transfer in a gravity-wave spectrum, Part 1, General theory, *Journal of Fluid Mechanics*, 12, 481-500.

Hasselmann, K., 1963. On the nonlinear energy transfer in a gravity-wave spectrum, Part 3, Evaluation of energy flux and sea-swell interactions for a Neuman spectrum, *Journal of Fluid Mechanics*, 15, 385-398.

Hasselmann, K. et al., 1973. Measurements of wind waves growth and swell decay during the Joint North Sea Wave Project (JONSWAP), Dt. Hydrogr. Z., A8(12), 95p.

Hasselmann, S. and K. Hasselmann, 1981. A symmetrical method of computing the nonlinear transfer in a gravity wave spectrum, *Hamb. Geophys. Einzelschriften, Reihe A:Wiss. Abhand.*, 52, 138p.

Hasselmann, S. and K. Hasselmann, 1985. Computations and Parameterizations of the Nonlinear Energy Transfer in a Gravity-Wave Spectrum. Part I: A New Method for Efficient Computations of the Exact Nonlinear Transfer Integral, *Journal of Physical Oceanography*, 15, 1378-1391.

Herterich, K., Hasselmann, K., 1980. A similarity relation for the non-linear energy transfer in a finite-depth gravity-wave spectrum. *Journal of Fluid Mechanics* 97, 215–224.

Holthuijsen, L. H., 2007. Waves in oceanic and coastal waters. *Cambridge: Cambridge University Press*.

Komatsu, K., T. Kusaba and A. Masuda, 1993. An efficient method for computing nonlinear energy transfer among wind waves, *Bull. Res. Inst. Apple. Mech. Kyushu Univ.*, 75, 121-146 (in Japanese).

Komatsu, K. and A. Masuda, 1996. A new scheme of nonlinear energy transfer among wind waves: RIAM method − algorithm and performance -, *Journal of Oceanography*, 52, 509-537.

Komatsu, K. 1996. Development of a new generation wave forecasting model based on a new scheme of nonlinear energy transfer among wind waves, Dr. Thesis, University of Kyushu, 155p. (in Japanese).

Komatsu, et al., 2001. Nonlinear energy transfer among wind waves in coastal region, Bull. Fish. Res. Agen, pp. 1, 7-21 (in Japanese).

L Cavaleri, J-HGM Alves, F Ardhuin, A Babanin, M Banner, K Belibassakis, M Benoit, M Donelan, J Groeneweg, THC Herbers, PAEM Hwang, PAEM Janssen, T Janssen, IV Lavrenov, R Magne, Jaak Monbaliu, M Onorato, V Polnikov, D Resio, WE Rogers, A Sheremet, J McKee Smith, HL Tolman, G Van Vledder, Judith Wolf, Ian Young, WISE Group, 2007. Wave modelling–the state of the art, *Journal Progress in Oceanography*, 75, 603-674p.

Masuda, A, 1980. Nonlinear energy transfer between wind waves, *Journal of Physical Oceanography*, 10, 2082-2092.

Masson, D., 1993. On the nonlinear coupling between swell and wind waves, *J. Phys. Oceanogr.*, 23, pp.1249-1258.

Phillips, O.M., 1981a. Wave interactions – The evolution of an idea. *Journal of Fluid Mechanics* 106, 5–227.

Resio, D. and W. Perrie, 1991. A numerical study of nonlinear energy fluxes due to wave-wave interactions, *Journal of Fluid Mechanics*, 223, 603-629.

Tamura, A, 2008. Current-Induced Modulation of the Ocean Wave Spectrum and the Role of Nonlinear Energy Transfer, *Journal of Physical Oceanography*, Volume 38, 2662-2984

Tolman, H.L., 1991. A third generation model for wind waves on slowly varying, unsteady, and inhomogeneous depths and currents. *Journal of Geophysical Research* 21, 782–797.

Tolman, H.L., 2002c. User manual and system documentation of WAVEWATCH III version 2.22. Technical Report 222, NOAA/NWS/NCEP/MMAB.

Tolman, H.L., 2003. Optimum Discrete Interaction Approximations for wind waves. Part 1: Mapping using inverse modeling. Tech. Note 227, NOAA/NWS/NCEP/MMAB.

Tolman, H.L., 2004. Inverse modeling of Discrete Interaction Approximations for nonlinear interactions in wind waves. *Ocean Modelling*, 6, 405–422.

Tolman, H.L., 2013. A Generalized Multiple Discrete Interaction Approximation for resonant four-wave interactions in wind wave models. *Ocean Modelling*, 70, 11-24.

Tracy, B. A. and D. T. Resio, 1982. Theory and calculation of the nonlinear energy transfer between sea waves in deep water, U. S. Army Engineer Waterways Experimental Station, Rep. No. 11, Vicksburg, U. S. A.

Tsagareli, K. N., A. V. Babanin, D. J. Walker, I. R. Young, 2005. A numerical Study of the Four-Wave Nonlinear Interactions in Finite-Depth Water, *17th Australasian Coastal and Ocean Engineering Conf and 10th Australasian Port and Harbour Conf*, 299-304

Ueno, K. and M. Ishizaka, 1997. On an efficient calculation method of the nonlinear energy transfer in wind waves, Sottukojiho, JMA, 64, 75-80 (in Japanese).

Van Vledder, G.Ph., Herbers, T.H.C., Jensen, R.E., Resio, D.T., Tracy, B.A., 2000. Modelling of non-linear quadruplet wave–wave interactions in operational wave models. In: Edge, Billy L. (Ed.), Coastal Engineering 2000, *Proceedings of the 27th International Conference on Coastal Engineering*. ASCE, Sydney, Australia, pp. 797–811.

WAMDI Group, 1988. The WAM model – a third generation ocean wave prediction model. *Journal of Physical Oceanography* 18, 1775–1809.

Webb, D. J., 1978. Non-linear transfers between sea waves, Deep-Sea Res., 25, 279-298.

Young, I.R. ,1999.Wind generated ocean waves. Elsevier, Oxford, UK.

Young, I.R., van Vledder, G.Ph., 1993. A review of the central role of non-linear interactions in wind–wave evolution. Philosophical Transactions of the Royal Society of London A 342, 505–524.